



AFRL-OSR-VA-TR-2014-0072

---

## **Development of Energetic Actuators for Shear and Vortex Dominated Flow Control**

S. H. Popkin, T. M. Taylor, B.  
Z. Cybyk  
The Johns Hopkins  
University  
Applied Physics Laboratory  
1110 Johns Hopkins Road  
Laurel, MD 20723-6099

---

19-02-2014

**Final Report**

<b>DISTRIBUTION A: Distribution approved for public release.</b>
--

Air Force Research Laboratory  
AF Office Of Scientific Research (AFOSR)/RTB1

<b>REPORT DOCUMENTATION PAGE</b>				Form Approved OMB No. 0704-0188							
<p>The public reporting burden for this collection of information is estimated to average 1 hour per response, including the time for reviewing instructions, searching existing data sources, gathering and maintaining the data needed, and completing and reviewing the collection of information. Send comments regarding this burden estimate or any other aspect of this collection of information, including suggestions for reducing the burden, to the Department of Defense, Executive Service Directorate (0704-0188). Respondents should be aware that notwithstanding any other provision of law, no person shall be subject to any penalty for failing to comply with a collection of information if it does not display a currently valid OMB control number.</p> <p><b>PLEASE DO NOT RETURN YOUR FORM TO THE ABOVE ORGANIZATION.</b></p>											
<b>1. REPORT DATE (DD-MM-YYYY)</b> 19-02-2014		<b>2. REPORT TYPE</b> Final Performance Report		<b>3. DATES COVERED (From - To)</b> 30-11-2009 to 30-11-2013							
<b>4. TITLE AND SUBTITLE</b> Development of Energetic Actuators for Shear and Vortex Dominated Flow Control				<b>5a. CONTRACT NUMBER</b>							
				<b>5b. GRANT NUMBER</b> FA9550-09-1-0575							
				<b>5c. PROGRAM ELEMENT NUMBER</b>							
<b>6. AUTHOR(S)</b> S. H. Popkin, T. M. Taylor, B. Z. Cybyk				<b>5d. PROJECT NUMBER</b>							
				<b>5e. TASK NUMBER</b> JHU/APL Task FGX62							
				<b>5f. WORK UNIT NUMBER</b>							
<b>7. PERFORMING ORGANIZATION NAME(S) AND ADDRESS(ES)</b> The Johns Hopkins University Applied Physics Laboratory 1110 Johns Hopkins Road Laurel, MD 20723-6099				<b>8. PERFORMING ORGANIZATION REPORT NUMBER</b>  FPS-R-14-0042							
<b>9. SPONSORING/MONITORING AGENCY NAME(S) AND ADDRESS(ES)</b> USAF, AFRL AFOSR/NA 875 N. Randolph St., Rm. 3112 Arlington, VA 22203				<b>10. SPONSOR/MONITOR'S ACRONYM(S)</b>							
				<b>11. SPONSOR/MONITOR'S REPORT NUMBER(S)</b>							
<b>12. DISTRIBUTION/AVAILABILITY STATEMENT</b> Unlimited											
<b>13. SUPPLEMENTARY NOTES</b>											
<b>14. ABSTRACT</b> Active flow control (AFC) techniques available for high-speed flow applications, including supersonic and hypersonic, are very limited. The Johns Hopkins University Applied Physics Laboratory (JHU/APL), in collaboration with the Florida State University Advanced Aero-Propulsion Laboratory (FSU/AAPL), is investigating and developing a promising device for high-speed flow control called the SparkJet actuator. This actuator, which produces a synthetic jet with high exhaust velocities, holds the promise of manipulating high-speed flows without active mechanical components. Computational Fluid Dynamic (CFD) modeling is used to investigate the predicted fundamental physics and flow interactions within and near the SparkJet actuator. The CFD results were used for comparison to microschlieren imagery acquired at FSU/AAPL and the 1-D numerical model developed at JHU/APL. To further verify the model accuracy, experimental testing involving time-dependent, pressure measurements of the actuator cavity pressure as a function of orifice diameter, cavity volume, and energy deposition. Finally, the SparkJet actuator design has been modified to create reliable and efficient devices.											
<b>15. SUBJECT TERMS</b> Micro-adaptive flow control, flow control actuator, SparkJet actuator, supersonic flow											
<b>16. SECURITY CLASSIFICATION OF:</b> <table border="1" style="width: 100%; border-collapse: collapse;"> <tr> <td style="width: 33%; padding: 2px;">a. REPORT</td> <td style="width: 33%; padding: 2px;">b. ABSTRACT</td> <td style="width: 33%; padding: 2px;">c. THIS PAGE</td> </tr> <tr> <td style="text-align: center; padding: 2px;">(U)</td> <td style="text-align: center; padding: 2px;">(U)</td> <td style="text-align: center; padding: 2px;">(U)</td> </tr> </table>			a. REPORT	b. ABSTRACT	c. THIS PAGE	(U)	(U)	(U)	<b>17. LIMITATION OF ABSTRACT</b>		<b>18. NUMBER OF PAGES</b> 80
a. REPORT	b. ABSTRACT	c. THIS PAGE									
(U)	(U)	(U)									
			<b>19a. NAME OF RESPONSIBLE PERSON</b> B. Z. Cybyk		<b>19b. TELEPHONE NUMBER (Include area code)</b> 240-228-7624						

**FINAL REPORT**

**FPS-R-14-0042**

**DEVELOPMENT AND APPLICATION OF ENERGETIC  
ACTUATORS FOR SHEAR AND VORTEX DOMINATED FLOW  
CONTROL**



**February 2014**

Prepared by  
S. H. Popkin, T. M. Taylor, B. Z. Cybyk

The Johns Hopkins University Applied Physics Laboratory  
11100 Johns Hopkins Road  
Laurel, MD 20723-6099

This page intentionally left blank.



# TABLE OF CONTENTS

Executive Summary . . . . .	xii
Nomenclature . . . . .	xv
1 Introduction . . . . .	1
1.1 Supersonic Open Cavity Flow . . . . .	1
1.2 High-Momentum Flow Control Actuators . . . . .	2
1.3 SparkJet Actuator . . . . .	5
2 Simplified Numerical Modeling . . . . .	11
2.1 Supporting CFD Simulations . . . . .	12
2.2 Governing Equations . . . . .	14
2.3 Single Cycle Simulation . . . . .	22
2.4 Simulating High-Frequency Actuation . . . . .	25
3 Experimental Details and Data Acquisition . . . . .	28
3.1 SparkJet Actuator . . . . .	30
3.2 SparkJet Power Supplies . . . . .	32
3.3 Data Acquisition . . . . .	34
3.4 Cavity Pressure Sensor . . . . .	34
3.5 Signal Post-Processing . . . . .	36
4 Pressure-Based Results and Analysis . . . . .	37
4.1 Basic Operation . . . . .	37
4.2 Efficiency . . . . .	41
5 Arc Power Measurements . . . . .	46
5.1 Results . . . . .	47
5.2 Analysis of Energy Losses . . . . .	50
6 Design Optimization . . . . .	51
6.1 Electrode Design . . . . .	51
6.2 Non-ZNMF Design . . . . .	55
7 Wind Tunnel Testing . . . . .	56
8 Conclusions . . . . .	58
9 Future Work . . . . .	60
10 Acknowledgements . . . . .	60
11 References . . . . .	60

This page intentionally left blank.

# LIST OF FIGURES

Figure 1	F-22 Raptor flying with open bomb bay doors[2]. . . . .	2
Figure 2	Photograph of the supersonic cavity flow model used by FSU/AAPL[3].	2
Figure 3	Sketch of REM design sizing parameters for unsteady REM actuation[14].	4
Figure 4	Basic schematic of the three stages of SparkJet operation. . . . .	5
Figure 5	Microschlieren images at two time delays after Stage 1 initiation showing the a) blast wave and b) turbulent jet formation in the early portion of Stage 2[25]. . . . .	7
Figure 6	Average velocity field contours and vectors for the 25 $\mu$ F discharge at 30 $\mu$ s, 50 $\mu$ s, 70 $\mu$ s, and 90 $\mu$ s delay times[24]. . . . .	10
Figure 7	Sketch of the assumed control volume where the larger gray cylinder represents the cavity volume and the smaller blue cylinder represents the orifice volume. . . . .	12
Figure 8	Structured, axi-symmetric grid representation of the SparkJet internal geometry with grid axis units in millimeters. The red section represents the grid cells raised to an elevated temperature and pressure to represent the energy deposition in Stage 1. . . . .	12
Figure 9	Time-dependent CFD simulation of the volume-averaged cavity pressure, temperature, and density and area-averaged jet velocity through the orifice. . . . .	13
Figure 10	Electrical representation of the thermal heat transfer process for the SparkJet actuator. . . . .	18
Figure 11	Sketch of the thermal heat transfer modeled using finite difference equations . . . . .	19
Figure 12	Notional temperature profile used to compare the combined thermal resistance and capacitance method and the discretization method. . . . .	20
Figure 13	Wall temperature response to the notional temperature profile using the combined thermal capacitive and resistive model. . . . .	21
Figure 14	Wall temperature response to the notional temperature profile simulating 1 kHz actuation over 50 cycles. . . . .	21
Figure 15	Time and space dependent thermal response of the Macor material to the notional temperature profile applied to the internal wall of the Macor during a single cycle. . . . .	22
Figure 16	Time and space dependent thermal response of the Macor material to the notional temperature profile applied at a frequency of 1 kHz over 50 cycles. . . . .	23

Figure 17	Simulation of the time-dependent variation in cavity pressure, temperature and density and the velocity through the orifice during early portion of the SparkJet cycle. . . . .	24
Figure 18	Simulation of the time-dependent variation in cavity pressure, temperature, and density and the velocity through the orifice for the entire SparkJet cycle. Note that cavity temperature, pressure, and density have returned to original ambient conditions as given in Table 1. . . . .	25
Figure 19	Comparison of the cavity pressure, temperature, and density and orifice velocity versus time based on the CFD simulations and the simplified numerical model. . . . .	26
Figure 20	Simulation of the time-dependent variation in cavity pressure, temperature, and density and the velocity through the orifice for four SparkJet cycles at 100 Hz. . . . .	26
Figure 21	Simulation of the momentum through the SparkJet orifice as a function of time when operated at 100, 1000, and 5000 Hz. . . . .	27
Figure 22	Magnitude plot of the steady-state momentum throughput from the SparkJet actuator operated from 1 Hz to 10 kHz for orifice diameters of 0.4, 1.0, and 2.0 mm. . . . .	28
Figure 23	Magnitude plot of the steady-state momentum throughput from the SparkJet actuator operated from 1 Hz to 10 kHz for energy deposition values of 0.24, 0.45, and 0.90 J. . . . .	29
Figure 24	Magnitude plot of the steady-state momentum throughput from the SparkJet actuator operated from 1 Hz to 10 kHz for cavity volumes of 42.4, 84.8, and 169.6 mm <sup>3</sup> . . . . .	29
Figure 25	Photograph of the SparkJet cavities and lids used to characterize the effect of cavity volume and orifice diameter on SparkJet cavity pressure rise and performance. . . . .	30
Figure 26	Photograph of the SparkJet setup with eight 0.88 $\mu$ F capacitors across the electrodes. Note the proximity of the capacitor connections to the SparkJet itself to allow for short wires and prevent losses that would exist with long wires. . . . .	31
Figure 27	SparkJet Array (a) schematic and photograph of the (b) side view and (c) top view. . . . .	32
Figure 28	Circuit diagram of the 600 V external trigger SparkJet power supply. . . . .	33
Figure 29	Circuit diagram of the 600 V pseudo-series trigger SparkJet power supply. . . . .	33
Figure 30	Drawing of the metal insert used to mate the SparkJet Macor housing to the PCB pressure transducer. . . . .	35
Figure 31	Cross section view of the SparkJet cavity, electrodes (configured for an external trigger) and installed pressure sensor. . . . .	35
Figure 32	Photograph of the uninstalled PCB 105C12 dynamic pressure sensor. . . . .	36
Figure 33	Pressure and FFT data demonstrating the effect of low-pass filtering on the SparkJet internal cavity pressure measurements. . . . .	38

Figure 34	Example of data acquisition output for the 600ET setup and SparkJet cavity volume of 169.6 mm <sup>3</sup> , orifice diameter of 1.0 mm and capacitance of 5.08 $\mu$ F. . . . .	39
Figure 35	Example of data acquisition output for the 600PST setup and SparkJet cavity volume of 84.8 mm <sup>3</sup> , orifice diameter of 1.0 mm and capacitance of 1.67 $\mu$ F. . . . .	40
Figure 36	Data acquisition output for the 600PST setup zoomed in to show the current and voltage outputs in more detail. . . . .	40
Figure 37	Variation of the peak cavity pressure as a function of $Q/E$ for three SparkJet cavity volumes, an orifice diameter of 1 mm and an electrode gap of 1.75 mm. . . . .	43
Figure 38	Fast-Fourier transform of ensemble-averaged, unfiltered pressure data displaying the frequency content for a) three cavity volumes at similar $Q_C/E$ values of approximately 27 and b) five input energies, $Q_C$ , and constant cavity volume of 84.8 mm <sup>3</sup> . . . . .	43
Figure 39	Time delayed images using LBMS of the SparkJet exhaust at (a) 10 $\mu$ s, (b) 18 $\mu$ s, and (c) 100 $\mu$ s. . . . .	44
Figure 40	Flow feature velocity analysis: a) table of the number of microschlieren images at each time delay and b) velocity of the jet front and shock waves at various time delays. . . . .	45
Figure 41	CAD representation of the SparkJet actuator designed for a pseudo-series trigger with a pressure sensor installed. . . . .	46
Figure 42	Comparison of pressure vs. time for three electrode gaps of 1.7, 3.0, and 4.0 mm given the same cavity volume (84.4 mm <sup>3</sup> ), orifice diameter (1.0 mm), and approximately similar $Q_C/E$ of 30. . . . .	47
Figure 43	Comparison of efficiency vs. $Q_C/E$ for three electrode gaps of 1.7, 3.0, and 4.0 mm given the same cavity volume (84.8 mm <sup>3</sup> ). . . . .	48
Figure 44	Comparison of the jet front and blast wave velocities using the external trigger mechanism at $Q_C$ of 25.5 and electrode gap of 1.7 mm and the pseudo-series trigger mechanism at $Q_C$ of 12.7 and electrode gap of 3.0 mm. . . . .	48
Figure 45	Voltage and current waveform curves in distinct groups corresponding to each capacitance change for a cavity volume of 84.8 mm <sup>3</sup> . . . . .	49
Figure 46	Efficiency of the conversion of stored capacitor energy to the arc discharge, calculated cavity temperature, and measured pressure rise as a function of $Q_C/E$ . . . . .	50
Figure 47	Comparison of the time dependent temperature and specific heat coefficient ( $C_v$ ) assuming a calorically perfect and imperfect gas as a function of arc discharge current and voltage for (a) a single case and (b) over a range of $Q_C/E$ values. . . . .	51
Figure 48	Tungsten oxidation caused by overheating on 1 mm diameter electrodes after operation at high frequency and subsequent overheating. . . . .	52
Figure 49	Photograph of the electrode design test setup for the pseudo-series triggering SparkJet design. . . . .	53

Figure 50	CAD representation of the non-ZNMF SparkJet design showing the air supply port, orifice array and pressure sensor access hole. . . . .	55
Figure 51	Photograph of the non-ZNMF SparkJet array design tested. . . . .	56
Figure 52	Microschlieren imagery of the non-ZNMF SparkJet array interacting with quiescent flow at varying air supply pressure. . . . .	56
Figure 53	Example of the perturbed supersonic flow and demonstration of how the oblique shock angles are defined. . . . .	57
Figure 54	Shadowgraph image of the baseline Mach 1.5 crossflow over a flat plate at various time delays. . . . .	58
Figure 55	Oblique shock angle variation as a function of time. . . . .	58

This page intentionally left blank.

# LIST OF TABLES

Table 1	Design parameters for numerical model. . . . .	24
Table 2	Design parameters tested to determine the effect of electrode material on electrode survivability. . . . .	54
Table 3	Design parameters tested to determine the effect of electrode diameter on frequency cutoff. . . . .	54



This page intentionally left blank.

# Executive Summary

A variety of active flow control (AFC) methods have been successfully applied to low speed flows. However, AFC techniques available for high-speed flow applications, including supersonic and hypersonic, are very limited. Under Air Force Office of Scientific Research (AFOSR) sponsorship (AFOSR Grant Number FA9550-09-1-0575), The Johns Hopkins University Applied Physics Laboratory (JHU/APL), in collaboration with the Florida State University Advanced Aero-Propulsion Laboratory (FSU/AAPL), is investigating and developing a promising device for high-speed flow control called the SparkJet actuator. This actuator, which produces a synthetic jet with high exhaust velocities, holds the promise of effectively controlling high-speed flows without active mechanical components.

A major accomplishment of this grant involved shadowgraph imagery of flow interactions between an array of SparkJet actuators and a supersonic (Mach 1.5) crossflow. This demonstration of SparkJet control authority was preceded by several other accomplishments: development of a simplified numerical model, experimental validation of the simplified model, improvements to SparkJet design for increased actuator efficiency and reliability, and high-fidelity computational modeling of the SparkJet interactions with quiescent flow.

The SparkJet actuator functions using an arc discharge contained within a cavity. The resulting heated cavity air is forced out of the cavity through an orifice or orifice array to interact with the external flow environment. The simplified one-dimensional (1-D) numerical model provides a simplified method for modeling the complex, multi-physics, multi-dimensional processes associated with a plasma-based flow control actuator such as the SparkJet. Initial actuator modeling was based on fully three-dimensional Computational Fluid Dynamics (CFD) simulations; however, the use of CFD to perform the full design process would have been prohibitively difficult due to time and computational resource limitations. Therefore, a simplified 1-D model derived from the Euler equations, using various assumptions, has been developed to expedite actuator design.

To validate the accuracy of the simplified model, experimental testing was used to record time-dependent, cavity pressure as a function of orifice diameter, cavity volume, and energy deposition. These results showed that the 1-D model over-estimated the pressure rise inside the cavity due to the energy deposition. Measurements of the voltage and current across the electrode gap during the energy deposition show that the power drawn by the arc is less than the assumed stored capacitive energy. In addition, removal of the 1-D model assumptions for instantaneous energy deposition and a calorically perfect gas brought model and experimental results in closer agreement.

Realistic operation of an array of actuators requires reliable and efficient devices. In the interest of reliability, the method of triggering the spark discharge has been modified by triggering directly across the anode and cathode rather than involving a third trigger electrode. Experimental results showed that this modification increases reliability but also increases efficiency. Another effort toward improving actuator reliability was through electrode shaping and a non-ZNMF (zero-net-mass-flux) design. Increasing the diameter of the electrode

while contouring the tip to a small tip area improved actuator performance especially during high-frequency operation. The addition of an external air supply improved jet momentum while the SparkJet was successfully operated at high-frequency up to 1 kHz.

To support model development and experimental testing, CFD modeling was used to investigate the predicted fundamental physics and flow interactions within and near the SparkJet actuator. Unsteady Reynolds-Averaged Navier-Stokes (URANS) simulations were used to model the flow physics following an arc discharge for both a single orifice and orifice array SparkJet actuator. Under this AFOSR grant, CFD studies focused on the SparkJet orifice array configuration to support wind tunnel testing at FSU/AAPL and the single orifice design to support benchtop studies to predict efficiency. The CFD results were also used for comparison to microschlieren imagery acquired at FSU/AAPL and the 1-D numerical model developed at JHU/APL.

## **Personnel Involved (Duration of Grant)**

JHU/APL: Bohdan Z. Cybyk (Aerospace Engineer), Sarah Popkin (Aerospace Engineer), H. Bruce Land III (Electrical Engineer), Trent Taylor (Aerospace Engineer), Jerry Emhoff (Aerospace Engineer), and John Teehan (Machinist).

## **Publications**

Haack, S., Taylor, T., Emhoff, J., and Cybyk, B., “Development of an Analytical SparkJet Model,” 5th AIAA Flow Control Conference, June 2010, AIAA 2010-4979.

Haack, S. J. and Foster, C. H., “Experimental Estimation of SparkJet Efficiency,” 42nd AIAA Plasmadynamics and Lasers Conference, June 2011, AIAA 2011-3997.

Land III, H. B., Grossman, K. R., Cybyk, B. Z., and VanWie, D. M., “Solid State Supersonic Flow Actuator and Method of Use,” U.S. Patent 7,988,103, August 2011.

Emerick, T., Ali, M., Foster, C., Alvi, F., Popkin, S., and Cybyk, B., “SparkJet Actuator Characterization in Supersonic Crossflow,” 6th AIAA Flow Control Conference, June 2012, AIAA 2012-2814.

Popkin, S. H., Cybyk, B., Land III, H. B., Emerick II, T. M., Foster, C. H., and Alvi, F. S., “Recent Performance-Based Advances in SparkJet Actuator Design for Supersonic Flow Applications,” 51st AIAA Aerospace Sciences Meeting, January 2013, AIAA 2013-0322.

Popkin, S. H., Taylor, T. M., and Cybyk, B. Z., “Development and Application of the SparkJet Actuator for High-Speed Flow Control,” *Johns Hopkins APL Technical Digest*, 32(1), June 2013.

Popkin, S. H., Cybyk, B. Z., Foster, C. H., Alvi, and F. S., “Experimental Estimation of SparkJet Efficiency,” *AIAA Journal* (accepted pending revisions).

Popkin, S. H., *One-Dimensional Numerical Model Development of a Plasma-Based Actuator*, Ph.D. thesis, University of Maryland, 2014.

# Nomenclature

$\alpha$	thermal diffusivity (m <sup>2</sup> /s)
$\beta$	phase constant between the vortex shedding and the acoustic wave response in the cavity (unitless)
$\gamma$	ratio of specific heats (unitless)
$\eta$	efficiency (unitless)
$\rho$	density (kg/m <sup>3</sup> )
$\omega$	frequency (rad/s)
$A$	area (m <sup>2</sup> )
$Bi$	Biot number (unitless)
$C$	capacitance (F)
$C_v$	specific heat for a constant volume (J/kgK)
$C_p$	specific heat for a constant pressure (J/kgK)
$d$	diameter (m)
$D$	depth (m)
$e$	internal energy per unit mass (J/kg)
$E$	internal energy (J)
$f$	frequency (Hz)
$h$	convective heat transfer coefficient (W/m <sup>2</sup> K)
$H$	height (m)
$I$	electric current (A)
$k$	thermal conductivity (W/mK)
$K$	ratio of vortex convection speed to freestream flow speed (unitless)
$L$	length (m)
$m$	mass (kg)
$M$	Mach number
$n$	mode number (unitless)
$P$	pressure (Pa)
$P_0$	total pressure (Pa)
$q$	input power (J/s)
$Q$	input energy (J)
$r$	radius (m)
$R$	specific gas constant (J/kgK)
$t$	time (s)
$T$	temperature (K)
$U$	velocity (m/s)
$v$	cavity volume (m <sup>3</sup> )
$v$	orifice volume (m <sup>3</sup> )
$V$	voltage (V)

## Subscripts

$\infty$	freestream condition
1	Conditions at the beginning of Stage 1
2	Conditions at the beginning of Stage 2
A	arc
c	cutoff
C	capacitance
e	exit
i	spatial discretization
j	temporal discretization
m	measured
M	Macor
n	notional
o	orifice
p	calorically perfect
P	pressure
T	thermally perfect
W	tungsten

## Acronymns

600ET	600 V electrode voltage initiated with an external trigger
600PST	600 V electrode voltage initiated with a pseudo-series trigger
AFC	Active Flow Control
AFOSR	Air Force Office of Scientific Research
CFD	Computational Fluid Dynamics
COMPACT	Combustion Powered Actuator
DBD	Dielectric Barrier Discharge
DST	Digital Speckle Tomography
EMI	Electromagnetic Interference
FFT	Fast-Fourier Transform
FSU/AAPL	Florida State University Advanced Aero-Propulsion Laboratory
JHU/APL	Johns Hopkins University Applied Physics Laboratory
LAFPA	Localized Arc Filament Plasma Actuator
MHD	Magnetohydrodynamic
NASA	National Aeronautics and Space Administration
ONERA	Office National d'Etudes et de Recherches Aérospatiales
PIV	Particle Image Velocimetry
REM	Resonance Enhanced Microjets
URANS	Unsteady Reynolds-Averaged Navier-Stokes
V/STOL	Vertical and/or Short Takeoff and Landing
ZNMF	Zero-net-mass-flux

# 1 Introduction

The ability to ensure safe separation of a weapon from the weapons bay of a supersonic jet or to reduce damaging noise from a jet engine exhaust depends on the ability to locally influence flow within the boundary layer of the high-speed flow environment. Controlling a large-scale, high-speed flow environment requires a flow control device or array of flow control devices which cover a large surface area and have the requisite control authority to manipulate high-momentum flow features. The motivation for this work and any flow control work is to develop, characterize and understand an actuator capable of improving otherwise adverse flow conditions. As a collaborative effort with FSU/AAPL, the work presented in this report focused on developing a device for wind tunnel testing culminating in supersonic flow experiments. Actuator development included numerical modeling, experimental testing, and design optimization for improved SparkJet operability.

## 1.1 Supersonic Open Cavity Flow

The flow control challenges unique to high-speed applications are primarily related to the momentum and frequency requirements. These high-speed flow applications possess high-momentum, high-frequency instabilities within the boundary layer. Before considering the appropriate device and technique to efficiently control flow, the details of each flow condition need to be understood. The application of interest here is unsteady, high-momentum supersonic open cavity flow.

An example of when supersonic open cavity flow can occur includes when an aircraft flying at supersonic velocities opens the bomb bay doors. Figure 1 shows an F-22 Raptor with open bomb bay doors and reveals the internal geometry the flow encounters when opened. Experimental, numerical, and analytical analyses of this flow field use a simplified representation of the open cavity with a characteristic length to depth ratio,  $(L/D)$ . The primary feature of the open cavity flow is a self-sustaining, unsteady flow inside the cavity with a characteristic frequency ( $f$ ) or frequencies based on  $L/D$  and Mach ( $M$ ). The unsteady nature of the flow can prevent reliable store separation or accelerate aircraft structural fatigue. Thus, methods of reducing the unsteadiness are desired. As a result of wind tunnel testing, the frequency, or *tone*, associated with cavity flow was first identified by Rossiter [1] and is, subsequently, known as a Rossiter tone.

The targeted cavity geometry (shown in Figure 2) is characterized by an  $L/D$  of 5.16 in a Mach 1.5 flow. Previous wind tunnel test results show that the front and rear recirculating regions are merged for this cavity flow condition and the first Rossiter tone ( $n = 1$ ) is 1.04 kHz as predicted by Equation 1 with  $K = 0.57$  and  $\beta = 0.25$ [3]. This equation assumes that the cavity speed of sound is equal to the freestream speed of sound. However, following Rossiter's work, Heller [4] determined that the cavity speed of sound is actually equal to the freestream stagnation speed of sound. Therefore, the modified equation for finding the cavity tones is given in Equation 2 and is commonly referred to in recent open cavity research.



**Figure 1:** F-22 Raptor flying with open bomb bay doors[2].

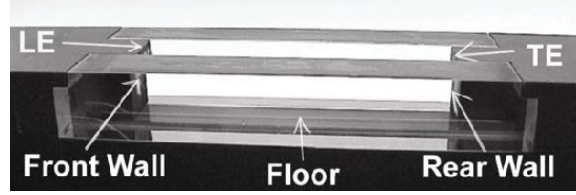


**Figure 2:** Photograph of the supersonic cavity flow model used by FSU/AAPL[3].

$$f = \frac{U}{L} \frac{(n - \beta)}{\left(\frac{1}{K} + M\right)} \quad (1)$$

$$f = \frac{U}{L} \frac{(n - \beta)}{\left(\frac{1}{K} + \frac{M}{\sqrt{1 + \frac{\gamma - 1}{2} M^2}}\right)} \quad (2)$$

Using Equation 2, the 1st, 2nd and 3rd modes ( $n = 1, 2, 3$ ) for the targeted cavity geometry are 0.84, 1.69 and 2.53 kHz. Both passive and active flow control techniques have been applied and demonstrate the ability to suppress these tones. The following section, however, will focus on summarizing the active flow control actuators available for high-momentum unsteady flows similar to the SparkJet actuator.

## 1.2 High-Momentum Flow Control Actuators

In the broadest sense, all flow control devices can be categorized as either passive or active devices. *Passive* devices include fences, ridges, bumps, or other built-in surface modifications which are designed to benefit an adverse flow feature at specific, on-design flow conditions. These devices are useful in volatile flow environments where flow enhancement is desired but moving parts would likely fail and where weight or power requirements would not allow an active device. However, these devices can contribute to a performance penalty.



To eliminate the drag penalty associated with passive devices, a wide variety of *active* flow control devices have also been developed. For high-speed flow, these tend to involve, high-momentum jets or rapid energy deposition using arcs, plasma, and magnetic fields. Devices that use rapid energy deposition include the combustion powered actuator (COMPACT), magneto-hydrodynamic (MHD) actuators, nano-second dielectric barrier discharge (DBD) actuators, and localized arc filament plasma actuators (LAFPAs). High-momentum fluidic devices include synthetic jet actuators, microjet actuators, and resonance enhanced microjet (REM) actuators. This section focuses on the flow control devices and techniques applied to high-speed flows.

Active flow control devices are designed to improve otherwise adverse flow phenomena without physically modifying the aerodynamic surface. In fact, the use of active flow control is sometimes referred to as *virtual shaping*[5, 6, 7, 8]. The most basic forms of active flow control involve steady suction, steady blowing, or combined blowing and suction. These techniques are typically used to control the thickness of the boundary layer and delay flow separation. A disadvantage to operating steady suction or blowing devices is the requirement of an external air supply or a vacuum chamber. Unsteady devices that draw on the external flow environment and eliminate the need for an external air supply are called ZNMF devices.

Applied specifically to high-speed flows, an actuator called a microjet has been utilized for both supersonic open cavity flow and impinging jet noise. Microjets, developed by Florida State University, are steady jets supplied with high pressure air. When arranged in an array, a single supply pressurizes a chamber and forces air through multiple orifices. Microjets have been applied to two high-speed applications: open cavity flow and jet noise. To control noise and the unsteady shear layer motion associated with a supersonic open cavity, an array of 12 microjets with a 0.4 mm orifice diameter were placed at the leading edge of the cavity[3]. The length-to-depth and length-to-width aspect ratio of the cavity are  $L/D = 5.16$  and  $L/W = 5.92$ , respectively, in a Mach 2.0 crossflow. Using shadowgraph, particle image velocimetry (PIV) and unsteady acoustic pressure measurements, the effect of microjets over a range of nozzle pressure ratios, demonstrated the ability of the microjets to reduce broadband noise up to 9 dB and tonal noise up to 20 dB. REM actuators were derived from microjets but operate with an inherent unsteadiness to target natural unsteadiness in a flow-field. Development of REM actuators is fairly recent but application oriented experimental tests have demonstrated the ability of the REM actuators to produce an unsteady influence on Mach 1.5 flow over a flat plate[9] and reducing broadband and impingement tone noise levels[10, 11].

While reducing noise levels is beneficial, another purpose of controlling supersonic cavity unsteadiness is to ensure safe store separation. To that end, wind tunnel tests were conducted to determine the efficacy of microjets creating a flow environment suitable for store separation. As part of the High Frequency Excitation (HIFEX) program funded by the Defense Advanced Research Projects Agency (DARPA), wind tunnel testing was conducted to evaluate the effectiveness of microjets on a cavity flow field in Mach 2.5 flow[12]. The results of this study showed that the microjet array in conjunction with a jet screen upstream of the

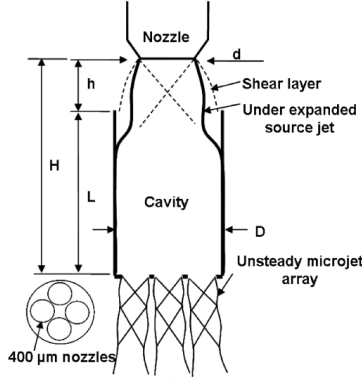


**Figure 3:** Sketch of REM design sizing parameters for unsteady REM actuation[14].

microjet array provided the best control using the least mass flow. The combination of flow control techniques is considered a *tandem array* and was used to control store separation on a full-scale test at the high-speed track at Holloman Air Force Base[13]. The full-scale test confirmed that safe store separation could be achieved at Mach 2 with the use of combined passive and active flow control.

Several other types of active flow control devices could be applied to open cavity flow due to their high-momentum output. One such high-momentum flow control device is the COMPACT, developed by Georgia Institute of Technology, which uses a small combustion process inside a cavity that ejects high-speed air through an orifice. This device ignites a mixture of air and hydrogen with a spark to increase cavity pressure[15]. Peak cavity pressure is achieved between 1 and 3 ms after combustion is initiated and a cycle completes in approximately 4-10 ms depending on the design parameters. The COMPACT has been used successfully to delay flow separation over a 2-D airfoil[16] and a 3-D rotorcraft fuselage[17].

A different group of actuation techniques is the use of electric or magnetic energy to produce fluid motion. A LAFPA involves a sudden energy deposition in the form of an arc discharge between two electrodes. The arc discharge produces significant heat via Joule heating which results in a blast wave and a local heat addition to the flow[18]. This device is similar to the SparkJet except that the LAFPA arc is not enclosed in a cavity but rather open to the flow and recessed in a groove to shield the arcs from the high-speed flow[19]. The electronics that support LAFPA operation use a ramped voltage up to 10 kV which creates a spark that is sustained by up to 0.25 A when an array of eight LAFPAs are in use. LAFPAs have been primarily applied to jet noise mitigation[20] and high-speed jet control[21] but also to shock wave boundary layer interaction control for supersonic inlets[22].

The SparkJet actuator shares some commonalities with the above mentioned AFC devices. Specifically, the SparkJet uses an arc discharge similar to the LAFPA, produces a fluidic jet similar to the microjet actuator, and produces an unsteady jet similar to the COMPACT and a synthetic jet actuator. As a ZNMF device with no moving parts, however, no single device shares the same characteristics of the SparkJet such that it represents a device with

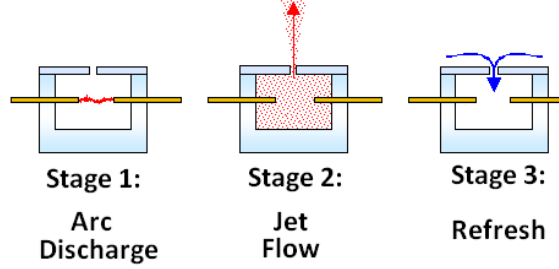


**Figure 4:** Basic schematic of the three stages of SparkJet operation.

the ability to have a unique influence on high-speed flow applications[23].

This section described the need for high-speed flow control and the devices developed with the intention of controlling high-speed flow. The following section outlines the basic functionality of the SparkJet actuator and describes previous work performed by JHU/APL and current work performed by several other organizations all in an effort to understand the SparkJet actuator. The present report summarizes the contributions made toward understanding SparkJet operation through numerical modeling, experimental testing, and design optimization under a five-year AFOSR grant. The work conducted by JHU/APL feeds into the critical efforts by FSU/AAPL to demonstrate the SparkJet in supersonic flow applications.

### 1.3 SparkJet Actuator

The SparkJet is a solid-state device containing no moving parts and has no external air supply making it a ZNMF device. It consists of a cavity with embedded electrodes and an orifice through which air can pass freely. The operation of the SparkJet is illustrated in Figure 4 as a series of stages. The operation begins with a brief arc discharge within the cavity to produce hot, high-pressure plasma and air (Stage 1). The second stage of operation consists of the venting of high-pressure plasma and air through the orifice, which converts the thermal energy of the discharge into kinetic energy (Stage 2). The third stage of the operation consists of a cooling/refresh phase (Stage 3) prior to the beginning of the next arc discharge (Stage 1).

The basic SparkJet cycle is dependent on a multitude of parameters including the magnitude of energy deposition; actuation frequency; orifice area and shape; cavity volume and shape; electrode spacing, diameter, and shape; and cavity wall thermal properties. When considering flow applications, an array of SparkJets interacting with external flow conditions will be dependent on external, local flow conditions (pressure, temperature, velocity, inherent instability frequency). Also, the number of and spacing between collocated SparkJets would affect spatial and temporal interactions between devices. Further design parameters can include the actuation frequency relative to natural instabilities in the external flow, phasing actuation of adjacent actuator arrays (if individually programmable), and alignment of nearby orifices. The physics and other details pertaining to each stage are described in the following sections.

## Stage 1 - Arc Discharge

The primary goal of Stage 1 is to raise the cavity air temperature and pressure quickly and with maximum efficiency. The method of satisfying this goal is by the use of a brief, high-current arc discharge sustained by a charged capacitance parallel to the anode and cathode. The maximum amount of input energy,  $Q_C$ , is controlled by the capacitance,  $C$ , and voltage,  $V$ , according to Equation 3. Another parameter important to understanding Stage 1 is the internal cavity energy,  $E$ , just before the spark discharge as given in Equation 4. At this point, a valuable parameter  $Q_C/E$  can also be defined which provides a sense of the amount of energy stored in the SparkJet cavity prior to Stage 2. This parameter is simply the ratio of input energy to the internal cavity energy as shown in Equation 5.

$$Q_C = \frac{1}{2}CV^2 \quad (3)$$

$$E = mC_vT \quad (4)$$

$$\frac{Q_C}{E} = \frac{1/2CV^2}{mC_vT} \quad (5)$$

The method of initiating the arc discharge is through a high-voltage, low-current trigger spark. In the very first SparkJet device, Stage 1 was initiated by increasing the voltage across the anode and cathode until the breakdown voltage between the electrode tips was exceeded and the trigger spark was initiated. However, this technique posed problems when attempting to acquire characterization data because the time between the voltage increase and the arc discharge would vary making it difficult to capture. Therefore, the initiation technique changed to the use of a trigger spark between the trigger electrode and the cathode, which was achieved using an external trigger circuit. This work includes yet another modification to the trigger mechanism, which improves reliability and efficiency.

Regardless of the exact trigger setup, once the trigger mechanism induces the capacitive arc breakdown, the rest of Stage 1 involves the conversion of capacitor energy into Joule heat and raising the cavity pressure. The energy that increases the temperature and, therefore, pressure in the SparkJet cavity is of most interest to SparkJet performance. However, a performance assessment requires some focus on inefficiencies. The sources of these inefficiencies are discussed in Section 4 using comparisons between experimental data and modeling solutions. Once the arc discharge is complete and the temperature and pressure of the air in the cavity have reached their maximum values, Stage 1 is complete.

## Stage 2 - Jet Flow

The SparkJet fluidic jet formation and flow is a very unsteady process initiated by the sudden, large pressure gradient across the orifice face generated by high-temperature and high-pressure cavity air from Stage 1. As the cavity air is forced through the orifice, the cavity pressure decreases due primarily to the decrease in cavity density and secondarily to the convective thermal heat transfer. Therefore, some level of thermal modeling is required during Stage 2. Collaborative efforts with FSU/AAPL have enabled the acquisition

of microschlieren imagery of the early jet development. Figures 5(a) and 5(b) show microschlieren images of the SparkJet flow  $12\ \mu\text{s}$  and  $100\ \mu\text{s}$ , respectively, after Stage 1 was initiated. These images show that the first evidence of the SparkJet formation is a blast wave (called a precursor shock by other researchers[24]) which appears only  $6\ \mu\text{s}$  after Stage 1 initiates. Immediately following the blast wave is the jet front which, over the course of  $100\ \mu\text{s}$  develops into a fully turbulent jet. By phase-averaging multiple images, evidence of locally supersonic flow is apparent[25].

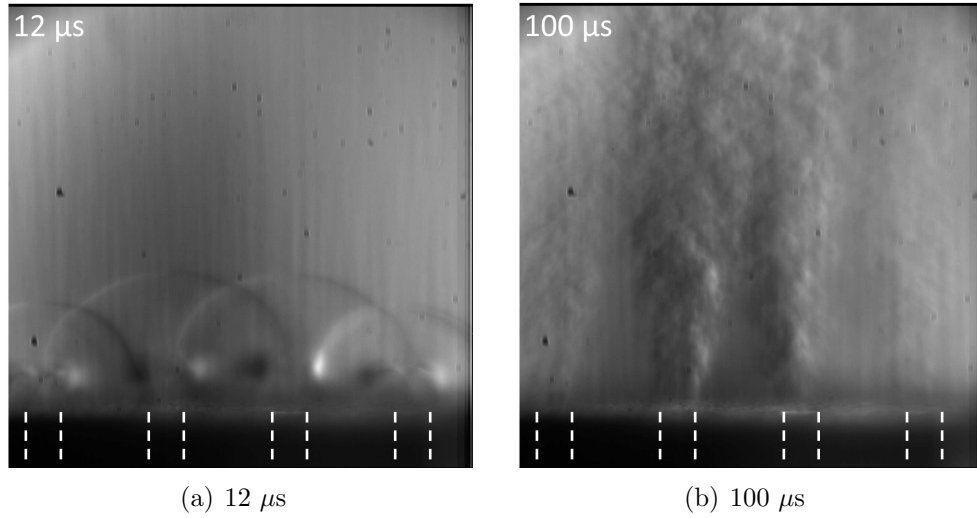


**Figure 5:** Microschlieren images at two time delays after Stage 1 initiation showing the a) blast wave and b) turbulent jet formation in the early portion of Stage 2[25].

The duration of Stage 2 is primarily controlled by the cavity volume and the orifice area. In general, decreasing orifice area and increasing cavity volume increases the duration of Stage 2. The jet formation can also be affected by contouring the orifice throat. The studies presented in this report use a constant area orifice, but other studies have investigated a converging orifice[24] and a converging-diverging orifice[26] to increase jet Mach number. Near the end of Stage 2, the cavity pressure decreases to ambient pressure. At this point, the jet momentum through the orifice is low, but not yet zero. As the jet momentum continues to carry air out of the cavity, the cavity pressure decreases below ambient pressure. As a result, an adverse pressure gradient develops across the orifice, which reduces the jet momentum. When the jet momentum is zero, Stage 2 is complete.

### Stage 3 - Refresh

Finally, once the fluid momentum at the orifice face is zero, the decreased pressure in the cavity forces the flow to reverse and increases the pressure and density of the cavity air. In addition, the ingestion of the relatively cool external flow and mixing with the high-temperature cavity air reduces the overall cavity temperature. Further reduction in cavity temperature occurs due to free convection of the air to the cooling cavity walls and electrodes. Thermal heat transfer continues to exist during this stage. The primary parameters

that affect the duration of Stage 3 are orifice diameter and the thermal conductivity of the walls and electrodes.

Stage 3 typically lasts long enough to raise concerns about SparkJet frequency limitation. For example, if the time from Stage 1 to the end of Stage 3 exceeds 1 ms and an actuation frequency of 1 kHz is desired, the second arc discharge will occur when the cavity density is lower and the temperature is higher than when the first arc discharge occurred. While this leads to a higher  $Q_C/E$  value (due to a lower  $E$  value), the lack of cavity density and mass leads to a lower momentum output during Stage 2 and a decreased ability to affect the external flow. One method to decrease the refresh time is to construct the actuator housing with material possessing a high thermal conductivity. Another method would be to provide an external source of air to refill the cavity; however, this method would detract from the appeal of the current ZNMF property of the SparkJet.

## State of the Art

Prior to the work presented in this report, previous studies had taken place at JHU/APL to study the SparkJet and its performance[27, 28, 29, 30, 31]. In addition, several other organizations have been conducting independent evaluations of SparkJet device (or similar) performance. Modeling and experimental efforts are needed to improve the fundamental understanding of the SparkJet flow physics, to characterize device operation, and to enable actuator array design. The following paragraphs outline analytical modeling, numerical modeling, and experimental testing efforts performed by other organizations including references.

## Analytical Modeling

The desire to simplify the complexities of the SparkJet process is evident by the efforts outlined in this section to produce an analytical model. In 2012, Anderson and Knight at Rutgers University documented a one-dimensional, analytical model which included an in-depth dimensional analysis[32]. Anderson's model and the early JHU/APL modeling efforts are similar in that they simplify the SparkJet to a 1-D representation, assume calorically perfect gas, inviscid flow, adiabatic walls, and prescribed, instantaneous energy input. Based on these assumptions, the model seeks to quantify several performance parameters based on fluidics. This study considers a single cycle with limited discussion of Stage 3 operation. Therefore, this model is not capable of capturing high-frequency actuation.

## Computational Modeling

Higher-fidelity simulations of the SparkJet actuator involve analysis using CFD. Several organizations have conducted CFD studies of the SparkJet actuator including Rutgers University and the Office National d'Etudes et de Recherches Aérospatiales (ONERA). At Rutgers University, Anderson and Knight used a finite volume code called GASPex (export version of GASP) to simulate the SparkJet flow[33]. The simulation efforts considered a single SparkJet (called *plasma jet* in the paper) interacting with both a quiescent flow and a Mach 3 crossflow

with a turbulent boundary layer. The quiescent flow cases considered the plasma jet performance for a range of input energy levels,  $Q_C$ , while the crossflow simulations considered the effect of orifice diameter,  $d_o$ , on the plasma jet impulse. Comparisons were made between the computational simulations and the Rutgers-developed analytical model. Results showed that the analytical model and computational simulation agree very well for interactions with a quiescent flow. The Mach 3 turbulent crossflow cases show that the impulse generated by the SparkJet is significantly affected by the flow environment. For example, the impulse generated in quiescent flow was compared to the impulse generated in the supersonic crossflow and results showed that the impulse is significantly lower for the quiescent flow than the supersonic crossflow case. While the simulations showed that the jet velocity at the orifice is lower for the crossflow case than the quiescent case, the difference in impulse is primarily due to the longer jet duration in the crossflow case.

ONERA has conducted a two-dimensional, axisymmetric, URANS simulation of the SparkJet (called a *plasma synthetic jet* (PSJ)) interaction with a quiescent flow and a crossflow assuming a prescribed input energy using their in-house CFD code called CEDRE CFD[26]. Follow-on work also included simulation of the arc discharge[34]. The CFD analysis was used to study the effect of shaping the PSJ orifice and cavity shape for a fixed volume. Results showed, not surprisingly, that a converging-diverging nozzle provides the best PSJ performance based on exit Mach number. The parametric cavity shape simulations showed that the height to diameter ratio of the cavity primarily affect the influence of viscous effects. The simulations also show that walls with high conductive thermal heat transfer lead to shorter refresh durations. Three-dimensional, URANS simulations of the PSJ interacting with a relatively low-speed (21.5 m/s) crossflow and preliminary comparisons to experimental data verified that the simulation captures the pair of vortices surrounding the jet orifice and the jet penetration of the boundary layer.

## Experimental Characterization

While simulations and modeling have estimated the potential strength and usefulness of the SparkJet actuator, experimental tests have been conducted to confirm the modeling results. As seen with the modeling efforts, several other organizations have experimentally tested the SparkJet including the University of Texas at Austin, ONERA, the University of Illinois, the National Aeronautics and Space Administration (NASA) Langley Research Center (LaRC) and the University of Florida. The experimental studies conducted by each institution are discussed in the following paragraphs.

At the University of Texas at Austin, the so-called *pulsed plasma jet* (PPJ) actuator design was similar to the SparkJet in that an arc within the cavity initiated the synthetic jet. However, the PPJ actuator was limited to operation in very low pressures (45 torr). The actuator design included electrode gaps up to 5 mm and the arc current was controlled such that it was maintained for 20 – 50  $\mu$ s at 1.1 - 3.9 A[35]. Experimental testing was primarily based on schlieren imagery in addition to planar laser scattering (PLS) of flow interactions with quiescent and a Mach 3 flow over a 30° corner. While differences in design and operating conditions exist between the SparkJet and the PPJ, the experimental results demonstrated

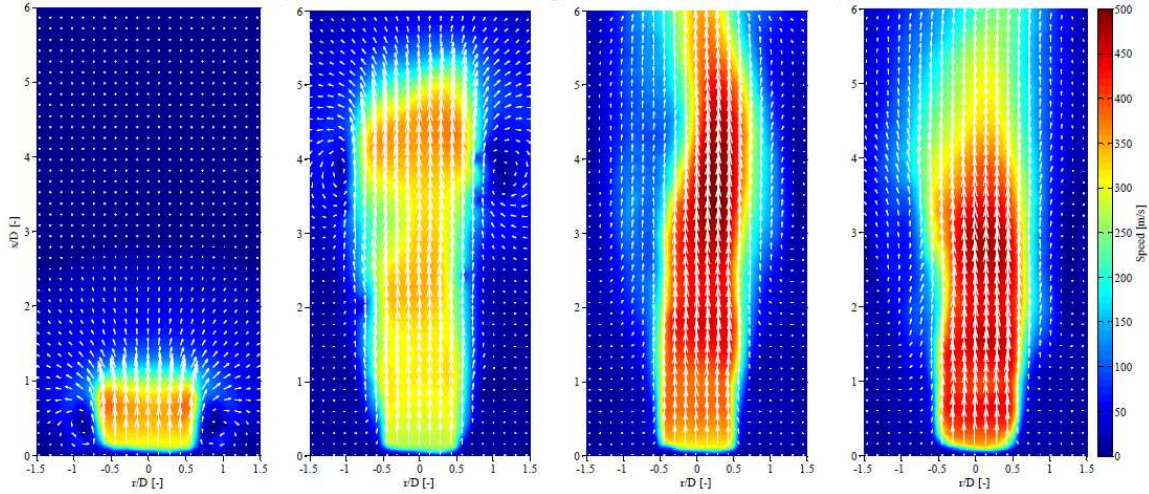


**Figure 6:** Average velocity field contours and vectors for the  $25\mu\text{F}$  discharge at  $30\mu\text{s}$ ,  $50\mu\text{s}$ ,  $70\mu\text{s}$ , and  $90\mu\text{s}$  delay times[24].

important flow interactions. The primary discovery was that the flow responsiveness was directly related to the frequency of the actuator, and the PPJ had the most effect on the separation bubble at the compression corner when placed upstream of the separation bubble. These results demonstrated the ability of such an actuator to control the frequency of fluid structures at Mach 3 flow conditions.

At the University of Illinois, both quiescent and Mach 3 crossflow experiments were conducted. The actuator design used for these studies was very similar to the SparkJet but the researchers refer to the actuator as a PPJ actuator. For the quiescent flow studies[24], schlieren and PIV images were used to characterize the PPJ actuator flow over a wide range of input energy values controlled by the capacitance values of  $0.25\mu\text{F}$ ,  $2\mu\text{F}$ ,  $25\mu\text{F}$  and  $68\mu\text{F}$ . The results show that the PPJ actuator flow starts with a blast wave (referred to as a precursor shock) with a velocity independent of the energy deposition level. The contact surface (i.e. jet front) velocity, however, increases with input energy.

University of Illinois acquired PIV images[24] which are very revealing of the PPJ actuator flow, and the method of seeding the ambient flow is a clear improvement over previous PIV efforts[30, 36]. Figure 6 shows the velocity field contours of the PPJ actuator flow at  $30\mu\text{s}$ ,  $50\mu\text{s}$ ,  $70\mu\text{s}$  and  $90\mu\text{s}$  delay times for a capacitance of  $25\mu\text{F}$ . The maximum flow velocity easily exceeds the speed of sound based on ambient temperature; however, shock cells are not visible because the local temperature in the jet is higher than the ambient temperature such that the local Mach number is below unity. Further data processing of the PIV images show that beyond  $90\mu\text{s}$ , the jet velocity gradually decreases. The magnitude of the velocity is proportional to the magnitude of energy deposition as is the jet duration.

The Mach 3 crossflow studies conducted by the University of Illinois used PIV and schlieren to investigate the interaction between a single PPJ actuator in a Mach 3 crossflow[37]. The results showed that the PPJ actuator, using  $2\mu\text{F}$  across the anode and cathode weakly



affected the crossflow. The PIV results showed that the maximum velocity perpendicular to the crossflow from the PPJ actuator was 60 m/s. The primary conclusion from this work was that further investigation is needed to understand the weak influence.

Extensive experimental work related to the PSJ has been carried out by ONERA[26, 38]. Experimental tests characterized the PSJ design as a function of cavity wall thermal conductivity, orifice diameter, frequency, and input energy. The PSJ design was very similar to the first SparkJet design by JHU/APL which contained a center anode and used a metal lid as the cathode. The experiments examined the effect of the orifice diameter, lid material, and frequency on the pressure rise in the cavity. The results showed that as orifice diameter decreases and actuation frequency increases, the pressure rise in the chamber decreases. They also show that as actuation frequency increases and lid thermal conductivity decreases, the pressure rise also decreases. These results suggest that maintenance of a prescribed pressure rise in the cavity at high actuation frequencies requires a reduction of Stages 2 and 3. This result translates to a larger orifice diameter and thermally conductive walls. ONERA also performed experiments testing a single PSJ in a wind tunnel to examine interactions between a pitched and skewed PSJ and a 40 m/s crossflow. Results showed that the PSJ influences the flow much like a synthetic jet or vortex generator. Experimental testing was also conducted to study the interaction between a PSJ and a high subsonic jet (Mach 0.6 and 0.9). Based on schlieren imagery, the PSJ clearly affects the jet shear layer and demonstrates potential for control jet noise.

Only very recently, NASA LaRC (in collaboration with Rutgers University) has begun testing the SparkJet actuator in quiescent flow[39]. The purpose of the experiments was to measure the impulse (and efficiency) provided by the SparkJet by fixing the SparkJet to the end of a pendulum and measuring the displacement. The measured displacement was converted to an impulse and then compared to an analytical model created by Anderson and Knight at Rutgers University[32]. The results showed that the actuator design used for this study provided an angular deflection up to  $0.015^\circ$  which corresponded to only an 8% efficiency. This low efficiency value is most likely due to the small electrode gap coupled with a relatively high voltage potential and voltage potential drops in the long cables connecting the actuator to the power supply.

## 2 Simplified Numerical Modeling

A major effort during this grant was developing a simplified numerical model to describe the SparkJet operation and, through variation of several design and operating parameters, understand how to optimize the design for high-frequency operation. The development of a one-dimensional analytical model began in 2003[28]. A three-stage model for the initial energy deposition, isentropic choked jet flow followed by unchoked jet flow, and preliminary refresh stage was presented. A similar approach is used in this section by modeling the SparkJet according to the three stages of operation. Each stage of the SparkJet cycle (shown in Figure 4) is analyzed separately, and pressure, temperature, and density are assumed averaged over the entire cavity volume. Figure 7 shows a sketch of the control volume used

to analyze the SparkJet; the jet velocity is assumed significant only in the orifice volume and zero in the cavity. For the specific case of a SparkJet with an orifice diameter of 1 mm, a cavity volume of 42.4 mm<sup>3</sup>, and total spark energy of 0.089 J, both CFD and 1-D numerical modeling are used to characterize the SparkJet.

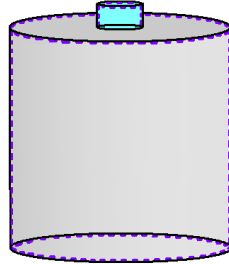


**Figure 7:** Sketch of the assumed control volume where the larger gray cylinder represents the cavity volume and the smaller blue cylinder represents the orifice volume.

## 2.1 Supporting CFD Simulations

To understand general SparkJet performance with a high-fidelity simulation, CFD simulations were conducted for a single cavity and orifice design but with varying input energies. The simulations conducted for this grant solve the flow physics of a 2-D axisymmetric shape using URANS equations. The reader is directed to previous work[40] for further details on the simulations. The major assumptions for these simulations were an isothermal wall, thermally perfect gas and no radiative heat transfer. Figure 8 shows a zoomed view of the grid in the SparkJet cavity, orifice, and external flow.

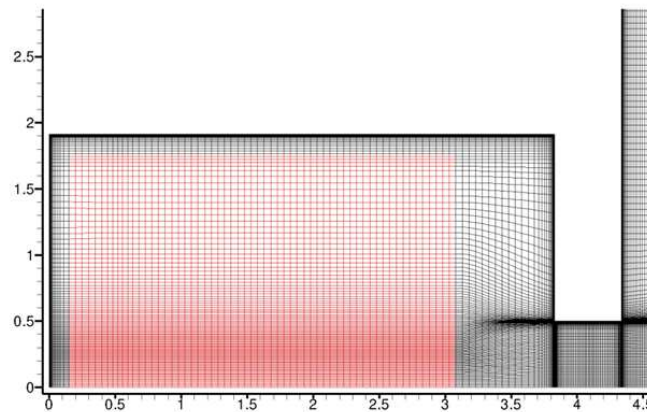


**Figure 8:** Structured, axi-symmetric grid representation of the SparkJet internal geometry with grid axis units in millimeters. The red section represents the grid cells raised to an elevated temperature and pressure to represent the energy deposition in Stage 1.

Relatively short duration ( $\approx 500 \mu\text{s}$ ) simulations, focused on the initial pressure rise, were

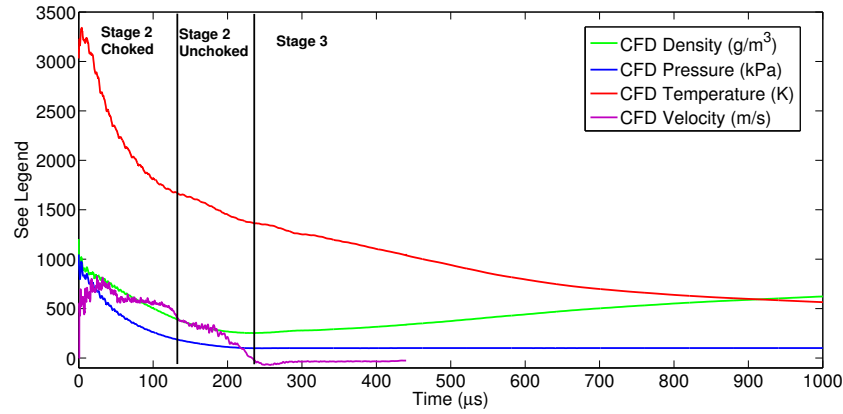


**Figure 9:** Time-dependent CFD simulation of the volume-averaged cavity pressure, temperature, and density and area-averaged jet velocity through the orifice.

conducted over a range of energy deposition efficiencies and ended near the start of the refresh cycle. The cavity air was initialized at rest, a temperature of 288 K, and a pressure of 101325 Pa. The red section of the grid was kept at the same density and at rest but was initialized at an elevated pressure and temperature to model Stage 1 of the SparkJet actuation cycle. To truly represent the arc discharge, the red section would ideally be confined to a very small region near the center of the cavity. However, CFD solution convergence was improved by expanding the red section of the grid until the temperature difference inside and outside the red section resulted in good convergence. Once the initial conditions were defined, the solution was run in a time-accurate manner. A separate region at the base of the cavity that was the width of the experimental dynamic pressure sensor described in Section 3 was defined. The pressure sensor region was then used to track the area-averaged pressure for the sensor versus time to compare with experimental data. Comparisons to the experimental data are discussed in Section 4.

In addition to comparison with experiment, comparison to the 1-D numerical model was also achieved by calculating the volume-averaged pressure, temperature, and density in the cavity as well as the area-averaged velocity in the orifice. Figure 9 shows these time-dependent values as a result of the CFD simulation. After the initial pressure and temperature rise, the orifice velocity increases which leads to the decrease in cavity density. As the jet flow continues, the pressure and temperature also decrease. Once the velocity reaches zero, the refresh stage starts by the gradual increase in cavity density. As the density increases, the relatively cool air is drawn into the cavity which quickly decreases the cavity temperature. The cavity pressure remains just below ambient pressure which forces the refresh stage to continue. The pressure gradient is primarily maintained by the continued convective heat transfer at the walls. These trends and values will be compared to the 1-D model to justify the assumptions made during development of the simplified model.

## 2.2 Governing Equations

The governing equations used to model the SparkJet cycle involve basic thermodynamics and fluid dynamics. Thermodynamics are used to simplify the plasma chemistry involved in the arc discharge. The fluid dynamics are represented by a 1-D derivation of the Euler equations. A summary of the resulting equations is given in this section.

### Stage 1

To initiate Stage 1 of the cycle, an instantaneous energy input from the capacitive arc discharge is used to determine the peak temperature inside the cavity by Equation 6. The total energy contained in a capacitive arc was given in Equation 3. Using the ideal gas law (Equation 7) and under the assumption that no mass has exited the cavity during this instantaneous energy addition, the peak pressure is also determined.

$$T_2 = T_1 \left( 1 + \frac{Q_C}{E} \right) \quad (6)$$

$$P_2 = \rho R T_2 = \rho R T_1 \left( 1 + \frac{Q_C}{E} \right) \quad (7)$$

### Stage 2

To initiate Stage 2, the peak temperature ( $T_2$ ) and pressure ( $P_2$ ) from Stage 1 are used as initial conditions and no more arc energy is added to the system. The unsteady Euler equations, separately identified as the conservation of mass, momentum and energy equations, are used to describe the change in cavity conditions for Stage 2. Equations 8-10 are the complete, integral form of the conservation equations.

$$\frac{\partial}{\partial t} \iiint_v \rho dv + \iint_S \rho \mathbf{U} \cdot d\mathbf{S} = 0 \quad (8)$$

$$\frac{\partial}{\partial t} \iiint_v \rho \mathbf{U} dv + \iint_S (\rho \mathbf{U} \cdot d\mathbf{S}) \mathbf{U} = - \iint_S p d\mathbf{S} + \iiint_v \rho \mathbf{f} dv + \mathbf{F}_{viscous} \quad (9)$$

$$\begin{aligned} & \frac{\partial}{\partial t} \iiint_v \rho \left( e + \frac{U^2}{2} \right) dv + \iint_S \rho \left( e + \frac{U^2}{2} \right) \mathbf{U} \cdot d\mathbf{S} \\ &= \iiint_v \dot{q} \rho dv + \dot{Q}_{viscous} - \iint_S p \mathbf{U} \cdot d\mathbf{s} + \iiint_v \rho (\mathbf{f} \cdot \mathbf{U}) dv + \dot{W}_{viscous} \end{aligned} \quad (10)$$

Under the following assumptions, Equations 11 - 13 are derived and used to solve for the time-dependent SparkJet flow and cavity conditions. While some assumptions are easily accepted (body forces and SparkJet dimensions), most of these assumptions are not as easily accepted and the success or failure of these assumptions are addressed through comparison to CFD simulations and experimental results.

- Inviscid flow
- No body forces
- Calorically perfect ( $e = C_v T$ ) and ideal gas ( $P = \rho R T$ )
- Pressure, temperature, and density are volume-averaged in the cavity
- Velocity is volume-averaged scalar in the orifice volume/throat and area-averaged scalar over the orifice cross-sectional area (velocity is assumed to be negligible in the cavity)
- Pressure gradient across orifice is defined as  $p = P - P_e$  (exit pressure)
- SparkJet dimensions (cavity and orifice volumes and areas) are fixed in time

$$\frac{\partial \rho}{\partial t} = - \left( \frac{\rho U A_o}{v} \right) \quad (11)$$

$$\frac{\partial U}{\partial t} = \frac{1}{\rho} \left( \frac{-(P - P_e) A_o - \rho U^2 A_o}{v_o} - U \frac{\partial \rho}{\partial t} \right) \quad (12)$$

$$\frac{dP}{dt} = \frac{(\dot{q} \rho v - (P - P_e) U A_o - \rho (C_v T + \frac{1}{2} U^2) U A_o - v_o (2 \rho U \frac{dU}{dt} + U^2 \frac{d\rho}{dt}))}{\left( \frac{v C_v}{R} \right)} \quad (13)$$

During Stage 2, the jet flow experiences both a choked and unchoked flow condition. Using the isentropic pressure ratio equation (Equation 14) and knowing that choked flow corresponds to Mach 1 flow, the pressure ratio for choked flow can be determined. Therefore, Stage 2 is segmented into a choked flow condition followed by unchoked flow depending on the pressure ratio between the cavity pressure and the ambient pressure. Assuming a specific heat ratio,  $\gamma = 1.4$ , the solution at Mach 1 shows that if the pressure inside the cavity is above  $1.893 P_\infty$ , the flow is considered choked and the pressure boundary condition at the orifice exit is set to  $P_e = P/1.893$ . Otherwise, the pressure at the orifice is equal to the ambient pressure for unchoked flow ( $P_e = P_\infty$ ). Stage 2 ends with zero orifice velocity and high temperature, low density, and slightly below ambient pressure air inside the cavity.

$$\frac{P_0}{P} = \left( 1 + \frac{\gamma - 1}{2} M^2 \right)^{\frac{\gamma}{\gamma - 1}} = \left( 1 + \frac{\gamma - 1}{2} \right)^{\frac{\gamma}{\gamma - 1}} = 1.893 \quad (14)$$

### Stage 3

During Stage 3, the cavity is refreshed with relatively cool, high-density, ambient air due to the slight pressure gradient across the orifice which is maintained by the continued heat transfer to the internal cavity surfaces. The original JHU/APL analytical model[28] did not attempt to capture Stage 3. As heat transfers to the SparkJet walls and electrodes, the air loses heat, which maintains a slight pressure gradient that continues to draw in air to increase the density to ambient. Since the pressure gradient is low throughout Stage 3, no choked flow assumptions are made. The derivation and equations described for Stage 2 are identical to those used to simulate Stage 3 except where the equations describe the flow passing through

the orifice. Therefore, the surface integrals in the original conservation equations depend on ambient conditions rather than cavity conditions. Equations 15 through 17 are used during Stage 3.

$$\frac{d\rho}{dt} = - \left( \frac{\rho_\infty A_o U}{v} \right) \quad (15)$$

$$\frac{dU}{dt} = \frac{1}{\rho_\infty} \left( \frac{(P - P_\infty) A_o - \rho_\infty U^2 A_o}{v_o} - U \frac{d\rho}{dt} \right) \quad (16)$$

$$\frac{dP}{dt} = \frac{(\dot{q}\rho v - (P - P_\infty) U A_o - \rho_\infty (C_v T_\infty + \frac{1}{2} U^2) U A_o - v_o (2\rho_\infty U \frac{dU}{dt} + U^2 \frac{d\rho}{dt}))}{\left( \frac{v C_v}{R} \right)} \quad (17)$$

## Thermal Modeling

The thermal effects during a single SparkJet cycle require consideration of each heat transfer mechanism: radiation, convection, and conduction. Based on extensive spark and arc discharge literature, the typical plasma temperatures reached for an arc in local thermal equilibrium at 1 atm are between 5000 and 30000 K. At such high temperatures, radiative heat transfer effects require attention. According to Section 10.9.5 in Raizer[41], “radiative losses make up from one to several percent of the power input” in air at a pressure of 1 atm. Also, with the intention of investigating an electrical discharge such as that during Stage 1, both ONERA[34] and UT Austin[42] have also provided numerical results based on a 2-D axisymmetric grid that also support the low losses due to radiative heat transfer. Therefore, radiative heat transfer in air at 1 atm is considered negligible for this thermal modeling.

Assuming the radiative losses are not significant, the remaining heat transfer mechanisms are conduction and convection. During the initial arc discharge, the primary mechanism is thermal conduction to the surrounding air and the electrodes. As the air is rapidly heated, an expanding, cylindrical blast wave emanates from the arc column. In the case of the SparkJet, the thermally conducting blast wave expands until it reaches the SparkJet walls. The subsequent pressure waves interact with the walls resulting in unsteady heat transfer. The frequency of this heat transfer primarily depends on the cavity dimensions. Also, because the cavity geometry does not match the blast wave geometry, areas of the walls not perpendicular to the blast wave direction of travel will also experience convective heat transfer as the fluid “slips” along the surface of the walls. The convective heat transfer coefficient used in the 1-D modeling is based on comparison between the 1-D model and CFD simulation results. Therefore, the thermal heat transfer during the SparkJet cycle includes concurrent conductive and convective heat transfer.

To properly model the thermal heat transfer process, the thermal energy transferred to the walls needs to be calculated from the beginning in Stage 2 since the discharge is complete or nearly complete by the time Stage 2 is underway. There are a variety of thermal models available depending on the assumptions that can be made. Balancing simplicity and unsteady thermal effects, the lumped capacitance model is appealing. This model first uses

the Biot number (Equation 18) to determine the validity of using this method. If the Biot number is less than 0.1, the lumped capacitance method is considered valid. Physically, a low Biot number means that the spatial temperature distribution across the wall is constant such that conductive heat transfer is far more significant than convective heat transfer. The typical SparkJet device is made of Macor walls and tungsten electrodes. Therefore, the SparkJet walls offer two thermal heat transfer paths corresponding to each material. Two values for the Biot number are determined, and both should be less than 0.1 to have confidence in the lumped capacitance method. The Biot number is approximately 0.44 for Macor and 0.004 for tungsten assuming the convective heat transfer coefficient,  $h$ , is 125 W/m<sup>2</sup>, the characteristic length (wall thickness),  $L$ , is 4 mm, and thermal conductivity of Macor,  $k_M$ , and tungsten,  $k_W$ , are 1.46 W/mK and 173 W/mK, respectively. The low thermal conductivity of Macor leads to a more substantial Biot number.

$$Bi = \frac{hL}{k} \quad (18)$$

Another commonly used thermal modeling method is based on thermal resistance. This method assumes that the system has reached a thermal steady-state condition and that the spatial thermal distribution is linear through the walls. While the SparkJet thermal condition is not steady-state, the modeling solution can be solved for every time step such that within each time step, the system is considered in a steady-state condition. The wall temperature values from the previous time step can be carried over to the next step to determine new heat transfer values.

Both the lumped capacitance and thermal resistance methods include features of interest for modeling SparkJet heat transfer. Therefore, these techniques are combined and a representative thermal circuit is used to model the thermal heat transfer and monitor the wall temperature. The general sequence of heat transfer begins with convection from the cavity air to the interior cavity surfaces, followed by parallel thermal conduction through the cavity materials, and completed by thermal convection from the exterior SparkJet surfaces to the ambient air temperature. The thermal energy source is represented electrically by an ideal voltage source. The cavity air temperature is represented by the equivalent voltage,  $T_A$ . This value will be used to link the thermal model to the fluid dynamic model described in the previous sections. The only means of heat transfer from the air to the Macor and tungsten is through thermal convection, which is represented by a resistor,  $R_{h,in}$ . The voltage labeled as  $T_{w,in}$  represents the interior wall temperature assuming the wall temperature of the Macor and tungsten are equivalent. The thermal conduction through the Macor and tungsten is represented by two parallel thermal resistances,  $R_M$  and  $R_W$ , respectively. The voltage labeled as  $T_{w,out}$  represents the exterior wall temperature. The final thermal heat transfer mechanism, thermal convection, is represented as a resistor,  $R_{h,out}$ . All thermal heat transfer mechanisms ultimately reach electrical ground or,  $T_\infty$ , the ambient air temperature.

Once the thermal circuit has been defined, the value of each electrical component needs to be determined. The thermal resistance of Macor and tungsten are given in Equations 19 and 20, respectively. The thermal resistance associated with convective heat transfer are given in Equations 21 and 22. The ability of a material to store thermal energy is represented by an

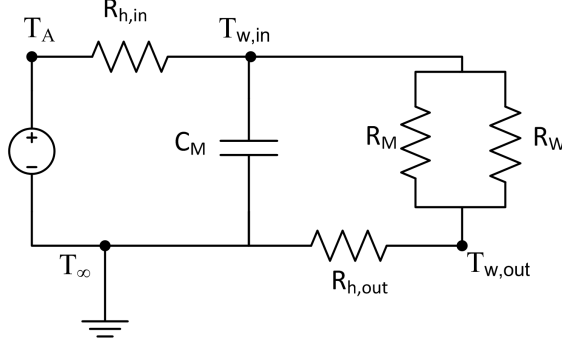


**Figure 10:** Electrical representation of the thermal heat transfer process for the SparkJet actuator.

equivalent capacitance. Here, only the thermal capacitance of the Macor is considered since the thermal capacitance of the tungsten electrodes is small due to their small volume. The thermal capacitance of Macor is given in Equation 23. With all of the circuit components defined, the wall temperatures can be solved using Equation 24.

$$R_M = \frac{L_M}{k_M A_M} \quad (19)$$

$$R_W = \frac{L_W}{k_W A_W} \quad (20)$$

$$R_{h,in} = \frac{1}{h_{in} A_{in}} \quad (21)$$

$$R_{h,out} = \frac{1}{h_{out} A_{out}} \quad (22)$$

$$C_M = \rho_M v_M C_p \quad (23)$$

$$\frac{T_A - T_{w,in}}{R_{h,in}} = C_M \frac{dT_{w,in}}{dt} + \frac{T_{w,in} - T_{\infty}}{R_{h,out} + \frac{1}{\frac{1}{R_M} + \frac{1}{R_W}}} \quad (24)$$

Another method for estimating SparkJet heat transfer is representing the differential form of the heat equation with finite difference equations. This method provides the most spatially and temporally accurate representation of the thermal effects involving the SparkJet cycle. However, this method can be more computationally time consuming. To maintain some level of simplicity the exact SparkJet cavity shape is not modeled but a single line through a side wall is analyzed. Due to the cylindrical shape of the SparkJet cavity and surrounding walls, the heat equation is analyzed in cylindrical coordinates as given in Equation 25 and the equation for thermal diffusivity,  $\alpha$ , is given in Equation 26.

$$\frac{\partial T}{\partial t} = \alpha \frac{\partial^2 T}{\partial x^2} = \frac{\alpha}{r} \frac{\partial}{\partial r} \left( r \frac{\partial T}{\partial r} \right) = \alpha \frac{\partial^2 T}{\partial r^2} + \frac{\alpha}{r} \frac{\partial T}{\partial r} \quad (25)$$

$$\alpha = \frac{k}{\rho C_v} \quad (26)$$



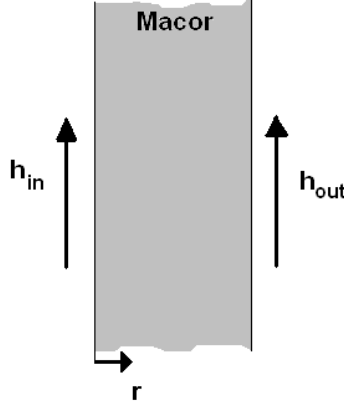


**Figure 11:** Sketch of the thermal heat transfer modeled using finite difference equations

For this work, discretization of the partial differential heat equation is accomplished by using explicit first-order, forward-difference discretization in time (Equation 27) and second-order, central-difference discretization in space (Equation 28). This discretization solves for the conductive heat transfer through the interior of the SparkJet walls at time step  $j$  and mesh point  $i$ . Separate equations are used to approximate the heat equation at the boundaries which involve the convective heat transfer as well.

$$\frac{\partial T}{\partial t} = \frac{T_i^{j+1} - T_i^j}{\Delta t} \quad (27)$$

$$\alpha \frac{\partial^2 T}{\partial r^2} + \frac{\alpha}{r} \frac{\partial T}{\partial r} \approx \alpha \frac{T_{i+1}^j - 2T_i^j + T_{i-1}^j}{\Delta r^2} + \frac{\alpha}{r_i} \frac{T_{i+1}^j - T_i^j}{\Delta r} \quad (28)$$

To solve for the internal mesh points, the above equations are used and combined in Equation 29.

$$\frac{T_i^{j+1} - T_i^j}{\Delta t} = \alpha \frac{T_{i+1}^j - 2T_i^j + T_{i-1}^j}{\Delta r^2} + \frac{\alpha}{r_i} \frac{T_{i+1}^j - T_i^j}{\Delta r} \quad (29)$$

At the boundaries, however, the effects of convection are taken into account. The internal boundary condition is given by Equation 30 and the external boundary condition is given by Equation 31.

$$hA(T_A^j - T_{i=1}^j) + kA \frac{T_{i=2}^j - T_{i=1}^j}{\Delta r} = \rho AC \frac{\Delta r}{2} \frac{T_{i=1}^{j+1} - T_{i=1}^j}{\Delta t} \quad (30)$$

$$hA(T_\infty^j - T_{i=M}^j) + kA \frac{T_{i=M}^j - T_{i=M-1}^j}{\Delta r} = \rho AC \frac{\Delta r}{2} \frac{T_{i=M}^{j+1} - T_{i=M}^j}{\Delta t} \quad (31)$$

The highly unsteady nature of the SparkJet thermal heat transfer requires very small time steps in this simulation. Based on numerical stability analysis, the maximum allowable time step for numerical stability is given in Equation 32. The mesh spacing,  $\Delta r$ , is given while the radius of each mesh point,  $r_i$ , is chosen to minimize  $\Delta t$  which corresponds to the radius of the SparkJet cavity.

$$\Delta t \leq \frac{1}{\alpha \Delta r \left( \frac{2}{\Delta r} + \frac{1}{r_i} \right)} \quad (32)$$

To compare the two thermal modeling methods for the SparkJet cycle, a notional temperature profile was applied to the internal wall. Equation 33 presents a negative exponential function of a magnitude of 2000 K to mimic the typical SparkJet cavity air temperature profile. For comparison, the internal wall temperature,  $T_{w,in}$ , was monitored using both methods. Figure 12 shows the temperature profile as a function of time.

$$T_n = (2000 - T_\infty) e^{-2000t} + T_\infty \quad (33)$$

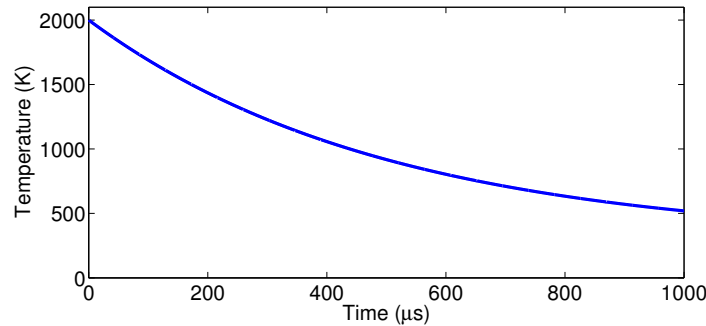
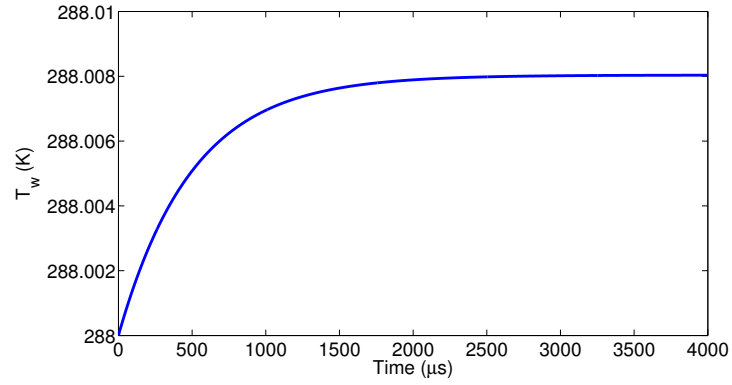


**Figure 12:** Notional temperature profile used to compare the combined thermal resistance and capacitance method and the discretization method.

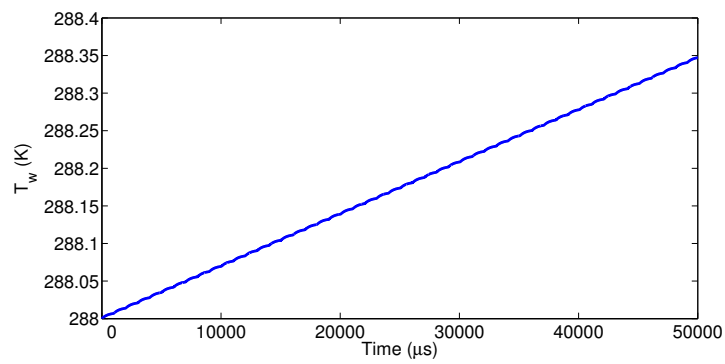
Figure 13 shows the wall temperature response to the notional temperature profile shown in Figure 12 over 1000  $\mu\text{s}$ . Initially, the wall temperature,  $T_{w,in}$ , rises quickly and then reaches an asymptotic value of 288.01 K. Surprisingly, the peak wall temperature is not significantly above the initial wall temperature of 288 K. Based on these results, an isothermal wall condition at 288 K may be sufficient for modeling the thermal heat transfer during a single SparkJet cycle. However, when considering multiple SparkJet cycles, recall that the wall temperature does not equal the ambient wall temperature at 1000  $\mu\text{s}$ . When modeling high-frequency actuation, the wall temperature rise can become more significant. Figure 14 shows the wall temperature response over 50 cycles at 1 kHz.

Figure 15 shows the spatial and temporal response of the cylindrical Macor walls to the notional temperature profile. At the wall surface, the temperature rises quickly and then more slowly decreases toward room temperature. Note, however, that the wall temperature only rises to a couple degrees above room temperature which compares well with the simplified thermal model. As time increases, the wall temperature decays but the interior temperature distribution rises as the thermal energy diffuses into the Macor. Also note that the thermal diffusion does not penetrate far into the Macor. In fact, the outer wall temperature rise is negligible and external thermal convection is irrelevant.

When considering the thermal effects over several SparkJet cycles, the internal wall temperature remains above the ambient temperature. Therefore, subsequent cycles will gradually raise the internal wall temperature such that prolonged cycles will result in a significant temperature rise as seen in Figure 16. Based on these results, a single SparkJet cycle can be



**Figure 13:** Wall temperature response to the notional temperature profile using the combined thermal capacitive and resistive model.



**Figure 14:** Wall temperature response to the notional temperature profile simulating 1 kHz actuation over 50 cycles.

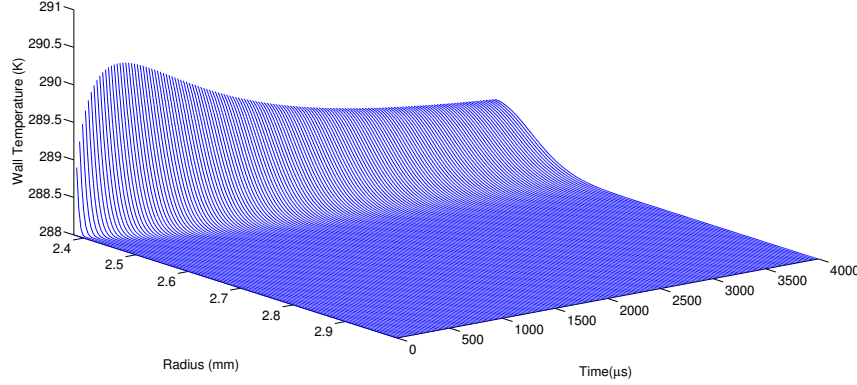


**Figure 15:** Time and space dependent thermal response of the Macor material to the notional temperature profile applied to the internal wall of the Macor during a single cycle.

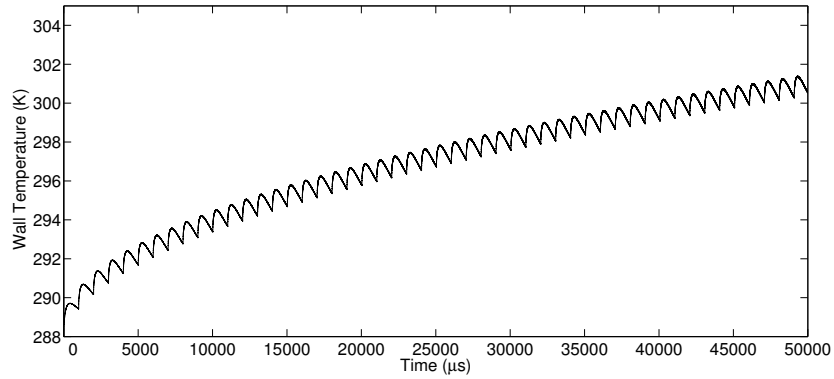
modeled with an isothermal wall boundary condition without sacrificing modeling fidelity. However, for high-frequency actuation, detailed thermal modeling is recommended.

Regardless of the method used to model heat transfer, defining the convective heat transfer coefficient remains a challenge. Inside the SparkJet cavity, unsteady pressure waves generate a forced convection condition while free convection exists outside the SparkJet walls. Methods for estimating the convective heat transfer coefficient are based on Reynolds number, Prandtl number and Nusselt number. However, these methods apply to convective heat transfer in relatively steady flows which is not the case inside the SparkJet cavity. As a result, a convective heat transfer coefficient of  $125 \text{ W/m}^2$  is used based on comparison to the CFD simulation referenced earlier[40].

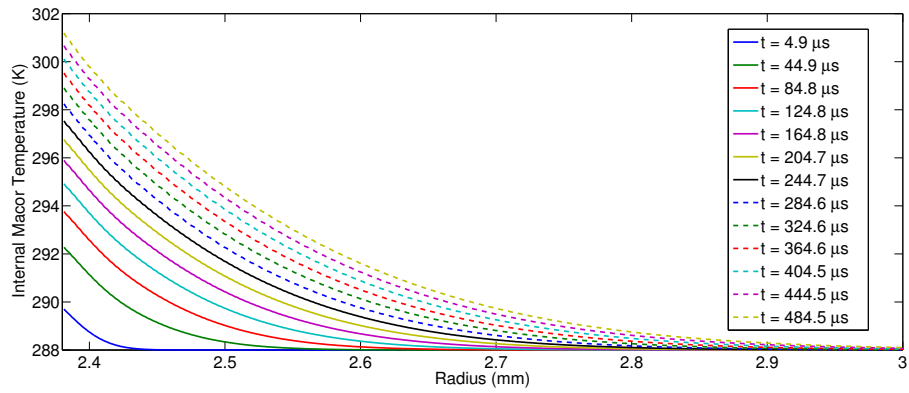
Considering the original thermal modeling goal of balancing fidelity with simplicity, the thermal model selected to be used with the fluid dynamic portion of the SparkJet 1-D model is the combined capacitive and resistive model. The following sections will show that the SparkJet momentum throughput reaches a steady-state value over tens of cycles. The previous plots showed that over 50 cycles, the wall temperature rises to only a few degrees above 288 K. While the finite difference modeling reveals some interesting thermal trends and phenomena, the wall temperature only increases 8 K above the ambient temperature. This temperature increase does not significantly affect the heat transfer; therefore, the simpler method best satisfies the modeling goal for this report.

## 2.3 Single Cycle Simulation

The system of equations described in the previous section were solved using the initial value problem solver in Matlab called ode45. The simulation requires multiple input parameters to properly represent an actual SparkJet cycle and the physical design. These parameters include ambient pressure, temperature, and density, cavity volume (excluding orifice volume),



(a) Wall temperature versus time.

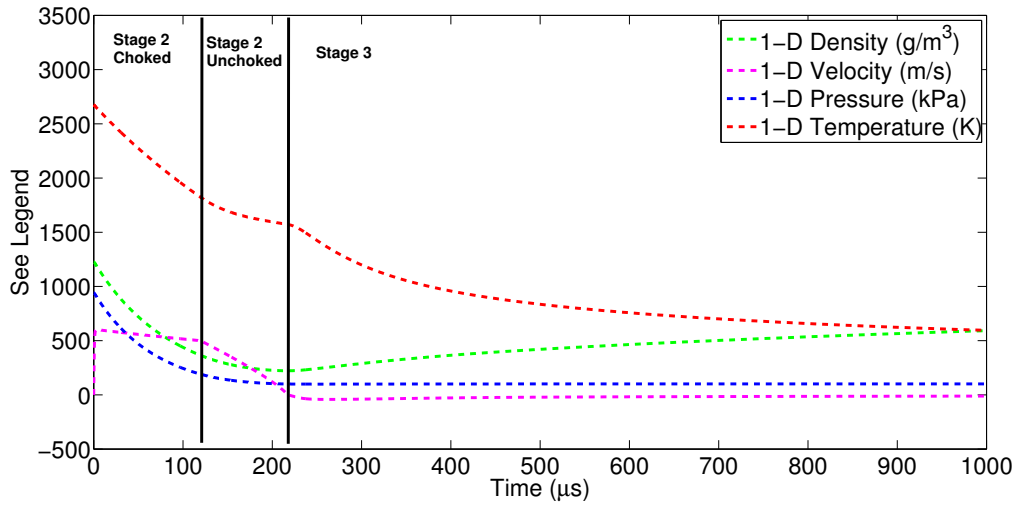


(b) Sample internal temperature distribution versus radius at various time steps.

**Figure 16:** Time and space dependent thermal response of the Macor material to the notional temperature profile applied at a frequency of 1 kHz over 50 cycles.

**Table 1:** Design parameters for numerical model.

Parameter	Value	Units
$P_\infty$	101325	Pa
$T_\infty$	288	K
$R$	287.15	J/kgK
$C_v$	716.85	J/kgK
$v$	42.4	mm <sup>3</sup>
$d_o$	1.0	mm
$H_o$	0.5	mm
$Q$	0.089	J

**Figure 17:** Simulation of the time-dependent variation in cavity pressure, temperature and density and the velocity through the orifice during early portion of the SparkJet cycle.

orifice diameter, orifice height, stored capacitor energy, specific heat capacity for a fixed volume of air, and the gas constant of air. When considering the thermal losses, thermal properties of the SparkJet cavity materials and electrodes are also required. To demonstrate this 1-D numerical model, Table 1 provides values for the required inputs. Figure 17 shows the time history of the cavity pressure, temperature and density as well as the orifice velocity during Stages 1 and 2 and the beginning of Stage 3. Figure 18 shows the full cycle ending when all cavity conditions have returned to ambient conditions.

To support the modeling assumptions related to viscosity; convective heat transfer; choked jet flow; and one-dimensionality of pressure, temperature, density, and velocity; the numerical modeling results are compared to the CFD simulation results previously shown in Figure 9. For the same energy deposition, cavity volume, orifice diameter, external flow conditions, and heat transfer mechanisms as the CFD simulation, the 1-D model and CFD results are compared in Figure 19. This figure shows that the overall comparison between the pressure, temperature, density, and velocity curves are quite good. The largest disparities occur at

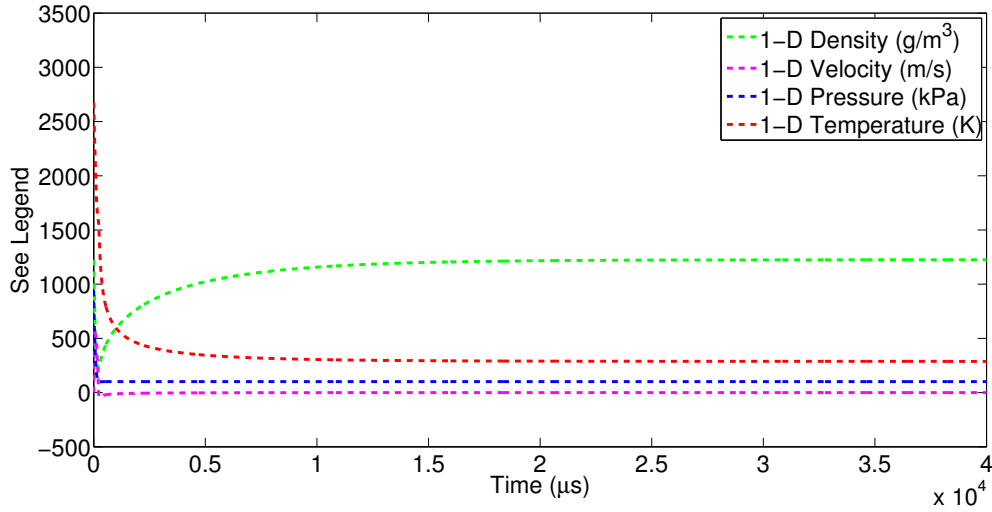


**Figure 18:** Simulation of the time-dependent variation in cavity pressure, temperature, and density and the velocity through the orifice for the entire SparkJet cycle. Note that cavity temperature, pressure, and density have returned to original ambient conditions as given in Table 1.

the beginning of the SparkJet cycle and are likely due to the highly unsteady flow present in the cavity and orifice as the jet formation begins. The unsteadiness is also responsible for the oscillations in the CFD velocity curve. However, as the cycle continues, the two modeling solutions merge. This comparison does not necessarily prove the assumptions but certainly supports them. With this level of confidence in the initial 1-D model development, the model is expanded to high-frequency actuation.

## 2.4 Simulating High-Frequency Actuation

As discussed in Section 1, most AFC techniques require actuation at frequencies matching or at a harmonic of natural instability in the flow. This model was modified to study the effect of high-frequency actuation on SparkJet performance. Figure 20 shows the variation in cavity pressure, temperature, and density and the velocity through the orifice when the SparkJet is actuated under the same conditions listed in Table 1 at 100 Hz.

Figure 20 demonstrates the effect of high-frequency actuation on SparkJet performance. Even at 100 Hz, the second cycle encroaches on the end of Stage 3 of the first cycle such that the peak temperature for the second cycle is slightly higher than that of the first cycle. This is indicative of the effect of a very slow, unforced refresh cycle. At relatively low frequencies, effects of an unfinished cycle can already be seen on the following cycle. Because momentum is an important performance parameter for AFC devices, Figure 21(a) shows that the effect is visible but not significant for actuation at 100 Hz. However, as frequency is increased, this effect is even more evident as shown in Figure 21(b) when the SparkJet is actuated at 1 kHz and 5 kHz.

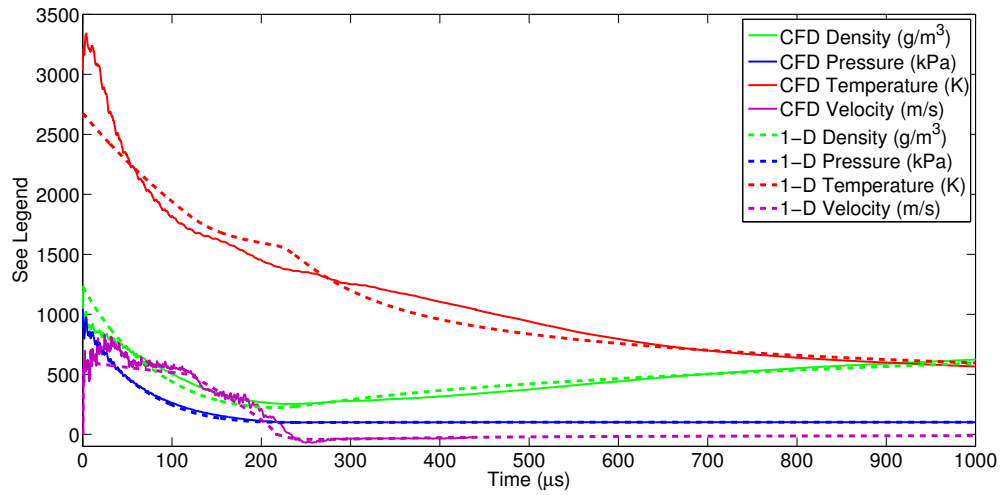


**Figure 19:** Comparison of the cavity pressure, temperature, and density and orifice velocity versus time based on the CFD simulations and the simplified numerical model.

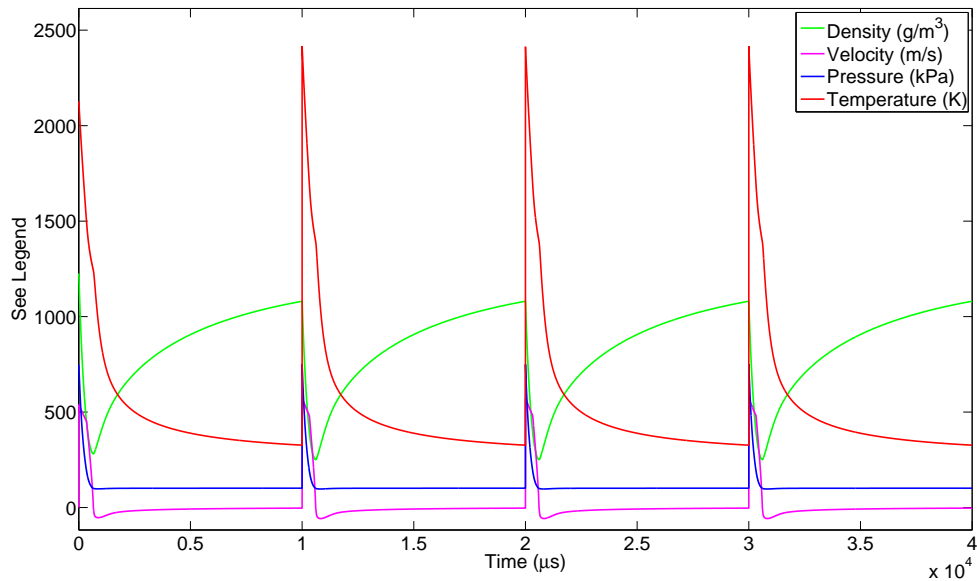
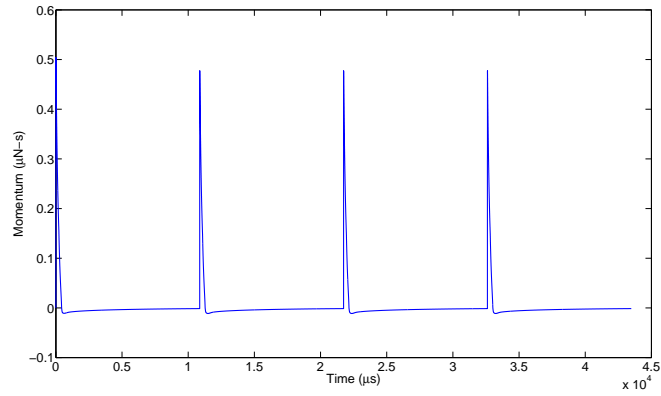
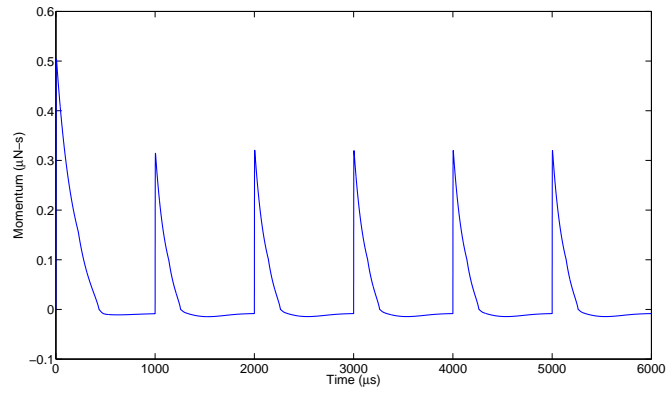


**Figure 20:** Simulation of the time-dependent variation in cavity pressure, temperature, and density and the velocity through the orifice for four SparkJet cycles at 100 Hz.

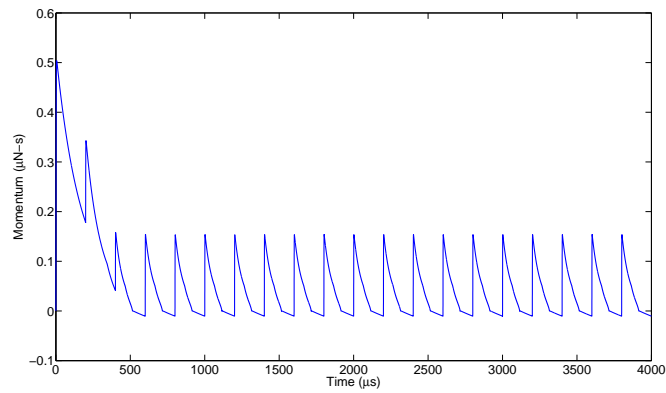




(a) 100 Hz.



(b) 1000 Hz.



(c) 5000 Hz.

**Figure 21:** Simulation of the momentum through the SparkJet orifice as a function of time when operated at 100, 1000, and 5000 Hz.

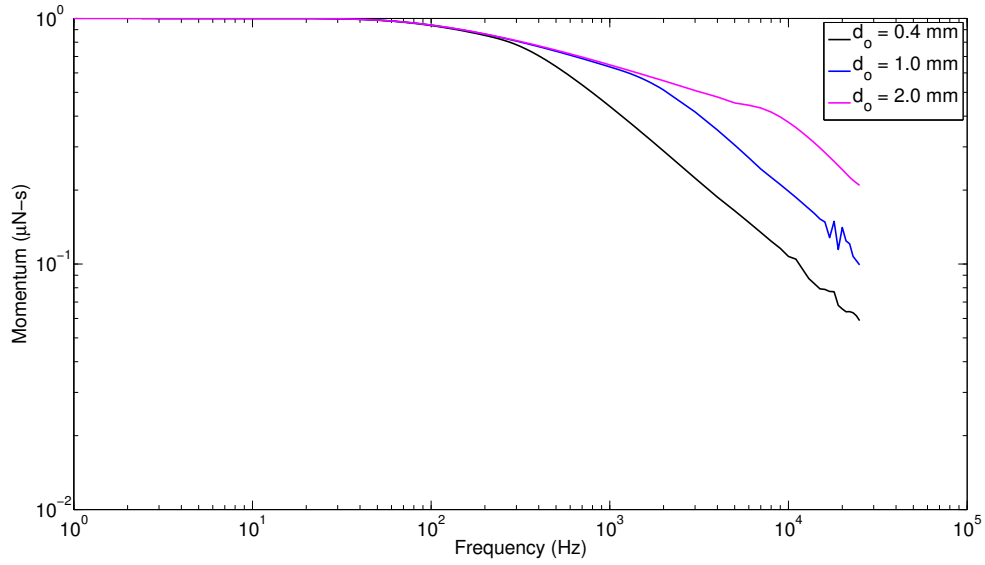


**Figure 22:** Magnitude plot of the steady-state momentum throughput from the SparkJet actuator operated from 1 Hz to 10 kHz for orifice diameters of 0.4, 1.0, and 2.0 mm.

When the simulation is run over a range of frequencies from 1 Hz to 20 kHz, the steady state momentum can be plotted as a function of frequency as shown in Figure 22. The steady state momentum output remains constant until approximately 100 Hz and continues to decrease as frequency increases. This can depend, of course, on the design parameters such as orifice diameter, cavity volume, and  $Q_C/E$ , primarily. Figure 22 shows that increasing the orifice diameter or decreasing the cavity volume allows for higher momentum throughput as frequency increases. High-frequency performance is independent of  $Q_C$ . At frequencies above 10 kHz, the momentum curves become oscillatory. The source of these variations is because at very high frequencies, the steady-state operation is actually bimodal and the peak pressure achieved during Stage 1 alternates between two values. At the minimum of these two values, the energy deposition is so low that Stages 2 and 3 are relatively short compared to the previous cycle and the cavity density is allowed to rise to a higher value than the previous cycle. With a higher cavity density, the energy deposition is stronger which leads to a relatively long Stage 2 and 3 and this cycle repeats indefinitely. Taking each of these trends into consideration, the high-frequency performance is improved by design parameter changes that essentially shorten the duration of the complete SparkJet cycle.

### 3 Experimental Details and Data Acquisition

While comparison to CFD supports assumptions related to fluid dynamics, the assumptions for energy transfer modeling during Stage 1 lack validation. Therefore, experimental measurements were made to understand the plasma-physics and support Stage 1 modeling. The SparkJet actuator has been characterized with simultaneous internal cavity pressure measurements and arc power measurements to understand SparkJet operation and efficiency as

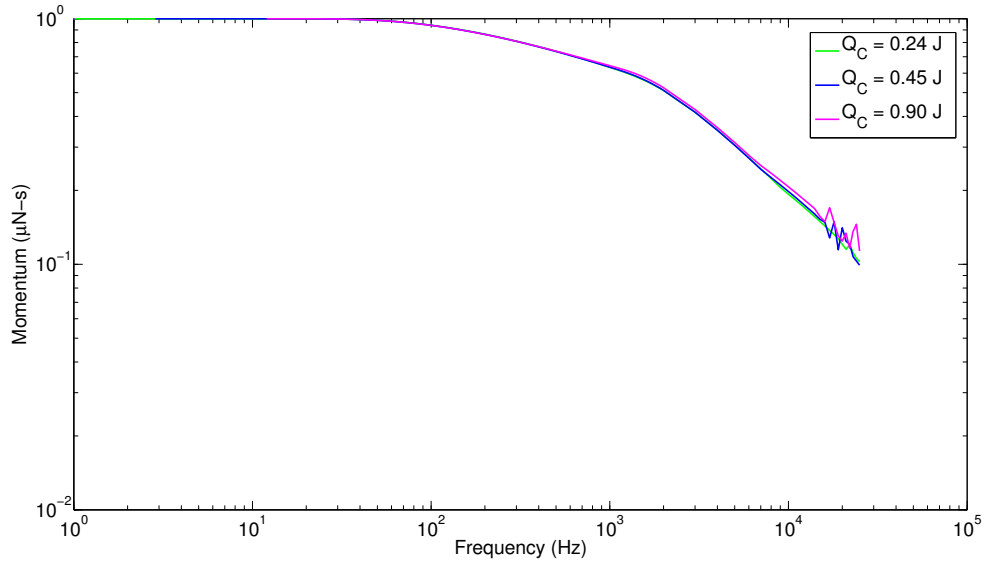


**Figure 23:** Magnitude plot of the steady-state momentum throughput from the SparkJet actuator operated from 1 Hz to 10 kHz for energy deposition values of 0.24, 0.45, and 0.90 J.

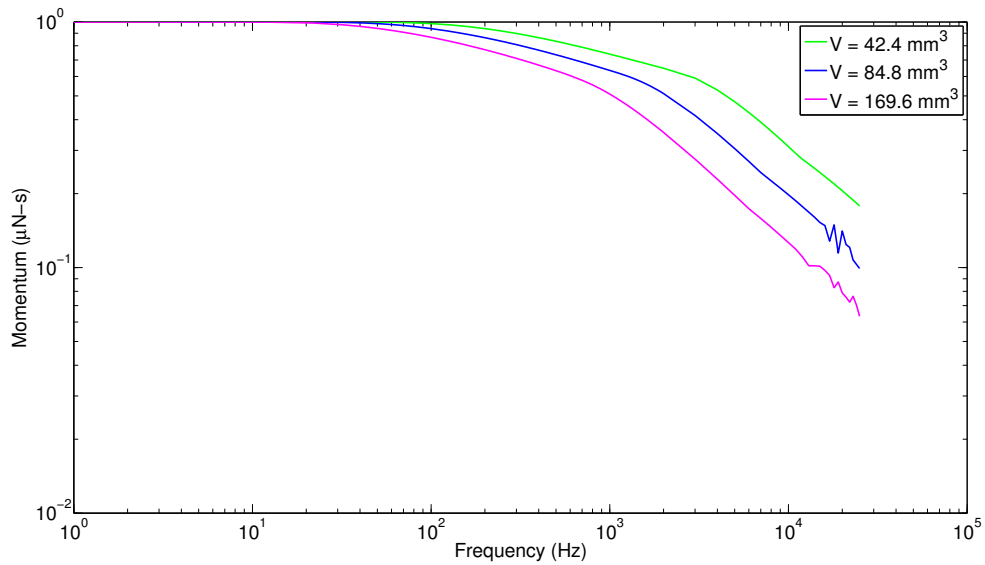


**Figure 24:** Magnitude plot of the steady-state momentum throughput from the SparkJet actuator operated from 1 Hz to 10 kHz for cavity volumes of 42.4, 84.8, and 169.6 mm<sup>3</sup>.

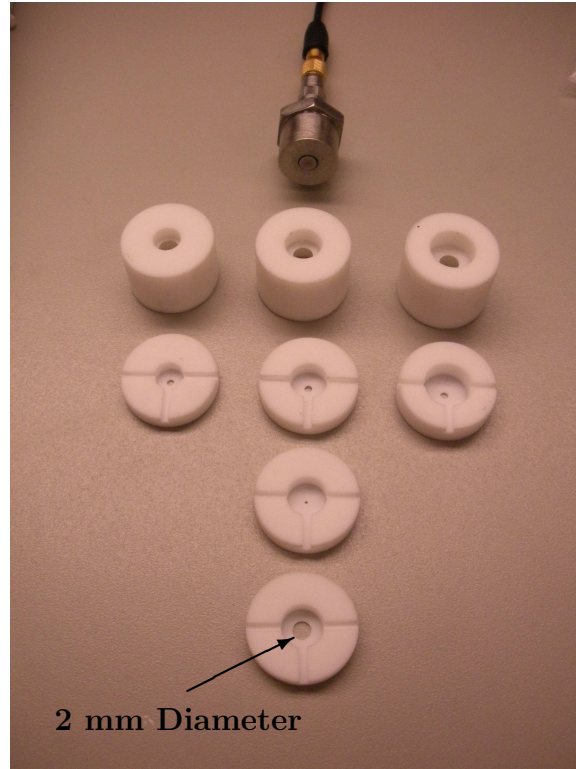


**Figure 25:** Photograph of the SparkJet cavities and lids used to characterize the effect of cavity volume and orifice diameter on SparkJet cavity pressure rise and performance.

a function of physical and electrical design parameters. The details for this experimental testing have been described in detail in Reference [43].

Internal cavity pressure measurements were completed using a high-frequency response, dynamic pressure transducer. The arc power drawn was estimated using the product of current and voltage measurements. These measurements lead to an experimental demonstration of SparkJet performance and estimation of the operating efficiency. This new knowledge supported the need to modify the 1-D Stage 1 modeling.

### 3.1 SparkJet Actuator

To characterize the SparkJet operation, several design parameters were varied to analyze the effect on the peak pressure rise in the cavity. These parameters include the orifice diameter, cavity volume, capacitance and voltage across the electrodes, and electrode gap. Figure 25 shows a photograph of the variety of Macor SparkJet bases and lids corresponding to variations in cavity volume (42.4, 84.8 and 169.6 mm<sup>3</sup>) and orifice diameter (0.4, 1.0 and 2.0 mm). Also in this image, the metal housing that was inserted into the bottom of the SparkJet base with the pressure sensor installed (small circle in the center of the metal face) and the connection to the sensor BNC cable are visible. Details on the sensor and installation are also discussed in Reference [43].

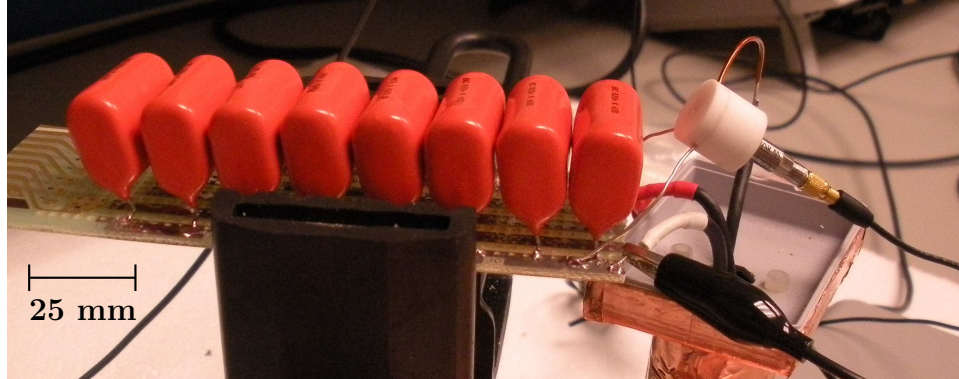


**Figure 26:** Photograph of the SparkJet setup with eight  $0.88 \mu\text{F}$  capacitors across the electrodes. Note the proximity of the capacitor connections to the SparkJet itself to allow for short wires and prevent losses that would exist with long wires.

The remaining design parameters were functions of the electrodes or the electronics. The electrode spacing was controlled during the assembly process and measured using a digital micrometer. The voltage across the electrodes was controlled by an external power supply but was typically set near 600 V for maximum output energy. The capacitance across the electrodes was controlled by adding or subtracting individual capacitors from a bank of capacitors as seen in Figure 26. Also note in this photograph that the wires from the capacitor bank to the SparkJet are only a few inches long. The short wires help minimize power losses that would exist with long wires.

In addition to a single orifice design, the orifice array SparkJet design was used for the microschlieren image acquisition. The orifice array design, intended for direct comparison with microjet arrays that were implemented in previous wind tunnel tests[11], consists of a cavity, removable electrode holder, electrodes and the orifice array as shown in the schematic in Figure 27(a). The trigger and sustain electrodes are of the same materials described for the single orifice design. The decision to design the array with a single cavity rather than one cavity per orifice stemmed from the desire to reduce the number of power supplies and electronic components. In addition, a single cavity and arc discharge ensures that the flow through each orifice is in phase. The cavity is formed from a square piece of Macor with a hole drilled defining the outer diameter of the cavity and two glass disks forming the sides of the cavity, while also providing optical access to the cavity. The cavity volume is  $363 \text{ mm}^3$  based on a diameter of 8.89 mm and depth of 5.84 mm. The SparkJet array cavity volume was chosen such that it scaled approximately with the number of orifices based on the  $84.8 \text{ mm}^3$  single orifice SparkJet design. A second hole was drilled in the Macor to insert the holder containing the electrodes. The orifice array (Figure 27(c)) is made up of four holes that are 0.4 mm in diameter and 0.5 mm in depth. The capacitance across the sustain electrodes remained constant at  $13 \mu\text{F}$  and the voltage across the electrodes is 600 V resulting in  $Q_C=25.05 \text{ J}$ .

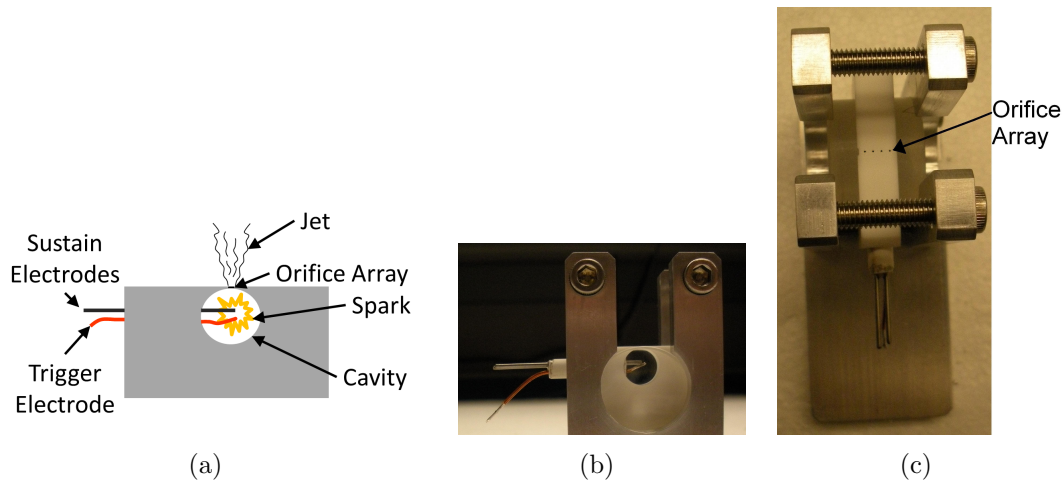


**Figure 27:** SparkJet Array (a) schematic and photograph of the (b) side view and (c) top view.

### 3.2 SparkJet Power Supplies

As the SparkJet operation was better understood over the duration of this grant, the SparkJet electronics were modified to meet high-frequency demands and/or to improve SparkJet performance. Two circuit designs were used to operate the SparkJet actuator involving an external trigger and pseudo-series trigger. The primary circuit used to generate the experimental results is shown in Figure 28 and is based on an externally triggered arc discharge concept rated to 600 V. For the remainder of this report, this circuit is referred to as 600ET.

The circuit shown in Figure 29 corresponds to the pseudo-series trigger SparkJet power supply with a maximum capacitor voltage of 600 V and is identified as 600PST. Transition to this circuit was motivated by actuator reliability concerns from FSU/AAPL. With the original intention of improving SparkJet reliability, results discussed in Section 4 will show that the 600PST circuit had additional performance benefits beyond improved actuator reliability.

Basic operation of both of the power supplies are very similar. The SparkJet operates on a triggered capacitive arc discharge; therefore, each SparkJet power supply includes a means of triggering the discharge (trigger circuit) and a bank of capacitors parallel to the SparkJet anode and cathode which sustains the trigger spark (sustain circuit). The sustain and trigger circuits are identified in Figures 28 and 29 by a red dash-dot rectangle surrounding the sustain circuit and a blue dashed rectangle surrounding the trigger circuit. An external DC power supply is used to charge the capacitor bank to a set voltage, and the output current limit of the power supply determines the charging rate per capacitance. Therefore, one determining factor in the frequency limit of the SparkJet is due to the DC power supply current limit.

Separate from the sustain circuit is the trigger circuit. A capacitor is charged by a separate DC power supply, and the charging rate is regulated by a resistor. If the trigger spark locally reduces the breakdown voltage below the electrode voltage, Stage 1 begins as the main

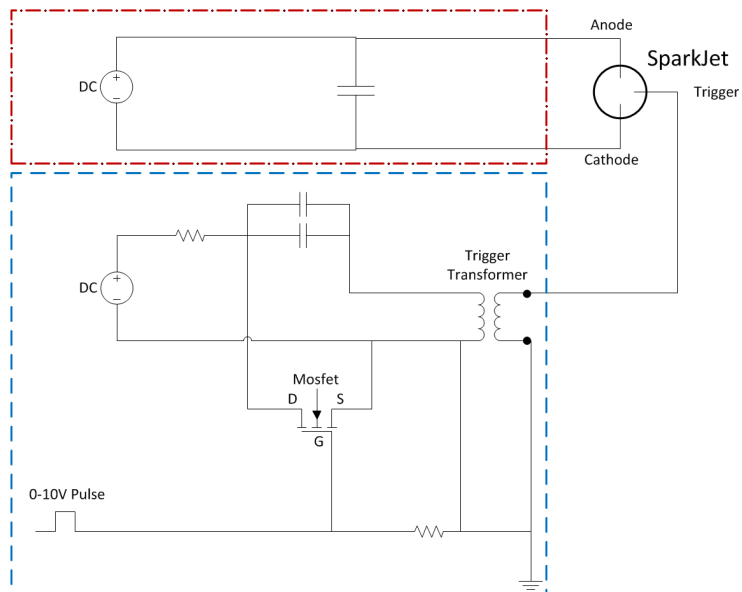


**Figure 28:** Circuit diagram of the 600 V external trigger SparkJet power supply.

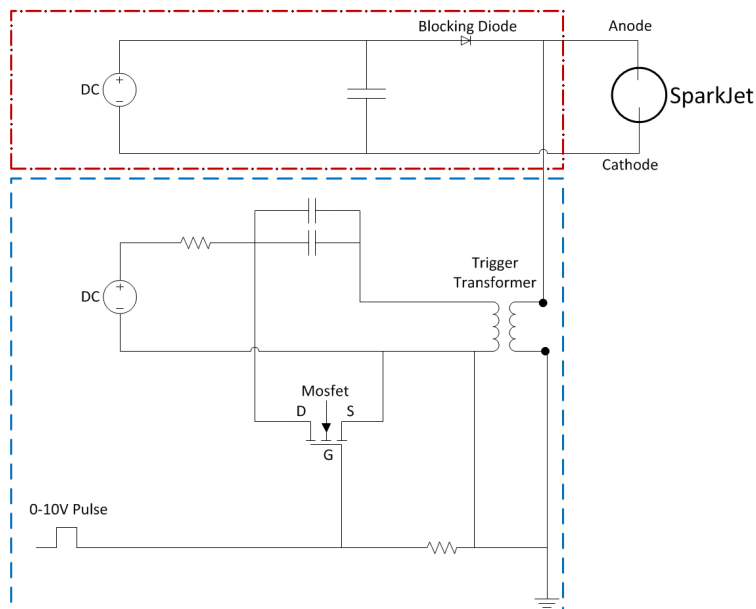


**Figure 29:** Circuit diagram of the 600 V pseudo-series trigger SparkJet power supply.

capacitor bank discharges across the anode and cathode. In the case of the pseudo-series circuit, the high-voltage transformer output is connected to the anode but high-voltage, high-current blocking diodes prevent the high voltage from interacting with the capacitor bank portion of the circuit. Further detail explaining the difference between the external and pseudo-series triggers are available in Reference [43].

Utilizing the pseudo-series trigger circuit offers both electrical and physical operating performance benefits. With the pseudo-series trigger circuit, the electrode configuration reduces to two electrodes while maintaining the ability to synchronize with data acquisition equipment. In this design, the trigger spark occurs between the anode and cathode thus reducing the breakdown voltage of the entire gap rather than a portion of the gap as with the external trigger circuit. Triggering across the entire gap increases reliability in producing an arc breakdown and, thus, operating the SparkJet actuator. Further benefits are also apparent when measuring the cavity pressure which is demonstrated in Section 4.

### 3.3 Data Acquisition

The primary instrument used to collect data is an Agilent AT-DSO5014A - 100MHz 4CH portable oscilloscope which monitors the low-voltage pulse, the voltage across the electrodes, the pressure sensor output and, for the 600PST circuit, the current through the electrodes at a sampling frequency of 250 MHz. Monitoring the low-voltage pulse is simply through a BNC cable from the pulse generator to the oscilloscope. A BK Precision Model PR2000 200 MHz Oscilloscope High Voltage Probe with x100 attenuation and rated to 2 kV was used to measure the voltage across the capacitors on the 600ET circuit. To monitor the trigger voltage, which typically exceeds 5 kV, a Tektronics P6015A 1000x high voltage passive test probe rated to 20 kV DC is used. Due to the design of the 600PST circuit, this probe also measured the voltage across the capacitors on the 600PST circuit. The pressure sensor output passes through a PCB Model 482C Signal Conditioner designed for PCB pressure sensors before reaching the oscilloscope. Current measurements were made using a Pearson Model 110 monitor. This instrument was added to the data acquisition process when the pseudo-series trigger research began because the voltage across the anode and cathode exceeded the voltage rating of the BK Precision voltage probe during triggering. The power drawn by the arc is simply the product of current and voltage. Separate from the oscilloscope measurements, the capacitance parallel to the electrodes is measured prior to operating the SparkJet using a Fluke Model 179 True RMS Multimeter.

### 3.4 Cavity Pressure Sensor

The high-frequency pressure data was obtained using a PCB 105C12 dynamic pressure sensor (Figure 32) installed in the bottom of the SparkJet cavity, opposite the orifice. The sensor design includes threads for installation and a brass ring to provide a pressure seal. This transducer has a response time of less than 2  $\mu$ s, resolution of 20 mpsi, and resonant frequency greater than 250 kHz. The force from the sensor threads due to the recommended torque (1.69 Nm) exceeds the strength of the Macor. Therefore, a stainless steel component was inserted into the Macor as shown in Figure 31 in order to support the sensor installation. The



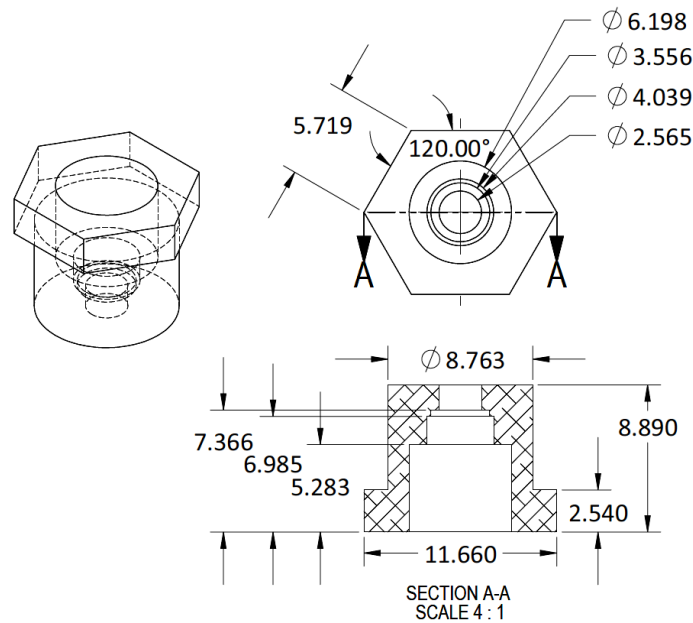


**Figure 30:** Drawing of the metal insert used to mate the SparkJet Macor housing to the PCB pressure transducer.

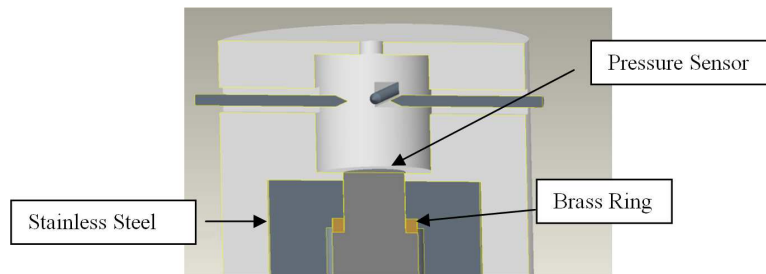


**Figure 31:** Cross section view of the SparkJet cavity, electrodes (configured for an external trigger) and installed pressure sensor.

stainless steel component was secured to the Macor using 5-minute epoxy. A detailed drawing of the metal insert is shown in Figure 30. The Macor and stainless steel are dimensioned such that the face of the pressure sensor is flush with the bottom of the cavity leaving a thin Macor wall between the cavity and the metal insert. The PCB 105C12 pressure sensor was chosen for its small size (2.5 mm sensing diameter), fast response time, and high flash temperature tolerance (1922 K). An additional benefit of using this sensor is the low sensitivity to Electromagnetic Interference (EMI) because the sensor is connected to the PCB Model 482C signal conditioner via a shielded BNC cable.

The PCB sensor sensing technology includes a preloaded quartz crystal surrounded by a stainless steel housing. The loading on the quartz determines the output signal. Ideally, only pressure changes at the sensor face affect the output signal. However, thermal loads can also affect the output signal due to the small size of the sensor and the proximity to the



**Figure 32:** Photograph of the uninstalled PCB 105C12 dynamic pressure sensor.

hot spark. To reduce the effects of the thermal shock associated with the initial blast wave, the exposed face of the sensor was coated with black Room Temperature Vulcanized (RTV) sealant.

### 3.5 Signal Post-Processing

The uncertainty for the single-ended voltage, differential voltage, current, and pressure measurements are  $\pm 10$  V,  $\pm 10$  V,  $\pm 10$  A and  $\pm 50$  kPa, respectively, based on the steady state oscillations before each arc discharge. Through ensemble averaging, these uncertainties were reduced to  $\pm 5$  V,  $\pm 5$  V  $\pm 3$  A, and  $\pm 25$  kPa, respectively. Uncertainty associated with the capacitance measurement before each discharge was  $0.01 \mu\text{F}$ .

For each SparkJet design, the voltage, current and pressure were acquired five times such that each signal could be ensemble averaged to reduce measurement uncertainty. For the voltage and current signals, this level of post-processing was sufficient to obtain a reliable signal with 50% reduction in the signal to noise ratio. The unsteadiness observed in the pressure data is very repeatable; however, for efficiency analysis, unsteadiness obscures the volume-averaged peak pressure measurement. Therefore, the pressure output was low-pass filtered above 60 kHz.

The cavity pressure data acquired are very unsteady beginning with the very high pressure associated with the initial blast wave and subsequent reflected waves within the cavity. Following each pressure wave, the pressure signal drops to a very low value and can even be negative. Part of the oscillations are due to mechanical resonance of the sensor at frequencies greater than or equal to 250 kHz (actually observed near 310-320 kHz) according to the PCB manual. Natural pressure wave reflections occur at lower frequencies ( $\approx 100$ -250 kHz) depending primarily on cavity dimensions. Because the purpose of this efficiency analysis is to improve modeling accuracy in a 1-D model utilizing a volume-averaged cavity pressure, there is a need to apply a low-pass filter to the high-frequency oscillations. The PCB output is linear up to one fifth the resonance frequency ( $\approx 310$  kHz) based on an FFT (Fast Fourier Transform) analysis of the pressure signals. Therefore, each pressure signal was decomposed into frequency components and only components less than 60 kHz were used to provide a volume-averaged peak pressure estimate. Equations 34 through 36 are used to reconstruct the pressure signal over a specified frequency range using Equation 37 where  $\omega_0 = 2\pi f_{\text{sampling}}$

( $f_{\text{sampling}} = 250$  MHz). The maximum value of the resulting filtered pressure signal is used to determine the pressure-based efficiency.

$$a_0 = \frac{1}{T} \sum_{t=0}^T P(t) dt \quad (34)$$

$$a_n = \frac{2}{T} \sum_{t=0}^T P(t) \cos(n\omega_0 t) dt \quad (35)$$

$$b_n = \frac{2}{T} \sum_{t=0}^T P(t) \sin(n\omega_0 t) dt \quad (36)$$

$$P(t) = a_0 + \sum_{n=1}^{n_{\text{max}}} a_n \cos(n\omega_0 t) + b_n \sin(n\omega_0 t) \quad (37)$$

Figure 33 shows several comparative plots demonstrating the effect of filtering on the pressure signals. Specifically, Figure 33(a) shows the effect of filtering the ensemble averaged pressure signal. Using Equation 44 (which will be derived in Section 4.2), the energy required to raise the cavity pressure to the maximum value is compared to the stored capacitor energy to provide an estimation of the pressure-based efficiency.

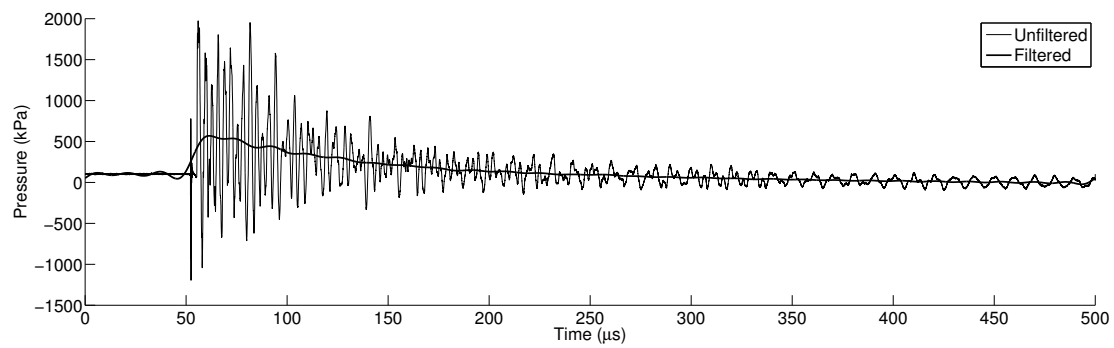
Figure 33(b) demonstrates the effect of applying the filtering technique described above for a cavity volume of  $169.6 \text{ mm}^3$ , orifice diameter of 1 mm, electrode gap of 1.75 mm, and capacitance of  $5.08 \text{ } \mu\text{F}$ . The filtered and unfiltered FFT results track almost exactly up to the cutoff frequency at 60 kHz. Beyond the cutoff frequency, the FFT of the filtered signal is nearly zero. This plot comparison clearly demonstrates the effectiveness of the low-pass filter.

## 4 Pressure-Based Results and Analysis

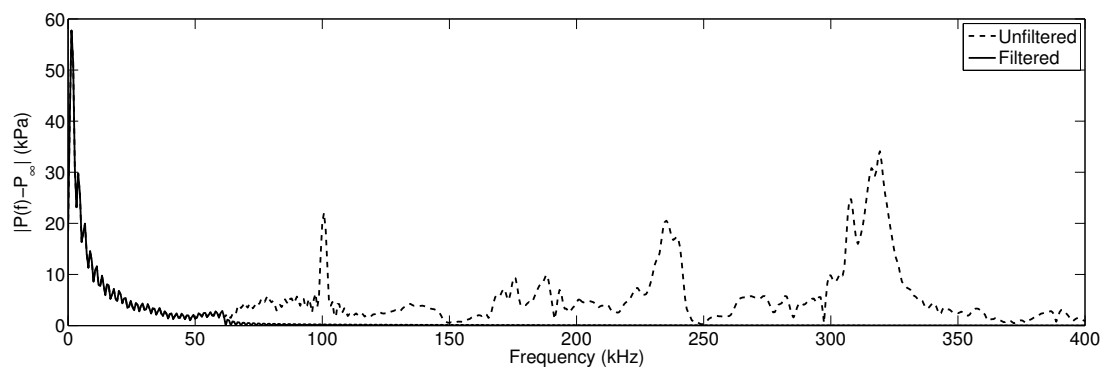
Using the experimental setup described in Section 3, the SparkJet performance based on cavity pressure, electrode voltage and arc current is studied. This section focuses on the pressure-based results with analysis and discussion. First, a general understanding of the SparkJet cavity pressure as a function of several design parameters is considered. Second, the peak pressure is converted to an efficiency metric to understand SparkJet performance as a function of a variety of parameters.

### 4.1 Basic Operation

Before presenting the bulk of the experimental results, a look at a single SparkJet data acquisition cycle is considered here for each experimental setup. Figure 34 shows a typical output from the 600ET circuit. The black, low-voltage line shows the input pulse and the blue line shows the voltage across the electrodes just before and after Stage 1. The dashed,



(a)



(b)

**Figure 33:** Pressure and FFT data demonstrating the effect of low-pass filtering on the SparkJet internal cavity pressure measurements.

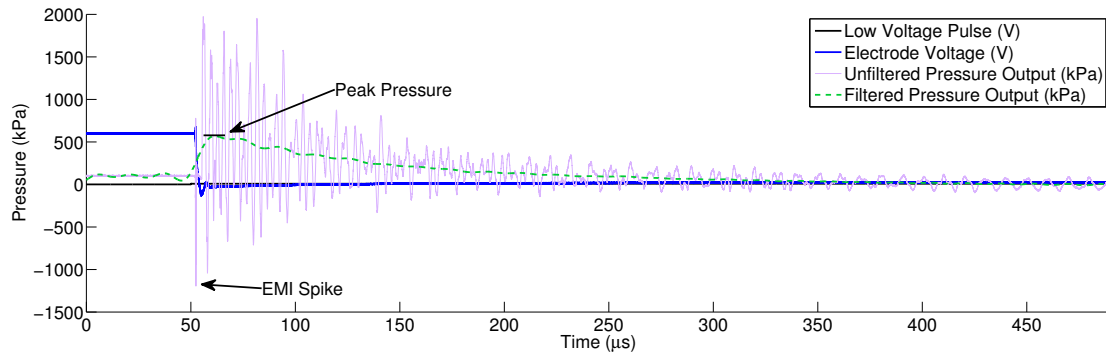


**Figure 34:** Example of data acquisition output for the 600ET setup and SparkJet cavity volume of  $169.6 \text{ mm}^3$ , orifice diameter of  $1.0 \text{ mm}$  and capacitance of  $5.08 \text{ } \mu\text{F}$ .

light purple line shows the raw pressure transducer output, and the dark green line shows the filtered pressure output to attenuate the nonlinear pressure response above  $60 \text{ kHz}$ . Analysis of each data set involves averaging the voltage over  $0.4 \text{ } \mu\text{s}$  (100 samples) to determine the applied voltage across the actuators and, therefore,  $Q_C$ . The raw pressure transducer output is initially affected by EMI from the trigger spark as indicated by the EMI spike, but the signal conditioner prevents the output signal from continuing to be contaminated. While the EMI spike is not related to pressure, it indicates when the trigger spark was initiated. After the EMI spike, the first significant pressure rise provides the time of arrival for the first blast wave from the arc, typically  $2\text{-}5 \text{ } \mu\text{s}$  after the EMI spike. Beyond the first pressure rise, the signal represents the pressure due to the arc acting on the face of the PCB sensor. The resulting filtered signal is shown in Figure 34 to demonstrate the effect of filtering. The filtered pressure transducer output is the source of the maximum pressure used in subsequent plots and analysis.

Figure 35 shows the typical output for the 600PST circuit, which is a similar plot to Figure 34 except for two differences. First, the voltage across the electrodes is approximately  $600 \text{ V}$ , but there is a spike in the voltage which represents the trigger voltage now that the trigger and capacitor voltages coincide with each other. In this particular plot, the trigger voltage saturates the oscilloscope measurement range in order to maximize measurement resolution of the voltage drop during Stage 1. Second, this plot includes the current across the electrode gap as shown in orange. Figure 36 shows a zoomed in section of Figure 35 focusing on the output signals during Stage 1. Here, the initial rise of the low-voltage pulse is more visible and shows that there is approximately  $0.2 \text{ } \mu\text{s}$  delay between the start of the low voltage pulse and the rise of the trigger voltage. Also, there is a delay of about  $0.5 \text{ } \mu\text{s}$  from when the trigger voltage rise begins and the high-power arc discharge. Therefore, a total delay of approximately  $0.7 \text{ } \mu\text{s}$  exists between the low-voltage input to the beginning of the arc discharge.

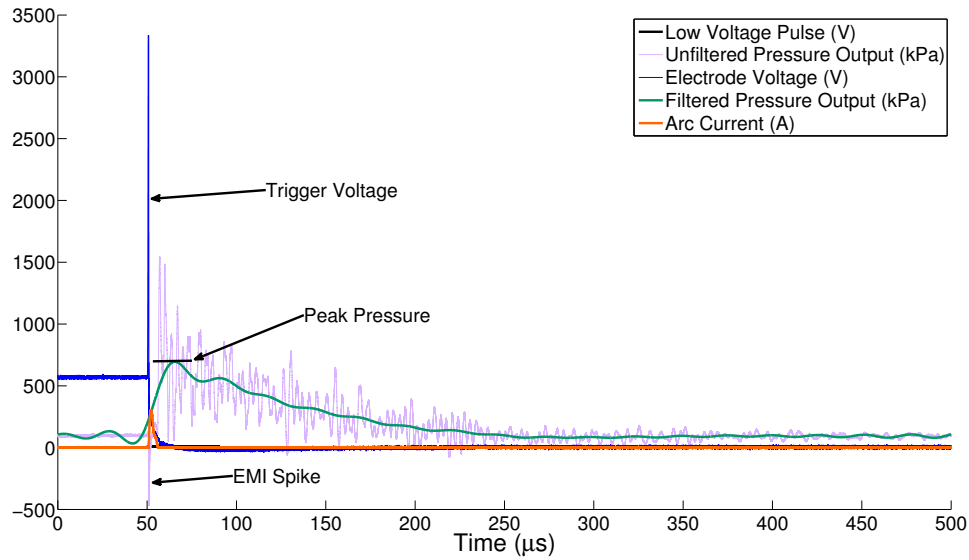


**Figure 35:** Example of data acquisition output for the 600PST setup and SparkJet cavity volume of  $84.8 \text{ mm}^3$ , orifice diameter of  $1.0 \text{ mm}$  and capacitance of  $1.67 \text{ }\mu\text{F}$ .

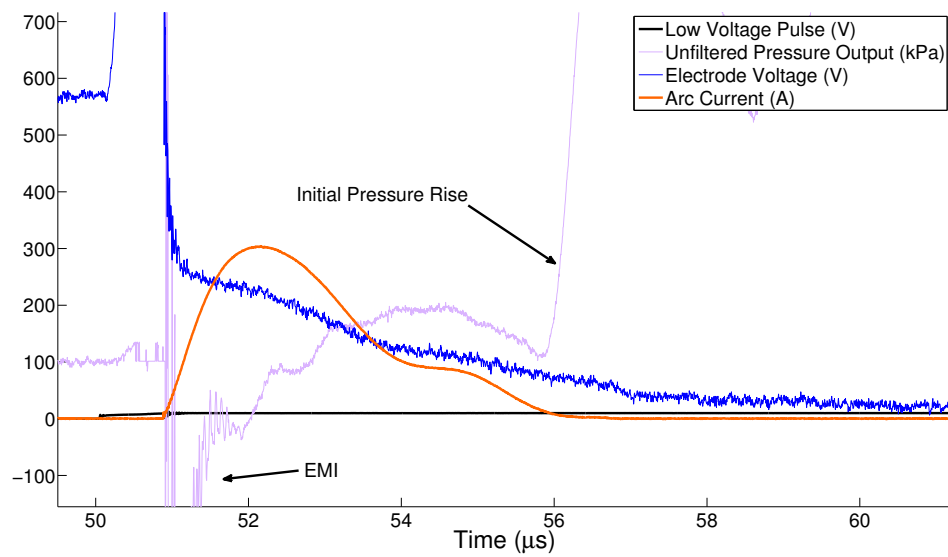


**Figure 36:** Data acquisition output for the 600PST setup zoomed in to show the current and voltage outputs in more detail.

## 4.2 Efficiency

The arc discharge and resultant Joule heating are complex processes which are dependent on circuit design and localization of the arc discharge within the cavity. The purpose of this efficiency analysis is to provide an understanding of the SparkJet efficiency, the source of inefficiencies and methods to improve efficiency starting with a calorically and electrically ideal system. In addition, the results of this efficiency analysis support modifications to Stage 1 modeling.

Efficiency is evaluated by determining the energy associated with the multiple processes involved in Stage 1. The equations used to model Stage 1 assume ideal energy transfer from the capacitors to the arc to raising the temperature and pressure of the cavity air. However, there are several electrical and physical effects that reduce the energy output by the SparkJet actuator. During the conversion of stored capacitor energy to the arc, there are energy losses outside those described by Narayanaswamy [44] which include resistance in the wires leading to the electrode tips, an increasing  $C_v$  as the cavity temperature increases, and localized, rather than distributed, energy deposition and heating. These phenomena result in an efficiency,  $\eta$ , less than 1.

The total energy released due to the power drawn by the arc is estimated using Equation 38 where  $V$  and  $I$  are directly measured. The efficiency related to converting stored capacitor energy to arc power is given in Equation 39. Efficiency losses here are related to parasitic resistance and inductance in wires and other circuit components which depend on circuit design. The efficiency of transferring capacitive energy,  $Q_C$ , to the energy drawn by the arc,  $Q_A$ , is calculated using Equation 39.

$$Q_A = \int V(t)I(t)dt \quad (38)$$

$$\eta_A = Q_A/Q_C \quad (39)$$

Knowing the energy deposited as a function of time, the corresponding cavity air temperature rise due to Joule heating is estimated using Equation 6 at each time step. The heat produced transfers from the arc column to the surrounding air or materials. Some heat is inevitably lost to the electrodes because the heat is released at the electrode tips [45]. The remaining heat, however, is transferred to the cavity air. The non-instantaneous energy deposition calculation assumes the energy is added to the entire cavity volume to raise the cavity temperature. This assumption does not take into account the highly spatial effects associated with the spark discharge but provides some insight into the efficiency losses.

In an attempt to incorporate the effects of the high cavity temperatures,  $C_v$  is estimated as a function of cavity air temperature resulting in a temperature dependent  $C_v$  and a thermally perfect gas assumption. Once the new cavity temperature is determined, the value of  $C_v$  is adjusted according to the simple harmonic oscillator model, Equation 40, and assuming a thermally perfect gas [46]. Here,  $\gamma_p$  and  $C_{v,p}$  correspond to a calorically perfect gas and  $\theta$  is the molecular vibrational energy constant equal to 3055.6 K. At the conclusion of the energy

deposition, the final cavity temperature is used in Equation 41 to determine the energy required to raise the cavity temperature assuming the idealized calorically perfect conditions. The additional efficiency loss due to a thermally perfect gas helps understand the efficiency loss between the arc discharge energy and the measured peak cavity pressure.

$$C_v(T) = C_{v,p} \left( 1 + (\gamma_p - 1) \left[ \left( \frac{\theta}{T} \right)^2 \frac{e^{\theta/T}}{(e^{\theta/T} - 1)^2} \right] \right) \quad (40)$$

$$Q_T = mC_{v,p}(T_2 - T_1) \quad (41)$$

$$\eta_T = Q_T/Q_C \quad (42)$$

Finally, the measured peak pressure is used to determine the efficiency based on pressure measurements. Using Equation 43, the energy required to raise the cavity pressure to the measured peak pressure is determined also assuming the original calorically perfect assumptions. The ratio of  $Q_P$  to  $Q_C$  is used to calculate the pressure-based efficiency,  $\eta_P$ , as shown in Equation 44.

$$Q_P = \left( \frac{P_m}{\rho R T_1} - 1 \right) E \quad (43)$$

$$\eta_P = Q_P/Q_C \quad (44)$$

Data similar to that shown in Figure 34 were acquired over a range of cavity volumes, orifice diameters, and values of  $Q_C$ . Results showed that the orifice diameter had little to no effect on the peak pressure measurements as expected. However, the measurement of peak cavity pressure as a function of cavity volume,  $v$  and input energy,  $Q_C$ , did show variation applicable to Stage 1. These results are combined in Figure 37 as three sets of data points which represent data from three SparkJet volume tests over a range of  $Q_C$  values.

When plotted as a function of  $Q_C/E$ , which is both a function of cavity volume and input energy, the points from the three tests show a common trend. In general, the results demonstrate relatively high efficiency at low  $Q_C/E$  values and relatively low efficiency at high  $Q_C/E$  values. The efficiency,  $\eta_P$ , decreases from 40% to 20% over the entire range of  $Q_C/E$ . The drop in efficiency is likely due to an increased heat transfer to the actuator Macor housing and the electrodes and increasing inefficiencies as the cavity temperature increases above the calorically perfect gas assumption. The efficiency as a function of orifice diameter was not plotted because orifice diameter does not affect energy addition.

Further analysis of the pressure signals also pertains to the frequency content of each pressure signal. The frequency content was evaluated over a range of cavity volumes and input energies as shown in Figure 38. For each of the three cavity volumes investigated, Figure 38(a) shows the FFT of unfiltered pressure signals for  $Q_C/E \approx 27$ . Signals corresponding to similar  $Q_C/E$  values were selected because the volume-averaged temperature rise and, therefore, acoustic velocity are similar. Therefore, variations in frequency content are related to acoustic waves traveling at the same velocity, but the frequency of oscillations would be higher



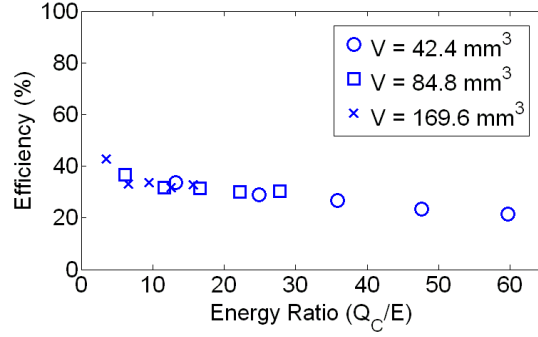


**Figure 37:** Variation of the peak cavity pressure as a function of  $Q/E$  for three SparkJet cavity volumes, an orifice diameter of 1 mm and an electrode gap of 1.75 mm.

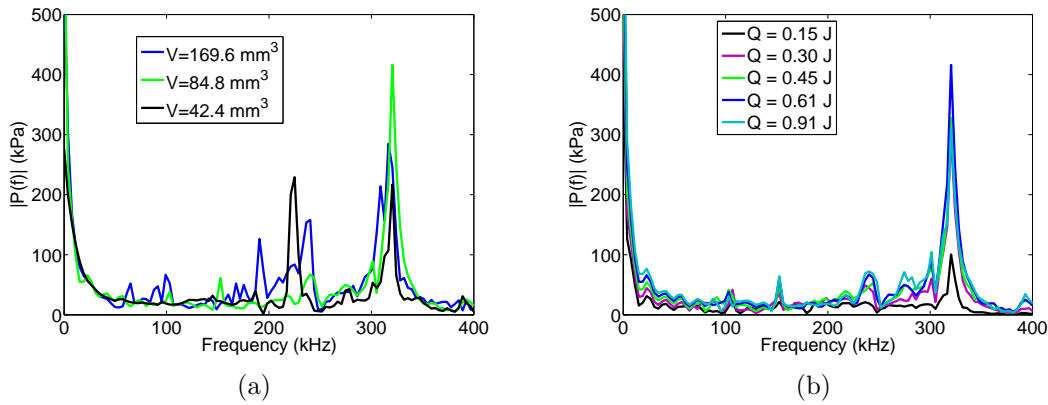


**Figure 38:** Fast-Fourier transform of ensemble-averaged, unfiltered pressure data displaying the frequency content for a) three cavity volumes at similar  $Q_C/E$  values of approximately 27 and b) five input energies,  $Q_C$ , and constant cavity volume of  $84.8 \text{ mm}^3$ .

in a smaller volume than in a larger volume. Referring to Figure 38(a), the frequency content for the smallest volume is generally higher than the frequency content for the largest volume. Figure 38(b) shows the results corresponding to a single cavity volume ( $84.8 \text{ mm}^3$ ) over a range of input energy,  $Q_C$ . As input energy increases, the magnitude of the frequency content increases; however, the frequency content itself does not vary over the range of energies evaluated. Therefore, these data suggest the variation in acoustic speed as a result of increased input energy is not significant.

Another feature of the FFT signals shown in Figure 38(a) is a dominant signal near 310-320 kHz. Because this frequency is independent of cavity volume, it is assumed that this frequency is actually associated with the resonant frequency of the pressure sensor mentioned earlier in the section discussing pressure signal filtering. The same frequency peak is also visible in Figure 38(b).

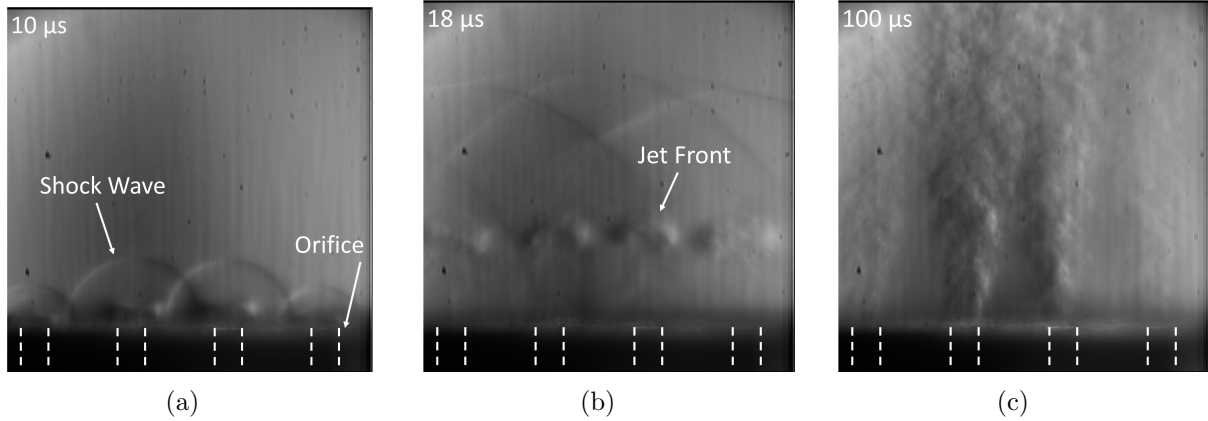


**Figure 39:** Time delayed images using LBMS of the SparkJet exhaust at (a) 10  $\mu\text{s}$ , (b) 18  $\mu\text{s}$ , and (c) 100  $\mu\text{s}$ .

### Flow Visualization

A major contribution from the collaborative effort from FSU has been in the form of microschlieren imagery of the SparkJet flow during Stage 2 of the actuation cycle. FSU achieved images with high spatial and temporal resolution made possible by a 10 ns light source illuminating a small flow region appropriate for the SparkJet flowfield. Full details of the microschlieren setup are available in Reference [25].

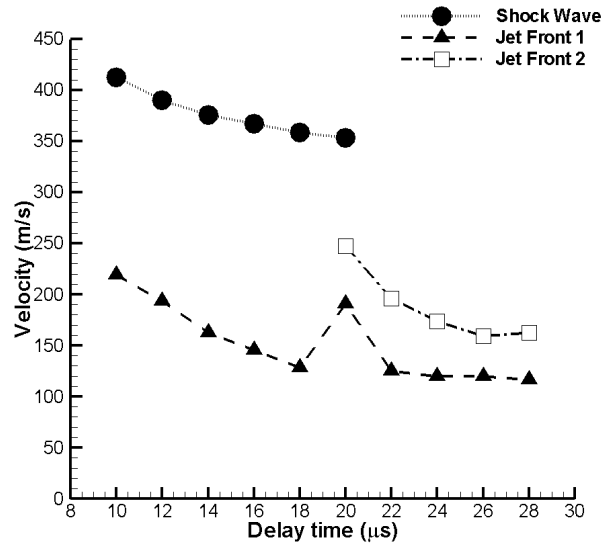
The flowfield associated with the SparkJet array was visualized at multiple time delays for which  $t = 0$  corresponds to the rising edge of the low-voltage signal to initiate the SparkJet operation. Images were acquired starting at an 8  $\mu\text{s}$  delay, which is when the shock wave generated by the arc discharge is first seen exiting from the orifice array, up to a delay of 100  $\mu\text{s}$ . Instantaneous images from several of these time delays are shown in Figure 39. Two of the key features present in this flow field are the initial shock wave identified at a time delay of 10  $\mu\text{s}$  in Figure 39(a) and the jet front shown at a delay of 18  $\mu\text{s}$  in Figure 39(b). The exhaust continues to be visible at time delays up to 100  $\mu\text{s}$ .

To gain further understanding of the behavior of the SparkJet exhaust, multiple images were averaged at each time delay to estimate the velocity of the shock wave, jet front, and secondary jet front shown in Figure 40(b). Due to variation ( $\leq 1 \mu\text{s}$ ) in the time between the trigger signal and the arc discharge, the data from the photodiode was used to select only the images acquired within the order of 10 ns of the expected delay for averaging. Figure 40(a) lists the number of images averaged for each time step. The shock wave and jet front exit the orifice array at a maximum velocity of 420 m/s and 225 m/s respectively, which decays over time. Further details related to the blast wave and jet front velocities are discussed in the complimentary report by FSU.

One of the goals of the bench top characterization of the SparkJet actuator was to verify supersonic flow in the exhaust predicted by CFD results [29] and as seen experimentally in similar jet flows [47]. Evidence of supersonic flow was observed and presented in Refer-

Delay Time	Images Averaged
8 $\mu\text{s}$	78
10 $\mu\text{s}$	65
12 $\mu\text{s}$	84
14 $\mu\text{s}$	71
16 $\mu\text{s}$	77
18 $\mu\text{s}$	53
20 $\mu\text{s}$	33
22 $\mu\text{s}$	18
24 $\mu\text{s}$	24
26 $\mu\text{s}$	39
28 $\mu\text{s}$	42
30 $\mu\text{s}$	24

(a)



(b)

**Figure 40:** Flow feature velocity analysis: a) table of the number of microschlieren images at each time delay and b) velocity of the jet front and shock waves at various time delays.

ence [25]. It was initially ruled out as a reflected shock from inside of the cavity passing through the jet front. However, the fact that it remains in the jet front for these consecutive time delays suggests that it is not passing through the jet front, but traveling with it. If this is indeed a shock inside of the jet front, then there is locally supersonic flow inside of the exhaust from the SparkJet.

### Variation with Electrode Gap

While the main goal of introducing the pseudo-series trigger circuit was to increase reliability, an unexpected benefit was the ability to increase the maximum electrode gap up to 4.0 mm at 1 atm. This benefit was explored experimentally by varying the electrode gap and quantifying the corresponding peak cavity pressure. The SparkJet actuator used to quantify the effect of changing the trigger mechanism on efficiency is identical to that described earlier except without a trigger electrode as shown in Figure 41. The SparkJet had a cavity volume of  $84.8 \text{ mm}^3$ , an orifice diameter of 1 mm and the electrode gap was evaluated at 3.0 mm and 4.0 mm.

Testing demonstrates that increasing the electrode gap also increases the thermal energy deposition in the working fluid during Stage 1. Figure 42 shows the internal cavity pressure as a function of time for an idealized arc discharge that is 100% efficient and three experimental setups with electrode gaps of 1.7 mm, 3.0 mm and 4.0 mm. The curve corresponding to a gap of 1.7 mm represents the approximate maximum gap size wherein discharges are achievable with the external trigger circuit. The curves corresponding to 3.0 mm and 4.0 mm represent the gap sizes with achievable discharges using the new pseudo-series trigger mechanism.

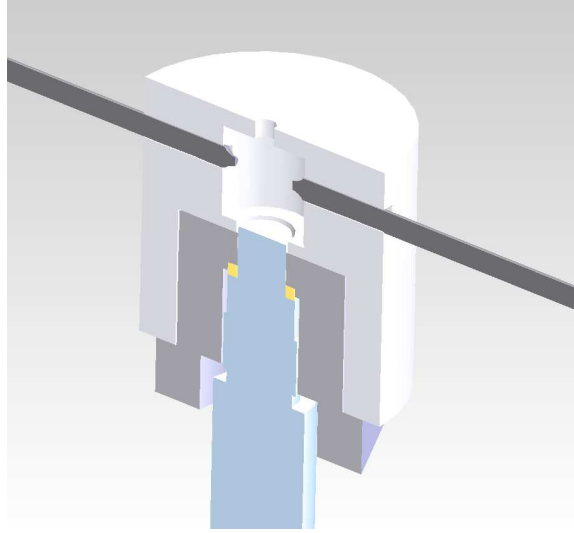


**Figure 41:** CAD representation of the SparkJet actuator designed for a pseudo-series trigger with a pressure sensor installed.

This plot clearly shows that increasing the electrode gap increases the energy transferred from the arc to the surrounding air during Stage 1. The larger electrode gap results in a longer arc column and larger arc column surface area through which heat is transferred to the surrounding air. In addition, larger electrode gaps possess larger resistance such that increased power is drawn across the arc rather than the wires. Figure 43 summarizes the curves shown in Figure 42 over a wide range of  $Q_C/E$  values. This plot shows that efficiency as a function of  $Q_C/E$  for various gap sizes follow similar exponentially decreasing trends. As such, the largest change to the efficiency is seen for  $Q_C/E$  near 10 where the efficiency rises from 30% to 75% for a tip distance change from 1.7 mm to 4.0 mm, respectively.

Again, flow visualization was utilized to capture and compare the flow field to view the effect of doubling the electrode gap to 3.0 mm while keeping the input energy,  $Q_C$ , constant. The goal of these visualization studies was to quantify the velocity of the dominant flow features (blast wave and jet front) and verify that the velocities are similar. Figure 44 shows the measured velocities of the jet front and blast waves for the different triggering mechanism. This plot shows that the flow feature velocities are very similar despite the lower energy input from the external trigger tests. Here, another experimental measurements confirms that increasing the electrode gap leads to a more efficient SparkJet design such that less electrical energy is required to create the same jet momentum output.

## 5 Arc Power Measurements

In order to investigate the source of the low pressure-based efficiencies shown in the previous section, the power drawn by the arc has been evaluated using the 600ET circuit. The arc discharge power was evaluated for a SparkJet with a cavity volume of 84.8 mm<sup>3</sup>, capacitor voltage of approximately 600 V, and six capacitance values ranging from 0.95  $\mu$ F to 5.13  $\mu$ F.

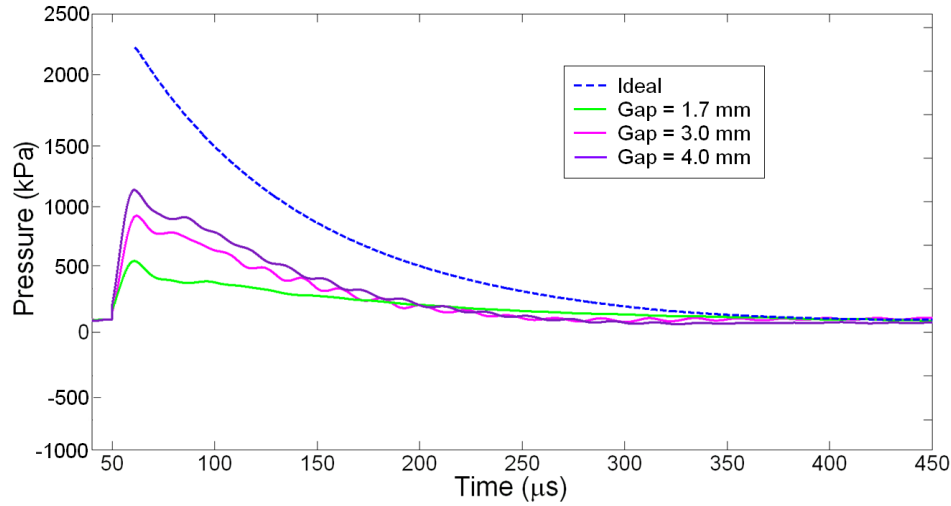


**Figure 42:** Comparison of pressure vs. time for three electrode gaps of 1.7, 3.0, and 4.0 mm given the same cavity volume ( $84.4 \text{ mm}^3$ ), orifice diameter (1.0 mm), and approximately similar  $Q_C/E$  of 30.

## 5.1 Results

Corresponding to each capacitance value, Figure 45 shows six current, voltage and power waveforms. Figure 45(a) shows that as capacitance increases, both the current magnitude and period increase. Correspondingly, Figure 45(b) shows that as capacitance increases, the time for the voltage drop increases such that the time derivative of the voltage drop during the arc discharge decreases in magnitude. These figures also show that even after the discharge is complete, as indicated when the current reaches zero, inductance in the circuit drives the voltage and current to continue to oscillate. Also shown in Figure 45(c) is the instantaneous power drawn by the arc which reaches a maximum value between 50 and 120 kW, and the entire energy discharge lasts 2-6  $\mu\text{s}$ .

With an understanding of the voltage, current and power measurements during the arc discharge process, the energy drawn by the arc is calculated by integrating the power curve according to Equation 38. The energy drawn is divided by the stored capacitor energy,  $Q_C$ , to calculate the capacitor to arc power efficiency and the results are shown by the magenta triangles in Figure 46. These results show that only 35-50% of the energy stored in the charged capacitor bank is converted to power drawn by the arc. These significant losses are likely due to the parasitic resistance and inductance corresponding to the 18 inches of 22 AWG wires leading from the capacitors to the arc. For comparison, the pressure-based efficiency for these tests is shown by the blue squares using the same analysis as described in Section 4. These pressure-based efficiencies show that the conversion of energy stored in the capacitors to the energy required to raise the cavity pressure (assuming calorically perfect and ideal gas) is 15-25% efficient. To explain some of the additional efficiency losses and estimate temperature rise in the cavity, the instantaneous arc discharge and calorically perfect gas assumptions are removed.

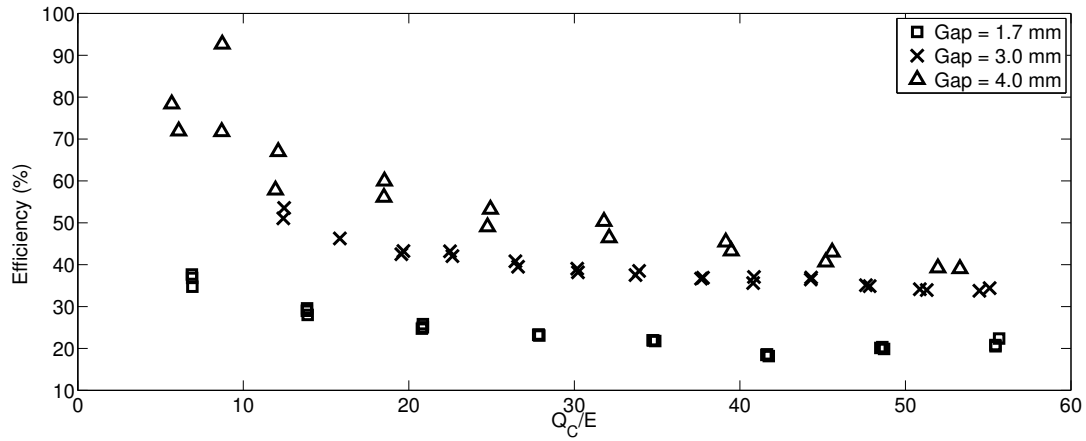


**Figure 43:** Comparison of efficiency vs.  $Q_C/E$  for three electrode gaps of 1.7, 3.0, and 4.0 mm given the same cavity volume ( $84.8 \text{ mm}^3$ ).

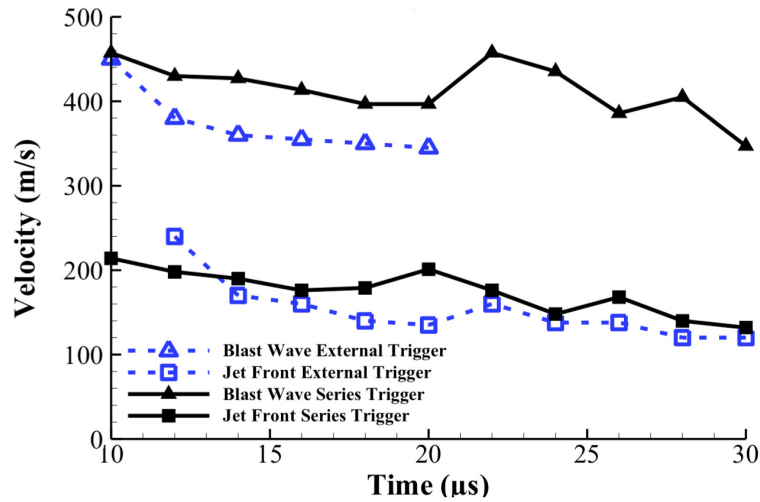
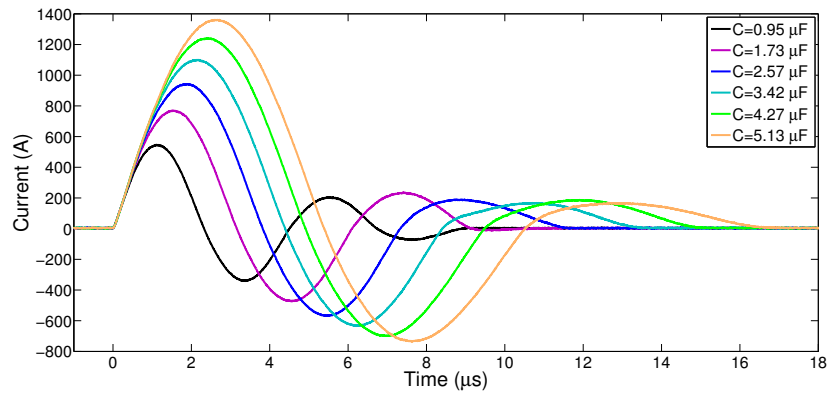
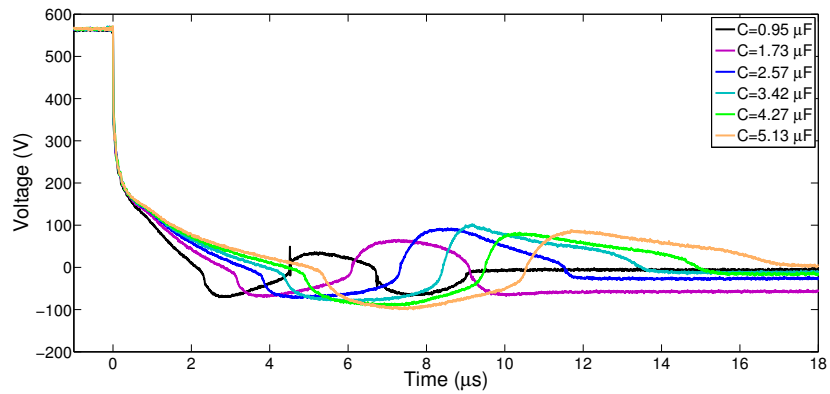


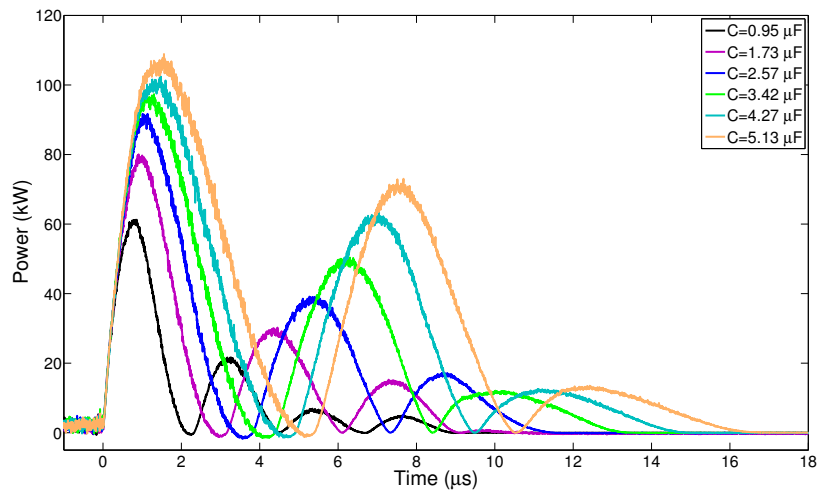
**Figure 44:** Comparison of the jet front and blast wave velocities using the external trigger mechanism at  $Q_C$  of 25.5 and electrode gap of 1.7 mm and the pseudo-series trigger mechanism at  $Q_C$  of 12.7 and electrode gap of 3.0 mm.



(a) Current Waveforms.



(b) Voltage Waveforms.



(c) Power Waveforms.

**Figure 45:** Voltage and current waveform curves in distinct groups corresponding to each capacitance change for a cavity volume of 84.8 mm<sup>3</sup>.

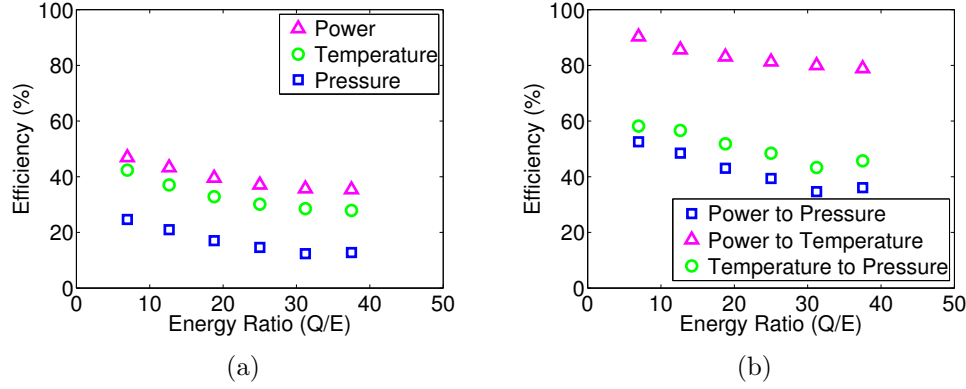


**Figure 46:** Efficiency of the conversion of stored capacitor energy to the arc discharge, calculated cavity temperature, and measured pressure rise as a function of  $Q_C/E$ .

## 5.2 Analysis of Energy Losses

To further analyze the energy losses, the results shown in Figure 46a are replotted in Figure 46b with efficiencies calculated using the actual arc power drawn, which removes circuit-based losses from the efficiency calculations. Therefore, the efficiency of converting arc power to pressurizing the SparkJet cavity is now shown to range from 35-55%. Also, the efficiency of converting from arc power to temperature assuming a thermally perfect gas and non-instantaneous energy deposition ranges from 80-90%. Finally, converting temperature to cavity pressure is 45-60% efficient. Again, these losses are likely due to heat lost to the electrodes. In addition, the assumption that the heat generated by the arc is immediately added to the entire volume of air in the cavity is challenged. The heat is initially localized to the arc itself which dissipates away to the cavity air and electrodes. Therefore, localized heating and high-temperature effects such as thermal radiation losses and gas dissociation also contribute to the efficiency losses between  $Q_A$  and  $Q_C$ .

The third set of points in Figure 46 correspond to the estimated efficiency based on the non-instantaneous, thermally perfect energy addition where  $Q_C = 1.6$  J ( $C = 5.13$   $\mu$ F). The effect of assuming a thermally perfect gas according to Equation 40 is shown in Figure 47. This figure shows the current and voltage across the arc discharge which results in the energy deposition into the cavity. Assuming a non-instantaneous energy deposition into a calorically perfect gas where  $C_v$  is constant, the black curve shows the corresponding temperature variation. For comparison, the non-instantaneous energy deposition into a *thermally* perfect gas is shown with the magenta curve. The corresponding variation in the specific heat constant is also shown for reference with the green curve. This comparison shows that incorporating a thermally perfect assumption reduces the final cavity temperature up to 1000 K. The temperature difference assuming a thermally perfect gas increases as  $Q_C$  increases as shown in Figure 47(b). Based on this analysis, these assumptions account for approximately 5-10% of the pressure-based efficiency losses.

The remaining pressure-based efficiency losses are most likely due to heat loss to the elec-



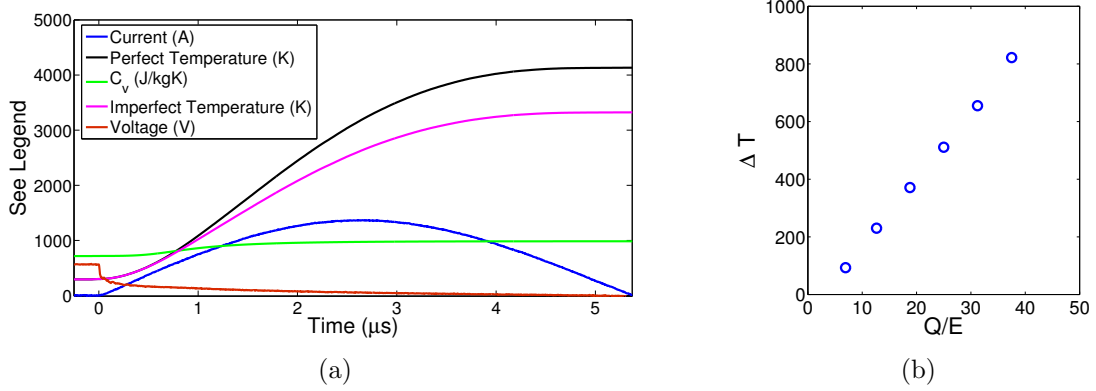


**Figure 47:** Comparison of the time dependent temperature and specific heat coefficient ( $C_v$ ) assuming a calorically perfect and imperfect gas as a function of arc discharge current and voltage for (a) a single case and (b) over a range of  $Q_C/E$  values.

trodes. Roth et al.[45] measured heat loss to electrodes due to arc discharges in a variety of gases and for a range of electrode spacings and electrode diameters. While none of the tests were in air, the thermal diffusivity of Argon, one of the gases tested, is very similar to that of air. Roth also tested heat loss for electrodes of a diameter of 1 mm and electrode gap of 2 mm in Argon pressurized at 1 atm. The results showed that approximately 50% of the heat generated by the arc discharge was lost to the electrodes. The heat loss is quite significant but, based on the results presented by Roth, can be significantly reduced by increasing the electrode gap. Recently, pressure-based measurements by JHU/APL provide supporting evidence that increasing the electrode gap in the SparkJet does, in fact, increase the pressure-based efficiency[48].

Through this analysis, the source of efficiency losses during Stage 1 of the SparkJet cycle are better understood. With an understanding of the losses, the SparkJet design can be improved to minimize losses. For example, the wires leading from the capacitors to the electrode gap should be shortened and of a lower wire gauge. Also, the circuit should be designed to promote larger electrode gaps to not only reduce heat loss to the electrodes, but also enlarge the arc channel to disperse heat from the arc to the surrounding air more quickly. Another advantage of increasing the electrode gap is the reduced electric field at the electrode tips such that the arc resistance relative to the parasitic wire resistance is increased; subsequently, the relative power drawn by the arc is higher than the power drawn by the wires.

## 6 Design Optimization

### 6.1 Electrode Design

Several SparkJet experiments[25, 49, 50] used electrodes made of 1 mm diameter 1.5% lanthanated tungsten rods, cut to approximately 25.4-50.8 mm lengths with the tips roughly

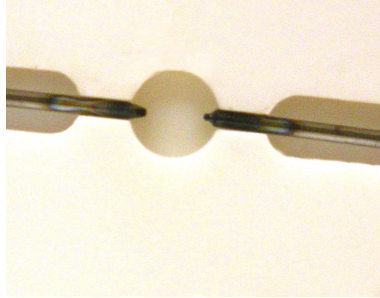


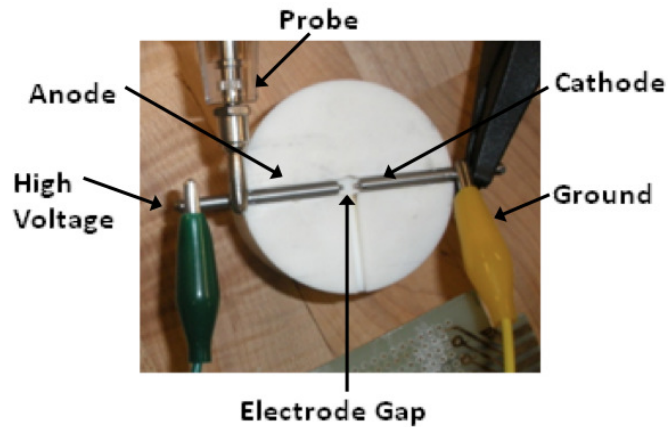
**Figure 48:** Tungsten oxidation caused by overheating on 1 mm diameter electrodes after operation at high frequency and subsequent overheating.

shaped with a Dremel grinding wheel. As soon as the focus turned to high-frequency actuation testing, investigation into electrode design became important. The electrode design optimization studies did not require enclosing the arc in a cavity since the goal of these studies was to ensure reliable arc initiation and electrode survivability independent of the cavity conditions. The system considerations associated with high-frequency SparkJet actuation led to several design trade-off studies.

Several problems became evident as actuation frequency and the burst duration at a given actuation frequency increased. For example, a sequence of 500 bursts at 1 kHz would cause the electrodes to overheat near the electrode tips. Up to the moment (approximately 10-50 cycles at 1 kHz) when the electrode tips exceeded a certain unknown temperature, the SparkJet fired properly. However, after the tips reached a certain temperature, misfiring became significant. This effect appeared to be independent of changes to the electrode surface due to previous burst sequences. An example of tungsten oxidation after high-frequency operation is shown in Figure 48. Hence, the first design parameter considered was the electrode diameter such that the heat generated by the arc could be dissipated more quickly through the larger electrodes. The electrode diameter was increased to 3.175 mm while maintaining a consistent length of 38.1 mm to determine if this phenomenon was, in fact, due to overheating of the electrodes. The electrode gap for all electrode testing was maintained at 2.5 mm.

In parallel with changes to the electrode diameter, an optimal and consistent tip shape needed to be determined to be used in future designs. Research into arc lamp[51], spark plug[52] and welding studies[53], indicated that the truncated cone, cylinder, pointed and hemispherical tips were typical shapes used for applications where arcs are encountered. Some tip shape options were not considered. For example, a pointed tip would result in large electric field amplification; this is preferred for initiating the arc across a large gap but it is very susceptible to tip deformation with each discharge. The resultant changes to the tip shape would quickly reduce reliability and lifetime of the SparkJet actuator. By contrast, a hemispherical electrode tip would demonstrate increased reliability because the smooth, continuous shape would result in very little electric field amplification; however, to initiate an arc, the electrode gap must be reduced.

As the results from the trigger modification study showed in Figures 42 and 43, maximizing

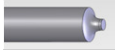


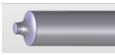








**Figure 49:** Photograph of the electrode design test setup for the pseudo-series triggering SparkJet design.

the electrode gap is desired. Therefore, this work focused on truncated cone and cylinder tip shapes because these shapes feature both sharp corners and electrode mass near the tips. Both tip shapes were designed such that the diameter at the tip was 1 mm. Experimental configurations included a cylindrical tip on the anode with a truncated cone tip on the cathode, a cylindrical tip on the cathode with a truncated cone tip on the anode and cases where both the anode and cathode had either a cylindrical tip or truncated cone tip. An example of how these shapes were tested is shown in Figure 49 where both the anode and cathode have cylindrical tip shapes.











The material selection was primarily driven by the need for electrode tip survivability, meaning that the electrode tips maintained their shape. Therefore, only pure tungsten or tungsten alloys were tested. These alloys included lanthanated, ceriated and zirconiased tungsten alloys, pure tungsten and a 30% copper/70% tungsten alloy in a class of materials known as Elkonite.

The results of these studies showed that actuator performance is significantly affected by the choice of tip shape and less significantly affected by material choice when operated at a fixed frequency of 500 Hz. The cylindrical tip shape for both the anode and cathode resulted in the best actuator performance with a low (0% to 5%) misfire percentage whereas the truncated cone tip shape resulted in failure of arc initiation altogether. The superior performance of the cylinder shape is likely caused by the electric field amplification due to the sharper corners of the cylinder. However, the difference in reliability could also be related to an impedance mismatch which is discussed later. The studies conducted to analyze electrode material performance based on the observed damage to the electrode tips is summarized in Table 2. The tungsten alloys all performed similarly and maintained the original tip shape well. The only material tested that did not exhibit good survivability was the copper/tungsten electrodes. The addition of copper led to significant alteration to the tip shape and the SparkJet misfired significantly after several burst sequences.

Anode (600 V)	Cathode (Gnd)	Material	Diameter	Length	Gap	Survivability
		Lanthanated Tungsten	3.175 mm	38.1 mm	2.5 mm	Minimal Wear
		Ceriated Tungsten	3.175 mm	38.1 mm	2.5 mm	Minimal Wear
		Zirconiated Tungsten	3.175 mm	38.1 mm	2.5 mm	Minimal Wear
		Pure Tungsten	3.175 mm	38.1 mm	2.5 mm	Minimal Wear
		Elkonite	3.175 mm	38.1 mm	2.5 mm	Significant Damage

**Table 2:** Design parameters tested to determine the effect of electrode material on electrode survivability.

During testing of the large diameter electrodes, a new issue affecting reliability was observed. For burst sequences at actuation frequencies higher than 500-600 Hz, the arc would fire once and then never again until the next burst sequences was initiated. For burst sequences at actuation frequencies lower than the observed cutoff frequency, the arc would fire with zero or very few misfires. In an attempt to understand this behavior, electrodes of the same material (pure tungsten), tip shape (cylinder), and length (38.1 mm) were evaluated as a function of electrode diameter. A summary of the results is shown in Table 3. Since the power supply for the SparkJet has a maximum operating frequency of 1 kHz, electrode diameters which fired successfully at 1 kHz are indicated as having a cutoff frequency greater than 1 kHz. Results showed that the observed cutoff frequency increased as electrode the length-to-diameter ratio increased; specifically, a length-to-diameter ratio above 24 results in a cutoff frequency above 1 kHz.

Anode (600 V)	Cathode (Gnd)	Material	Diameter	Length	L/ D	Gap	Cutoff Frequency
		Pure Tungsten	3.175 mm	38.1 mm	12	2.5 mm	500 Hz
		Pure Tungsten	2.38 mm	38.1 mm	16	2.5 mm	900 Hz
		Pure Tungsten	1.587 mm	38.1 mm	24	2.5 mm	>1000 Hz
		Pure Tungsten	1.0 mm	38.1 mm	38	2.5 mm	>1000 Hz
		Pure Tungsten	3.175 mm	203.2 mm	64	2.5 mm	>1000 Hz

**Table 3:** Design parameters tested to determine the effect of electrode diameter on frequency cutoff.

This behavior appeared to mimic basic RC circuit operation, and further investigation led to the realization that impedance matching between the arc and the rest of the circuit was affecting the arc initiation. Based on cylindrical antenna fundamentals [16], the electrode length-to-diameter ratio is a parameter that can be used to control impedance. While small in magnitude, the inherent resistance, inductance and capacitance in the electrodes could be sufficient to affect the overall SparkJet performance as frequency increases. Therefore, the 38.1 mm long 3.175 mm diameter electrodes were exchanged for 203.2 mm long and 3.175 mm diameter electrodes to quickly test this hypothesis. The resulting test showed successful results with zero misfires for a burst sequence of 500 at 1 kHz as indicated in the last row of Table 3. Since impedance is affected by arc resistance, the conclusions based on electrode tip shape and electrode material are linked to impedance matching. This series of electrode design optimization testing has confirmed that relatively large diameter electrodes are beneficial for thermal management. However, further testing is required to understand the impedance of the complete SparkJet circuit.

## 6.2 Non-ZNMF Design

To investigate momentum throughput as a function of frequency and the potential benefits during high-frequency actuation, a preliminary design for a non-ZNMF SparkJet actuator was considered. This design included an external air supply feeding into the cavity to assist the refresh cycle, Stage 3, and was tested using the 600PST circuit. The air supply was situated perpendicular to the anode and cathode through the side wall of the cavity at the same height of the electrodes. Figure 50 shows a CAD representation of the non-ZNMF SparkJet cavity through the transparent Macor housing which highlights the air supply port, orifice array and pressure sensor access. The SparkJet used for this test was designed and constructed at JHU/APL and benchtop tested at FSU/AAPL. A check valve was installed just upstream of where the air supply met the cavity. The air supply gage pressure was set to 1.3 psig. Above 1.3 psig, the SparkJet failed to fire. The suspected cause of the SparkJet failure was the air flow from the air supply was preventing the trigger spark from spanning the electrode gap and that the air supply was essentially blowing out the trigger spark.

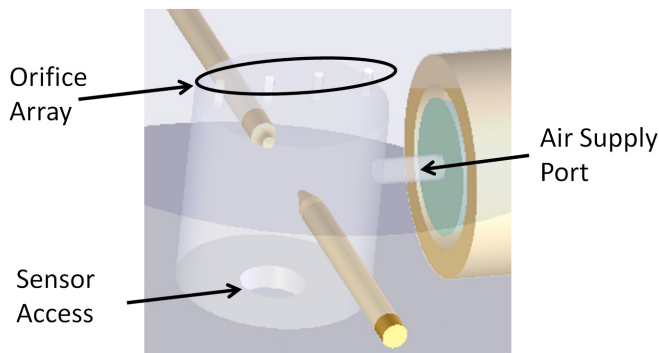


**Figure 50:** CAD representation of the non-ZNMF SparkJet design showing the air supply port, orifice array and pressure sensor access hole.

Therefore, the position of the air supply was adjusted such that the air flow would curve

around the cavity walls rather than through the electrode gap. Figure 51 shows the actual design tested which incorporated the adjustment of the air supply position. Also note in this figure that the check valve was moved farther away from the cavity to fit the air supply close to the cathode (ground). Regardless, Kapton tape was used as a precaution to prevent any possible arcing between the cathode and the air supply. Using this new design, a supply pressure up to 3.0 psig could be used for the non-ZNMF design testing. Microschlieren

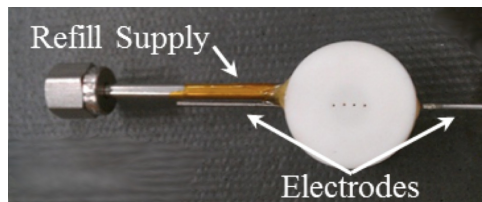


**Figure 51:** Photograph of the non-ZNMF SparkJet array design tested.

images of the SparkJet array flow for varying air supply pressure (0, 1.3, and 3.0 psig) and operating under varying frequency (500, 700, and 1000 Hz) were acquired at a time delay of 20  $\mu$ s after the 10th arc discharge in a burst of discharges. The images shown in Figure 52 show the variation in jet formation as a function of air supply pressure. These effect of varying frequency and further analysis of the non-ZNMF results are presented in the complimentary report by FSU.

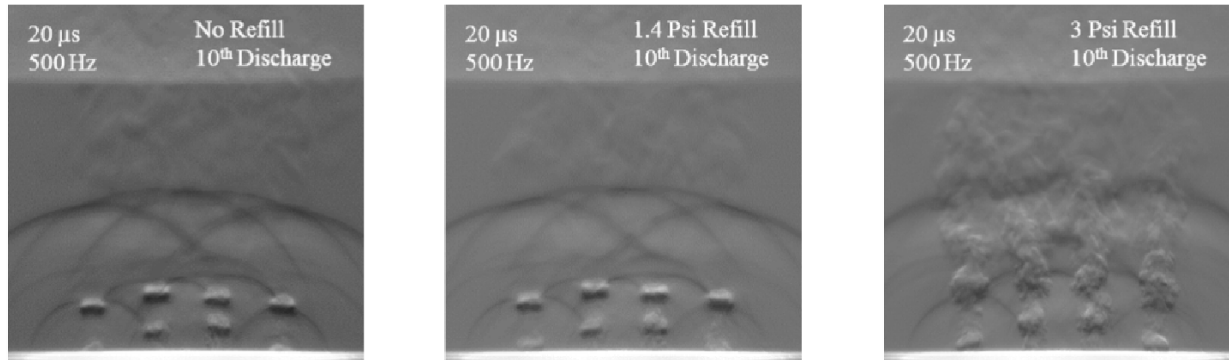


**Figure 52:** Microschlieren imagery of the non-ZNMF SparkJet array interacting with quiescent flow at varying air supply pressure.

## 7 Wind Tunnel Testing

Toward investigation of the flow interactions between an array of SparkJet actuators and a supersonic crossflow, JHU/APL has supported the wind tunnel tests performed at FSU/AAPL by providing the SparkJet actuator and supporting electronics. The wind tunnel testing requirements has also been a driver in improving the SparkJet reliability mentioned earlier in this report. All wind tunnel SparkJet arrays consist of three cavities each with one pair of electrodes and four orifices with an orifice diameter of 0.4 mm. The arc discharge across

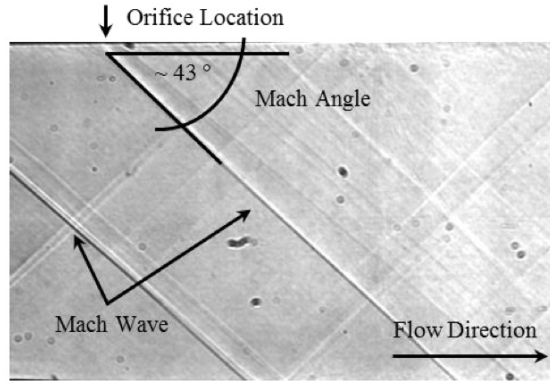


**Figure 53:** Example of the perturbed supersonic flow and demonstration of how the oblique shock angles are defined.

each electrode pair is supplied by three identical power supply setups and the trigger timing is controlled by a single low voltage square wave to ensure concurrent firing. During initial wind tunnel testing, JHU/APL also provided on-site support to maintain SparkJet operation.

A z-type focusing shadowgraph system with two parabolic and two  $45^\circ$  mirrors was used for wind tunnel flow visualization. The light source used was a white-light Xenon flash lamp capable of being pulsed up to a frequency of 1 kHz with a pulse duration of  $5\ \mu\text{s}$ . While the SparkJet was operating in single-shot mode, a LaVision Imager Pro-X camera was used with DaVis 7.2 software for image acquisition. The SparkJet, light source, camera, and data acquisition were triggered using a DG-535 delay generator. The SparkJet actuator array (three cavities with four orifices each) was operated at 40 bursts every second at 700 Hz and the interactions with a Mach 1.5 crossflow over a flat plate have been visualized. Additional wind tunnel visualization experimental details have been published previously[50]. Figure 53 shows an example of the perturbed supersonic flow and also provides a definition of oblique shock angle measurements referenced later.

Figure 54 shows how the supersonic crossflow evolves as the SparkJet actuator cycle progresses from 0-700  $\mu\text{s}$ . The images corresponding to a time delay of 75-275  $\mu\text{s}$  reveal the presence of blast waves downstream of the oblique shock in the expansion fan which steadily propagate away from the SparkJet orifices. As the blast waves move away from the orifices, the oblique shock wave is pushed slightly upstream and remains so for the remaining images.

The oblique shock angle evolution as a function of time is plotted in Figure 55. The maximum oblique shock angle of approximately  $48^\circ$ , which is equivalent to a  $5^\circ$  turning angle, occurs 250-275  $\mu\text{s}$  after the SparkJet is fired. The image corresponding to a time delay of 350  $\mu\text{s}$  shows that the oblique shock has propagated across the entire length of the test section and has a measured angle of  $47^\circ$ . The oblique shock angle is approximately  $46^\circ$  at a time delay of 500  $\mu\text{s}$  and at an angle of  $45^\circ$ , 700  $\mu\text{s}$  after the SparkJet has discharged. It is assumed that the shock wave will asymptotically return to a Mach wave at extended time delays.



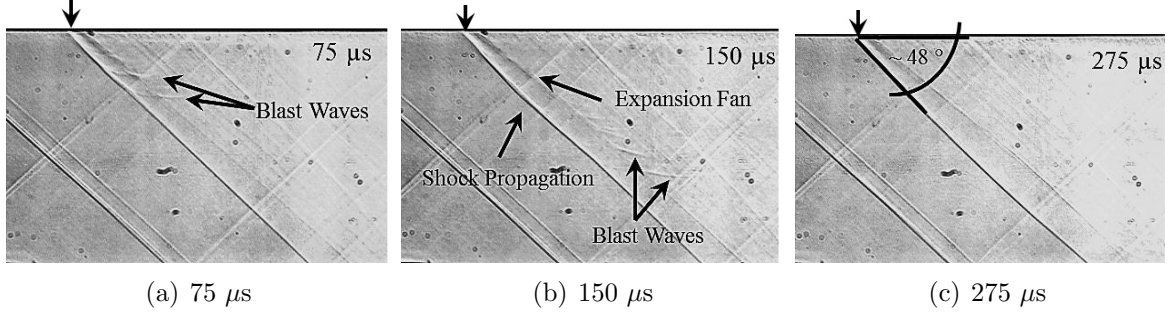


**Figure 54:** Shadowgraph image of the baseline Mach 1.5 crossflow over a flat plate at various time delays.

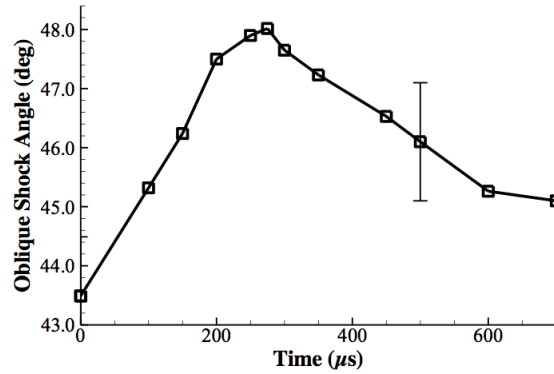


**Figure 55:** Oblique shock angle variation as a function of time.

## 8 Conclusions

Development of a high-momentum, unsteady active flow control device is required to properly control high-speed flow environments such as a supersonic open cavity. Under this grant, a device intended to satisfy the needs of high-speed flow control, the SparkJet, has been further developed, modeled and demonstrated in a high-speed environment. There are a multitude of adjustable design parameters which can be tailored to a specific application. Through numerical modeling and experimental efforts, these design parameters are becoming better understood.

The primary purpose of this grant was to study flow phenomena present during flow control applications, namely, flow interactions between an array of SparkJet actuators and a supersonic flow. This report provides a synopsis of SparkJet fluid and plasma physics, modeling options and assumptions, and a look at design optimization efforts and the corresponding benefits. As a collaborative effort with FSU/AAPL, efforts at JHU/APL primarily involved developing the SparkJet actuator such that it could operate reliably at high-frequency and produce a high-momentum jet. The highlights of the wind tunnel testing have been docu-



mented in this report demonstrating a measurable flow response due to a SparkJet array. FSU/AAPL will also release a complimentary report summarizing SparkJet benchtop and wind tunnel experimental results using flow visualization and including detailed discussion of those results.

Through the development of a 1-D numerical model, several design parameters were investigated with the interest of understanding the effect on jet momentum as actuation frequency increased. Of primary interest were cavity volume, input energy, and orifice diameter. The simulation showed that only cavity volume and orifice diameter affected high-frequency performance. For orifice diameters of 0.4, 1.0, and 2.0 mm, modeling results showed that, as orifice diameter increases, the high-frequency performance improves. For cavity volumes of 42.4, 84.8, and 169.6 mm<sup>3</sup>, modeling results show that, as cavity volume increases, the high-frequency performance degrades. Modeling results showed, however, that variation in the input energy from 0.24 to 0.90 J does not affect high-frequency performance. The trends related to orifice diameter and cavity volume suggest that parameters that shorten the SparkJet cycle duration are beneficial to high-frequency performance. With this conclusion in mind, another design parameter to consider is the thermal conductivity of the SparkJet walls. If the heat transfer rate is increased, the SparkJet cycle duration is also reduced and, therefore, high-frequency performance should also improve.

The 1-D modeling results also showed that the modeling assumptions led to an overestimation of the energy transferred to the cavity air. Stage 1 of the SparkJet process involves complex plasma dynamics and requires an understanding of the SparkJet power supply circuit. Experimental measurements of the internal cavity pressure and power drawn by the arc discharge show that the conversion from stored capacitor energy to work on the cavity air in the form of pressure is not 100% efficient. The conversion of energy from the capacitors to the arc is primarily based on circuit design and the resistance associated with the electrode gap. The efficiency of this energy conversion varies with  $Q_C/E$  but ranges from 40-50%. However, by increasing the resistance of the electrode gap relative to the circuit resistance, the power drawn by the arc is also increased. Experimental results show that this can be accomplished by increasing the electrode gap distance. The conversion of energy from the arc to thermal energy to work done by the increased pressure is primarily controlled by thermal losses to electrodes and thermally perfect effects. The efficiency of converting arc energy to thermal energy ranges from 80-90%, and the efficiency of converting thermal energy to raising the cavity pressure ranges from 35-50%. Knowledge of the sources of these inefficiencies allows a designer to account for the expected energy losses and design the actuator to minimize the energy losses when possible.

Actuator design modifications were motivated by a feedback process with FSU/AAPL. The resulting investigation into electrode design and the triggering mechanism led to significantly improved actuator reliability. In fact, the change to the trigger mechanism also allowed for larger electrode gaps which led to improved actuator efficiency. The electrode design modifications included increasing the electrode diameter and identifying a reliable electrode material. Increased electrode diameter from 1.0 mm to 3.175 mm improved reliability during high-frequency operation. The electrode material experiments showed that a variety of tung-

sten alloys with greater than 97% tungsten are capable of surviving the arc environment. A separate design modification was also made to allow for an external air supply to reduce the duration of Stage 3. Microschlieren images suggest that this modification improved jet momentum as both the air supply pressure and actuation frequency increased.

Understanding of the SparkJet operation, significant design parameters, and design challenges have been well developed as demonstrated in this report. With this broad knowledge of the actuator, future work toward applying the SparkJet technology to real applications is required. Applications such as supersonic open cavity flow, high-speed inlets, jet noise mitigation and vehicle steering are examples of excellent applications for the SparkJet actuator. For each application, the ideal frequency range and required jet momentum will be achieved by careful control of the SparkJet actuator through the multitude of design parameters available for adjustment.

## 9 Future Work

There are several areas of interest for future work pertaining to the SparkJet actuator itself. High-fidelity CFD modeling of an array of SparkJet actuators in a large-scale flow environment presents several computational challenges and would represent a significant contribution to the flow control community in general. In addition, expansion of the 1-D modeling to include interactions with an external flow and neighboring actuators would be beneficial for rapid design optimization. For high-frequency actuation, the non-ZNMF design should be further studied with an external flow environment. The quiescent benchtop results in this report show beneficial changes to the SparkJet flowfield which need to be explored in a wind tunnel testing environment. Finally, the most important future work includes wind tunnel testing to demonstrate and evaluate SparkJet effectiveness against a variety of flow environments.

## 10 Acknowledgements

This work was sponsored by the AFOSR through a research grant monitored by Dr. Doug Smith. (The views expressed in this paper are not necessarily endorsed by the AFOSR.) There is no property to report under this grant. The authors also thank Mr. Bruce Land, III for his important contributions to the SparkJet power supplies and circuits, Mr. John Teehan for machining the SparkJet components, and Dr. Jerry Emhoff his contributions to the modeling efforts.

## 11 References

- [1] Rossiter, J., *Wind-tunnel Experiments on the Flow Over Rectangular Cavities at Subsonic and Transonic Speeds*, H.M. Stationery Office, 1967.

- [2] United States Air Force, "F-22A Raptor," <http://www.af.mil/shared/media/photodb/photos/070713-F-0986R-007.jpg>, 2007, Online accessed March 2013.
- [3] Zhuang, N., Alvi, F. S., Alkisar, M. B., and Shih, C., "Supersonic Cavity Flows and Their Control," *AIAA Journal*, Vol. 44, No. 9, September 2006.
- [4] Heller, H. H., Holmes, G., and Covert, E. E., "Flow-Induced Pressure Oscillations in Shallow Cavities," Tech. rep., Air Force Flight Dynamics Laboratory, December 1970, AFFDL-TR-70-104.
- [5] Chen, F. and Beeler, G. B., "Virtual Shaping of a Two-Dimensional NACA 0015 Airfoil using Synthetic Jet Actuator," 1st AIAA Flow Control Conference, June 2002, AIAA 2002-3273.
- [6] Deb, D., Tao, G., Burkholder, J. O., and Smith, D. R., "Adaptive Compensation Control of Synthetic Jet Actuator Arrays for Airfoil Virtual Shaping," *Journal of Aircraft*, Vol. 44, No. 2, March-April 2007.
- [7] Shneider, M. N., Macheret, S. O., Zaidi, S. H., Girgis, I., and Miles, R. B., "Virtual Shapes in Supersonic Flow Control with Energy Addition," *Journal of Propulsion and Power*, Vol. 24, No. 5, September-October 2008.
- [8] Kumar, R., Botu, A., Ali, Y., Alvi, F. S., and Venkatakrishnan, L., "Virtual Shock Shaping Using Microjet Arrays," 48th AIAA Aerospace Sciences Meeting, January 2010, AIAA 2010-0103.
- [9] Topoloski, M., Arora, N., Ali, M., Solomon, J., and Alvi, F., "Experiments on Resonance Enhanced Pulsed Microjet Actuators in Supersonic Crossflow," 6th AIAA Flow Control Conference, June 2012, AIAA 2012-2813.
- [10] Strickland, G., Solomon, J., Gustavsson, J., and Alvi, F., "Implementing Resonant Enhanced Pulsed Micro-Actuators for the Control of Supersonic Impinging Jets," 50th AIAA Aerospace Sciences Meeting, January 2012, AIAA 2012-0065.
- [11] Solomon, J., Hong, S., Wiley, A., Kumar, R., Annaswamy, A., and Alvi, F., "Control of Supersonic Resonant Flows Using High Bandwidth Micro-Actuators," 15th AIAA/CEAS Aeroacoustics Conference, May 2009, AIAA 2009-3247.
- [12] Bower, W., Kibens, V., Cary, A., Alvi, F., Raman, G., Annaswamy, A., and Malmuth, N., "High-Frequency Excitation Active Flow Control for High-Speed Weapon Release (HIFEX)," 2nd AIAA Flow Control Conference, June-July 2004, AIAA 2004-2513.
- [13] Shouman, K., Suplisson, A., Grove, J., and Bower, W., "Supersonic Store Separation at the Holloman High Speed Test Track," Society of Experimental Test Pilots, 2007.
- [14] Solomon, J. T., Foster, C., and Alvi, F., "Design and Characterization of High-Bandwidth, Resonance Enhanced Pulsed Microactuators: A Parametric Study," *AIAA Journal*, Vol. 51, No. 2, February 2013.

- [15] Crittenden, T. M., Woo, G. T. K., and Glezer, A., "Combustion Powered Actuators for Separation Control," 6th AIAA Flow Control Conference, June 2012, AIAA 2012-3135.
- [16] Brzozowski, D. P., Woo, G. T. K., Culp, J. R., and Glezer, A., "Transient Separation Control Using Pulse-Combustion Actuation," *AIAA Journal*, Vol. 48, No. 11, November 2010.
- [17] Woo, G. T. K., Glezer, A., Bain, J., Sankar, L., and Crittenden, T. M., "Rotorcraft Fuselage Drag Reduction using Combustion Powered Actuators," 49th AIAA Aerospace Sciences Meeting, January 2011, AIAA 2011-0034.
- [18] Samimy, M., Adamovich, I., Webb, B., Kastner, J., Hileman, J., Keshav, S., and Palm, P., "Development and Application of Localized Arc Filament Plasma Actuators for Jet Flow and Noise Control," 42nd AIAA Aerospace Sciences Meeting, January 2004, AIAA 2004-0184.
- [19] Hahn, C., Kearney-Fischer, M., and Samimy, M., "Effects of Ring Groove and Duty Cycle on Plasma Actuator Performance in High Speed Jets," 49th AIAA Aerospace Sciences Meeting, January 2011, AIAA 2011-0977.
- [20] Samimy, M., Kim, J., Kastner, J., Adamovich, I., and Utkin, Y., "Active Control of a Mach 0.9 Jet for Noise Mitigation Using Plasma Actuators," *AIAA Journal*, Vol. 45, No. 4, April 2007.
- [21] Samimy, M., Kearney-Fischer, M., Kim, J., and Sinha, A., "High-Speed and High-Reynolds-Number Jet Control Using Localized Arc Filament Plasma Actuators," *Journal of Propulsion and Power*, Vol. 28, No. 2, March-April 2012.
- [22] Caraballo, E., Webb, N., Little, J., Kim, J., and Samimy, M., "Supersonic Inlet Flow Control Using Plasma Actuators," 47th AIAA Aerospace Sciences Meeting, January 2009, AIAA 2009-0925.
- [23] Land III, H. B., Grossman, K. R., Cybyk, B. Z., and VanWie, D. M., "Solid State Supersonic Flow Actuator and Method of Use," U.S. Patent 7,988,103, August 2011.
- [24] Reedy, T. M., Kale, N. V., Dutton, J. C., and Elliott, G. S., "Experimental Characterization of a Pulsed Plasma Jet," 50th AIAA Aerospace Sciences Meeting, January 2012, AIAA 2012-0904.
- [25] Foster, C. H., Solomon, J. T., and Alvi, F. S., "Visual Study of Resonance Dominated Microjet Flows using Laser-Based Micro-Schlieren," 49th AIAA Aerospace Sciences Meeting, January 2011, AIAA 2011-0766.
- [26] Caruana, D., Barricau, P., Hardy, P., Cambronne, J. P., and Belinger, A., "The "Plasma Synthetic Jet" Actuator. Aero-thermodynamic Characterization and first Flow Control Applications," 47th AIAA Aerospace Sciences Meeting, January 2009, AIAA 2009-1307.

- [27] Cybyk, B. Z., Simon, D. H., Land III, H. B., and Wilkerson, J. T., “SparkJet Actuators for Flow Control,” DTIC report, The Johns Hopkins University Applied Physics Laboratory, February 2007.
- [28] Grossman, K. R., Cybyk, B. Z., and VanWie, D. M., “SparkJet Actuators for Flow Control,” 41st Aerospace Sciences Meeting and Exhibit, 6-9 January 2003, AIAA 2003-0057.
- [29] Cybyk, B. Z., Wilkerson, J. T., and Grossman, K. R., “Performance Characteristics of the SparkJet Flow Control Actuator,” 2nd AIAA Flow Control Conference, June 2004, AIAA 2004-2131.
- [30] Cybyk, B. Z., Simon, D. H., Land III, H. B., Chen, J., and Katz, J., “Experimental Characterization of Supersonic Flow Control Actuator,” 44th AIAA Aerospace Sciences Meeting, January 2006, AIAA 2006-0478.
- [31] Grossman, K., Cybyk, B., Rigling, M., and VanWie, D., “Characterization of SparkJet Actuators for Flow Control,” 42nd AIAA Aerospace Sciences Meeting and Exhibit, January 2004, AIAA 2004-0089.
- [32] Anderson, K. V. and Knight, D. D., “Plasma Jet for Flight Control,” *AIAA Journal*, Vol. 50, No. 9, September 2012.
- [33] Anderson, K. V. and Knight, D. D., “Characterization of Single Pulse of Plasma Jet,” 50th AIAA Aerospace Sciences Meeting, January 2012, AIAA 2012-0188.
- [34] Quint, G., Rogier, F., and Dufour, G., “Numerical Modeling of the Electric Arc Created Inside the Cavity of the PSJ Actuator,” 20th AIAA Computational Fluid Dynamics Conference, June 2011, AIAA 2011-3394.
- [35] Narayanaswamy, V., *Investigation of a pulsed-plasma jet for separation shock boundary layer interaction control*, Ph.D. thesis, University of Texas at Austin, August 2010.
- [36] Haack, S. J., Land III, H. B., Cybyk, B. Z., Ko, H. S., and Katz, J., “Characterization of a High-Speed Flow Control Actuator Using Digital Speckle Tomography and PIV,” 4th AIAA Flow Control Conference, June 2008, AIAA 2008-3759.
- [37] Ostman, R. J., Herges, T. G., Dutton, J. C., and Elliott, G. S., “Effect on High-Speed Boundary-Layer Characteristics from Plasma Actuators,” 51st AIAA Aerospace Sciences Meeting, January 2013, AIAA 2013-0527.
- [38] Hardy, P., Barricau, P., Belinger, A., Caruana, D., Cambronne, J., and Gleyzes, C., “Plasma Synthetic Jet for Flow Control,” 40th AIAA Fluid Dynamics Conference, June 2010, AIAA 2010-5103.
- [39] Golbabaie-Asl, M., Knight, D., Anderson, K., and Wilkinson, S., “SparkJet Efficiency,” 51st AIAA Aerospace Sciences Meeting, January 2013, AIAA 2013-0928.

- [40] Haack, S., Taylor, T., Emhoff, J., and Cybyk, B., “Development of an Analytical Spark-Jet Model,” 5th AIAA Flow Control Conference, June 2010, AIAA 2010-4979.
- [41] Raizer, Y. P., *Gas Discharge Physics*, Springer-Verlag, 1st ed., 1991.
- [42] Ekici, O., Ezekoye, O. A., Hall, M. J., and Matthews, R. D., “Thermal and Flow Fields Modeling of Fast Spark Discharges in Air,” *Journal of Fluids Engineering*, Vol. 129, 2007, pp. 55–65.
- [43] Popkin, S. H., *One-Dimensional Numerical Model Development of a Plasma-Based Actuator*, Ph.D. thesis, University of Maryland, 2014.
- [44] Narayanaswamy, V., Laxminarayan, R., and Clemens, N., “Characterization of a High-Frequency Pulsed-Plasma Jet Actuator for Supersonic Flow Control,” *AIAA Journal*, Vol. 48, No. 2, 2010, pp. 297–305.
- [45] Roth, W., Guest, P. G., von Elbe, G., and Lewis, B., “Heat Generation by Electric Sparks and Rate of Heat Loss to the Spark Electrodes,” *The Journal of Chemical Physics*, Vol. 19, No. 12, December 1951.
- [46] Staff, A. R., “Equations, Tables, and Charts for Compressible Flow,” Tech. Rep. 1135, National Advisory Committee for Aeronautics, 1953.
- [47] Kleine, H., “Filming the Invisible - Time-Resolved Visualization of Compressible Flows,” *The European Physics Journal Special Topics*, Vol. 182, 2010, pp. 3–34.
- [48] Popkin, S. H., Cybyk, B., Land III, H. B., Emerick II, T. M., Foster, C. H., and Alvi, F. S., “Recent Performance-Based Advances in SparkJet Actuator Design for Supersonic Flow Applications,” 51st AIAA Aerospace Sciences Meeting, January 2013, AIAA 2013-0322.
- [49] Haack, S. J. and Foster, C. H., “Experimental Estimation of SparkJet Efficiency,” 42nd AIAA Plasmadynamics and Lasers Conference, June 2011, AIAA 2011-3997.
- [50] Emerick, T., Ali, M., Foster, C., Alvi, F., Popkin, S., and Cybyk, B., “SparkJet Actuator Characterization in Supersonic Crossflow,” 6th AIAA Flow Control Conference, June 2012, AIAA 2012-2814.
- [51] Optoelectronics, P. E., “High Performance Flash and Arc Lamps,” <http://laser-caltech.web.cern.ch/laser-caltech/report/Flash%20lamp%20Eg&G.pdf>, 2013, Online accessed July 2013.
- [52] Denso, “Denso Spark Plugs,” <http://www.globaldenso.com/en/products/aftermarket/plug/catalog/europe/pdf/pdfcatalog-eu-gbr.pdf>, cited 20 December 2010.
- [53] Bowers, R. J., Sorensen, C. D., and Eagar, T. W., “Electrode Geometry in Resistance Spot Welding,” *Supplement to the Welding Journal*, Vol. 69, No. 2, 1990, pp. 45s–51s.

# AFOSR Deliverables Submission Survey

Response ID:3360 Data

1.

---

## 1. Report Type

Final Report

## Primary Contact E-mail

Contact email if there is a problem with the report.

bohdan.cybyk@jhuapl.edu

## Primary Contact Phone Number

Contact phone number if there is a problem with the report

240-228-7624

## Organization / Institution name

Johns Hopkins University Applied Physics Laboratory

## Grant/Contract Title

The full title of the funded effort.

Development of Energetic Actuators for Shear and Vortex Dominated Flow Control

## Grant/Contract Number

AFOSR assigned control number. It must begin with "FA9550" or "F49620" or "FA2386".

FA9550-09-1-0575

## Principal Investigator Name

The full name of the principal investigator on the grant or contract.

Bohdan Z Cybyk

## Program Manager

The AFOSR Program Manager currently assigned to the award

Douglas R Smith

## Reporting Period Start Date

11/30/2009

## Reporting Period End Date

11/30/2013

## Abstract

Active flow control (AFC) techniques available for high-speed flow applications, including supersonic and hypersonic, are very limited. The Johns Hopkins University Applied Physics Laboratory (JHU/APL), in collaboration with the Florida State University Advanced Aero-Propulsion Laboratory (FSU/AAPL), is investigating and developing a promising device for high-speed flow control called the SparkJet actuator. This actuator, which produces a synthetic jet with high exhaust velocities, holds the promise of manipulating high-speed flows without active mechanical components. Computational Fluid Dynamic (CFD) modeling is used to investigate the predicted fundamental physics and flow interactions within and near the SparkJet actuator. The

DISTRIBUTION A: Distribution approved for public release.

CFD results were used for comparison to microschlieren imagery acquired at FSU/AAPL and the 1-D numerical model developed at JHU/APL. To further verify the model accuracy, experimental testing involving time-dependent, pressure measurements of the actuator cavity pressure as a function of orifice diameter, cavity volume, and energy deposition. Finally, the SparkJet actuator design has been modified to create reliable and efficient devices.

---

**Distribution Statement**

This is block 12 on the SF298 form.

Distribution A - Approved for Public Release

---

**Explanation for Distribution Statement**

If this is not approved for public release, please provide a short explanation. E.g., contains proprietary information.

---

**SF298 Form**

Please attach your **SF298** form. A blank SF298 can be found [here](#). Please do not spend extra effort to password protect or secure the PDF, we want to read your SF298. The maximum file size for SF298's is 50MB.

[FA9550-09-1-0575\\_SF298\\_20140224.pdf](#)

---

**Upload the Report Document. The maximum file size for the Report Document is 50MB.**

[FA9550-09-1-0575\\_final\\_report\\_20140224.pdf](#)

---

**Upload a Report Document, if any. The maximum file size for the Report Document is 50MB.**

---

**Archival Publications (published) during reporting period:**

Haack, S., Taylor, T., Emhoff, J., and Cybyk, B., "Development of an Analytical SparkJet Model," 5th AIAA Flow Control Conference, June 2010, AIAA 2010-4979.

Haack, S. J. and Foster, C. H., "Experimental Estimation of SparkJet Efficiency," 42nd AIAA Plasmadynamics and Lasers Conference, June 2011, AIAA 2011-3997.

Emerick, T., Ali, M., Foster, C., Alvi, F., Popkin, S., and Cybyk, B., "SparkJet Actuator Characterization in Supersonic Crossflow," 6th AIAA Flow Control Conference, June 2012, AIAA 2012-2814.

Popkin, S. H., Cybyk, B., Land III, H. B., Emerick II, T. M., Foster, C. H., and Alvi, F. S., "Recent Performance-Based Advances in SparkJet Actuator Design for Supersonic Flow Applications," 51st AIAA Aerospace Sciences Meeting, January 2013, AIAA 2013-0322.

Popkin, S. H., Taylor, T. M., and Cybyk, B. Z., "Development and Application of the SparkJet Actuator for High-Speed Flow Control," Johns Hopkins APL Technical Digest, 32(1), June 2013.

Popkin, S. H., Cybyk, B. Z., Foster, C. H., Alvi, and F. S., "Experimental Estimation of SparkJet Efficiency," AIAA Journal (accepted pending revisions).

Popkin, S. H., One-Dimensional Numerical Model Development of a Plasma-Based Actuator, Ph.D. thesis, University of Maryland, 2014.

---

**Changes in research objectives (if any):**

---

**Change in AFOSR Program Manager, if any:**

Original Program Manager (2009) was Dr. John Schmisseeur, AFOSR/NA, (703)696-6962, [john.schmisseeur@afosr.af.mil](mailto:john.schmisseeur@afosr.af.mil)

---

**Extensions granted or milestones slipped, if any:**

DISTRIBUTION A: Distribution approved for public release.



**AFOSR LRIR Number**

**LRIR Title**

**Reporting Period**

**Laboratory Task Manager**

**Program Officer**

**Research Objectives**

**Technical Summary**

**Funding Summary by Cost Category (by FY, \$K)**

	Starting FY	FY+1	FY+2
Non-Military Government Personnel Costs			
In-house Contractor Costs			
Travel (Be Specific)			
Training (Be Specific)			
Supplies			
Other Expenses (Be Specific)			
Total Resource Requirements			

**Report Document**

**Appendix Documents**

## 2. Thank You

**E-mail user**

Feb 26, 2014 12:08:38 Success: Email Sent to: bohdan.cybyk@jhuapl.edu

Response ID: 3360

<b>Survey Submitted:</b>	Feb 26, 2014 (12:08 PM)
<b>IP Address:</b>	128.244.11.5
<b>Language:</b>	English (en-us)
<b>User Agent:</b>	Mozilla/4.0 (compatible; MSIE 8.0; Windows NT 6.1; WOW64; Trident/4.0; SLCC2; .NET CLR 2.0.50727; .NET CLR 3.5.30729; .NET CLR 3.0.30729; Media Center PC 6.0; .NET4.0C; .NET4.0E; InfoPath.3)
<b>Http Referrer:</b>	

<b>Page Path:</b>	1 : (SKU: 1) 2 : Thank You (SKU: 2)
<b>SessionID:</b>	1393431624_530e1448343544.48805185

Response Location

<b>Country:</b>	United States
<b>Region:</b>	MD
<b>City:</b>	Laurel
<b>Postal Code:</b>	20723
<b>Long &amp; Lat:</b>	Lat: 39.135799, Long:-76.872002